



# SEPARATION AND QUANTIFICATION OF STRUCTURALLY SIMILAR IMPURITIES BY HPLC METHOD OF VORTIOXETINE HYDROBROMIDE- AN ANTIDEPRESSANT DRUG

**Shashikant B. Landge,<sup>[a]</sup> Sunil B. Dahale,<sup>[a]</sup> Sachin J. Devadhe,<sup>[a]</sup> Dattatray G. Deshmukh,<sup>[a]</sup> Pavankumar V. Solanki,<sup>[a]</sup> Sanjay A. Jadhav,<sup>[a]</sup> László Kótai,<sup>[b]</sup> Saroj R. Bembalkar,<sup>[c]\*</sup> and Rajendra P. Pawar<sup>[c]\*</sup>**

**Keywords:** Vortioxetine; positional isomers; isomeric impurities; HPLC method; normal phase

A new, specific, and robust normal phase liquid chromatographic (NP-LC) method for the determination of structurally similar impurities (isomers) of Vortioxetine hydrobromide has been developed and validated. An excellent chromatographic resolution between the structurally similar impurities (isomers) and Vortioxetine hydrobromide was achieved on Chiralpak-ADH (250 x 4.6 mm ID), 5  $\mu$  column. The mobile phase used of n-hexane, ethanol, diethylamine, and trifluoroacetic acid in the ratio (75:25:0.05:0.05, v/v/v/v) and the flow rate was maintained at 1.0 mLmin<sup>-1</sup>. UV detection was carried out at 235 nm. The resolution between all positional isomers and Vortioxetine hydrobromide was found not less than 2. An effect of column oven temperature on the resolution was also studied and found to be  $\geq 2.0$ . Three structurally similar impurities (Isomer-1, Isomer-2, and Isomer-3) have been detected in the test sample of Vortioxetine hydrobromide by advanced NP-LC method. Further, these isomeric impurities were characterized by mass spectrometry, <sup>1</sup>H NMR and FT-IR spectral data. The developed method was validated as per ICH guidelines and found to be specific, robust, and selective. The developed NP-LC method was successfully applied to the analysis of drug substance and drug product samples of Vortioxetine hydrobromide.

\*Corresponding author

E-mail: [bembalkarsaraj@rediffmail.com](mailto:bembalkarsaraj@rediffmail.com),  
[rppawar@yahoo.com](mailto:rppawar@yahoo.com)

<sup>[a]</sup> Research and Development Center, Megafine Pharma (P) Ltd, Nashik, India

<sup>[b]</sup> Research Centre for Natural Sciences, Budapest, Hungary

<sup>[c]</sup> Department of Chemistry, Deogiri College, Station Road, Aurangabad-431005, Maharashtra, India

## INTRODUCTION

Vortioxetine is an antidepressant drug used to treat depressive disorders (depression). A major depressive disorder is a severe and disabling condition that is often accompanied by cognitive dysfunction.<sup>1</sup> This dysfunction in depression may include impairments in attention, memory, executive function, and processing speed. Acute serotonin (5HT) depletion impairs memory and mood in vulnerable patients. The depressive disorder has traditionally been treated with tricyclic antidepressants, monoamine oxidase inhibitors, selective serotonin and norepinephrine uptake inhibitors. Vortioxetine falls under a class of typical antidepressants known as serotonin modulators and stimulators.

This drug is sold under the trade names Trintellix and Brintellix. It is made by the pharmaceutical companies Lundbeck and Takeda. Vortioxetine given orally once daily, to start with an initial dose of 5 mg or 10 mg and can be extended to a maximum of 20 mg, depending on the situation of the case under the fed condition or fasting conditions.<sup>2</sup>

There are lots of regulatory challenges to address the regulatory queries on control and carryover by organic impurities in drug substance or drug product. These impurities are sometime genotoxic, hence the proper study of these impurities by the suitably developed analytical method is critical in drug development in today's scenario. These improved continuously with the use of new reagents, catalyst and intermediates, etc., or with changes in synthesis routes. Therefore, the control of organic or inorganic impurities in the manufacturing stages of API and its starting material plays an essential role during the process development. We have observed three isomeric impurities viz., Isomer-1, Isomer-2, and Isomer-3 in the Vortioxetine hydrobromide drug substance sample (Figure 1).

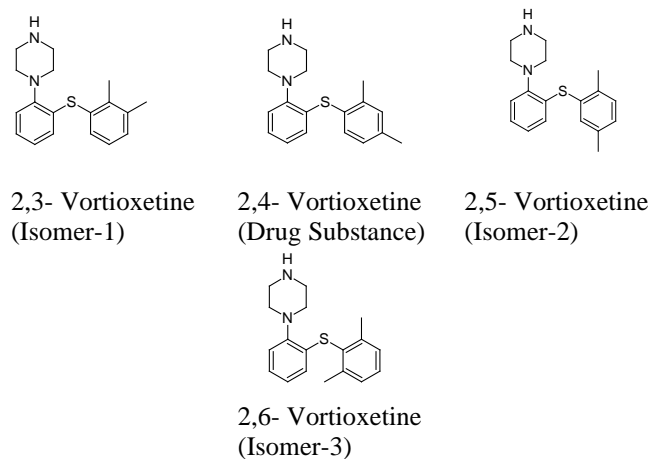


**Figure 1.** Structure of Vortioxetine and its isomeric impurities (Isomer-1, Isomer-2, and Isomer-3).

During the literature search, there were several bio-analytical methods<sup>3-7</sup> reported for the determination of Vortioxetine and its metabolite in blood plasma. Few other pieces of literature were also available on the quantitative determination of Vortioxetine and its impurities in biological and formulation samples.<sup>8-11</sup> However, these papers have not provided the details on the analysis of structurally similar impurities (Isomers) of Vortioxetine hydrobromide. It is mandatory that, to meet the regulatory requirement, the impurity profile study of drug substances and drug products has to be carried out using a suitable and validated analytical method in the final drug substance and drug product.<sup>12,13</sup> Further, during the review of pharmacopeial monographs, Vortioxetine hydrobromide was not found in them.

Best of our knowledge, there were no methods reported for the determination of structurally similar impurities of Vortioxetine in drug substance and drug product by using the HPLC technique. The core objective of this research work was to develop a specific and robust NP-LC method for the determination of structurally similar impurities of Vortioxetine and its analytical method validation. The identified isomeric impurities required for method development and method validation were received from Megafine Pharma R&D center, process development laboratory. IR, mass spectra and NMR methods were used to characterize the impurities. The developed method was found to be specific, selective, and robust for the determination of isomeric impurities of Vortioxetine hydrobromide. The developed method was successfully validated according to the USP<1225> Validation of Compendial Procedures and ICH Q2 (R1) guidelines.<sup>14, 15</sup>

## EXPERIMENTAL

The common reagents like diethylamine and trifluoroacetic acid AR grade were procured from Merck (India). HPLC grade n-hexane and ethanol were procured from Qualigen fine chemicals, Mumbai, India. The samples of Vortioxetine hydrobromide and its three isomers (Isomer-1, Isomer-2, and Isomer-3) were received from the synthetic laboratory of Megafine Pharma (P) Ltd., Nashik, India.

HPLC (Agilent 1200, Agilent Technologies, Germany) equipped with an ultraviolet (UV) detector was used for method development and method validation. The n-hexane, ethanol, diethylamine, and trifluoroacetic acid was used in the ratio of 75:25:0.05:0.05 (v/v). The analysis was carried out under isocratic mode. The flow rate and injection volumes were fixed at 1.0 mL min<sup>-1</sup> and 10 µL, respectively and the autosampler temperature was kept at 10 °C. The data were acquired at 235 nm for 45 min and processed by using Chromeleon Software Ver. 6.8.

### Preparation of analytical solutions

Individual stock solutions of each impurity and Vortioxetine hydrobromide reference standard at a concentration of 200 µg mL<sup>-1</sup> were prepared in the mobile phase and further diluted adequately to study the validation parameters to get the 2.0 µg mL<sup>-1</sup> concentrations of Vortioxetine and its impurities, respectively, as the standard solution, shown in Electronic Supplementary Material

Figure 1b. The reference standard of Vortioxetine hydrobromide (2000 µg mL<sup>-1</sup>) spiked with all impurities at a specification level (0.10% w/w) was used as a system suitability solution (SST) as shown in Electronic Supplementary Material Figure 1c.

The test sample solution having a concentration of 2000 µg mL<sup>-1</sup> was prepared for the determination of isomeric impurities of Vortioxetine hydrobromide. The mobile phase was used as a diluent for the preparation of all analytical solutions. The specification limits used for validation studies of Isomeric impurities (Isomer-1, Isomer-2, and Isomer-3) was 0.10 % w/w. Formulation sample was prepared by powdering the tablets of Vortioxetine hydrobromide contains 40 mg of the active ingredient in the diluent in a 20 mL flask and ultrasonicated for ca. 15min. Finally, this solution was filtered through the Merck Nylon syringe filter having pore size 0.45 µm. The clear liquid was collected and used for the determination of related substances in the pharmaceutical dosage forms.

### Chromatographic procedure

The blank (diluent), resolution mixture, six replicate injections of standard solution, and test sample solution were separately injected and chromatographed. The relative standard deviation (RSD) of NMT 5.0 % from six replicate injections of standard solution for Vortioxetine and its Isomers, Isomer-1, Isomer-2, Isomer-3 were used to verify the system suitability criteria of the method. The resolution NLT2.0 between Vortioxetine and its three isomers was set as system suitability criteria in resolution mixture.

### Identification of Impurities

Vortioxetine hydrobromide crude samples were analyzed for the identification of isomeric impurities by the proposed method. Three isomeric impurities were detected in the crude sample of Vortioxetine. The m/z of detected peaks was determined by LCMS technique. The observed m/z values confirmed the possible structures of isomeric impurities (Figure 1). The impurities (Isomer-1, Isomer-2, and Isomer-3) were synthesized and co-injected with the Vortioxetine hydrobromide test samples to confirm its retention times. The representative chromatogram of spiked test preparation is shown in Electronic Supplementary Material Figure 2b. These identified impurities found to be carryover impurities from the starting material of Vortioxetine hydrobromide. It is bound to come as carryover in Vortioxetine hydrobromide by the reaction of such impurities with another key starting material.

Bruker AV400 (400 MHz) spectrometer was used to record the <sup>1</sup>H NMR spectra by using deuterated chloroform as a solvent and tetramethylsilane (TMS) as an internal standard.

LCMS-2020 mass spectrometer (Shimadzu) equipped with a quadrupole mass analyzer was used to record the mass spectra. Spectra were acquired from m/z 100 to 1000 at scan speed 3750 µ/sec with event time 0.2 sec. Ions were detected in electron spray ionization with positive ion mode.

Perkin Elmer model-spectrum-100 (California, USA) instrument (KBr pellet method) was used to record the FT-IR spectra.

## RESULTS AND DISCUSSION

### Development of analytical method

The objective of analytical method development was to separate Vortioxetine hydrobromide and its three isomeric impurities (Isomer-1, Isomer-2, and Isomer-3) in short run time with excellent resolution and good peak shape. The resolution between isomeric impurities was critical during the method development and hence selection of proper stationary phase played a significant role during the method development. Initial method development trials were conducted on different stationary phases like Chiralpak-ODH, Chiralpak-ADH, Chiralpak-IA, Chiralpak-IB, and Chiralpak-IC Columns along with the optimization of other chromatographic conditions like detection wavelength, type and the quantity of organic solvent and modifier, the composition of the mobile phase, thermostat, and column oven temperature.<sup>16</sup>

Analytical trials were carried out at isocratic condition by using Chiralpak-IA column [(250 x 4.6 mm) 5 $\mu$ m] and a mixture of n-hexane, ethanol, and diethylamine in the different ratios (e.g., 70:30:0.05, v/v/v). The various trials taken by changing the ratio of ethanol were found not suitable to separate the Vortioxetine and its three isomers. The peak of Vortioxetine was found co-eluted with its isomeric impurities. To increase the resolution between Vortioxetine and its isomers, the stationary phase of chiral columns was screened (e.g., Chiralpak-ODH, Chiralpak-ADH, Chiralpak-IA, Chiralpak-IB, and Chiralpak-IC). Due to this change, the resolution between Vortioxetine and its three isomers was increased but not to the satisfactory level. Few additional trials were conducted on the Chiralpak-ADH column by using the other modifier, i.e., trifluoroacetic acid. Finally, the change in the column with a

combination of modifiers, diethylamine and trifluoroacetic acid has given good separation between the Vortioxetine and its isomers.

The system suitability criterion was evaluated at every time during the different trial runs of method development to ensure the strength of the developed method. The isocratic mode was preferred than the gradient mode to achieve a stable baseline due to normal phase chromatography. Finally, satisfactory resolution and good peak shape of analyte were observed on Chiralpak-ADH, (250 x 4.6mm ID), 5 $\mu$  column at flow rate 1.0 mL min<sup>-1</sup>,  $\lambda$  235nm, column oven temperature 35°C, injection thermostat 10°C. The mobile phase consists of n-hexane, ethanol, diethylamine, and trifluoroacetic acid in the ratio (75:25:0.05:0.05,v/v/v/v). It was observed that Vortioxetine and its three isomers, Isomer-1, Isomer-2, and Isomer-3, are well separated under the optimized conditions with a resolution greater than 2.0 (Figure 2).

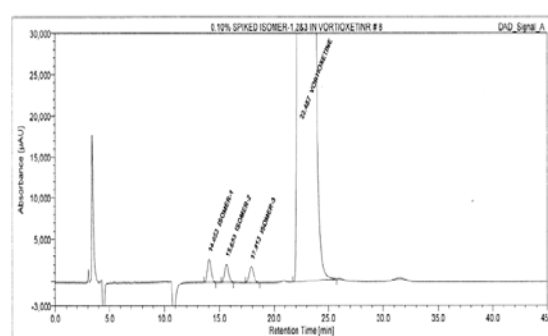


**Figure 2.** Typical NP-LC chromatograms of the Vortioxetine test sample spiked with isomeric impurities (Isomer-1, Isomer-2, and Isomer-3).

**Table 1.** Results of a validation study for isomeric impurities of Vortioxetine.

Compound	Related substances results, in %			
	Isomer-1	Isomer-2	Isomer-3	Vortioxetine
<b>Precision: %RSD</b>				
Method precision (n=6)	1.08	1.95	3.71	-
<b>Limit of detection (LOD)</b>				
LOD (% w.r.t. test)	0.008	0.008	0.008	0.008
<b>Limit of quantitation (LOQ)</b>				
LOQ (% w.r.t. test)	0.025	0.025	0.025	0.025
<b>Linearity: For related substances LOQ to 500 % of specification level</b>				
The correlation coefficient (r) <sup>2</sup>	1.00000	1.00000	0.99997	0.99998
Slope	32671.77	26431.51	27210.24	36785.80
Intercept	733.46	-365.57	-276.50	1600.94
<b>Accuracy; Mean Recovery (%RSD): LOQ to 150 % of specification level</b>				
LOQ	97.01 (2.34)	103.91 (2.80)	109.93 (2.56)	-
50 %	104.97(0.98)	106.39 (1.21)	111.78 (1.48)	-
100 %	105.15(1.48)	104.93 (1.97)	106.11 (1.68)	-
150 %	102.21(0.82)	104.08 (1.26)	106.18 (0.98)	-

% w.r.t. test LOD LOQ values are in % concerning test concentration of 2000  $\mu$ g mL<sup>-1</sup>

The observed resolution indicates that the excellent capability of the developed method to resolve the closely eluted peaks. This optimized method was validated as per ICHQ2 (R1) guidelines. The representative chromatograms are provided below in the Electronic Supplementary Information Figures 1 and 2 or in Figure 2.

### Analytical method validation

#### Specificity

Specificity is an ability of the method to measure the analyte response in the presence of its potential impurities. The uniqueness of the developed NP-HPLC method was determined in the presence of its isomeric impurities (Isomer-1, 2, and 3). The test sample of Vortioxetine was spiked with its isomeric impurities at specification level and injected along with its every isomeric standard to confirm the retention time of spiked isomeric impurities; similar to each isomeric standard.

#### Precision

The system precision for Vortioxetine and its isomer was verified by injecting six replicate injections of the standard solution. % RSD of Vortioxetine and its isomers peak areas were evaluated and found to be < 5.0 %. The test samples of Vortioxetine hydrobromide were prepared by spiking the Isomeric impurities viz., Isomer-1, 2 and 3 at the specification level. The % RSD ( $n = 6$ ) for each isomer was evaluated and found to be between 1.08-3.71 %. The results are depicted in Table 1.

#### Linearity

The linearity of peak areas versus different concentrations was evaluated for Vortioxetine and its three isomers using six levels ranging from LOQ to 500 % (LOQ, 50, 100, 200 and 500 %) concerning the specification level of impurities. The linear regression data for all the components were tested and the correlation coefficient for each component found to be more than 0.999. The results are depicted in Table 1.

#### Limits of detection and quantitation (LOD and LOQ)

Several approaches for determination of the quantitation limit are reported in ICH Q2 (R1), depending on the procedure (non-instrumental or instrumental). Based on the visual evaluation, the quantitation limit has been determined by the analysis of samples with known concentrations of analyte (isomeric impurities) and establishing the minimum level at which the analyte can be quantified with acceptable accuracy and precision. 25 % of specification (i.e., 0.025 %) concentration was selected to determine the LOQ of the method. Further, the LOQ was verified by giving the six replicate injection of LOQ concentration. The observed % RSD of LOQ precision was < 10.0 %. 1/3 concentration of LOQ was established as a LOD. The results are depicted in Table 1.

#### Recovery

Vortioxetine hydrobromide test sample solutions were spiked with its three isomers at four different concentration levels, LOQ, 50, 100, and 150 % at the specified limit in triplicate. These spiked sample solutions were analyzed to determine the recovery of the analytical method. The recovery of all three isomers was found to be in-between the predefined acceptance criterion, 80.0-120.0 %. The results are depicted in Table 1.

#### Mobile phase stability

The Vortioxetine test sample was analyzed after 24 h and 48 h by using the same mobile phase. Vortioxetine test sample spiked with isomeric impurities at specification level was used to evaluate the mobile phase stability of the method. The content of each isomeric impurity was evaluated and compared with the results of method precision. The study indicated that there is no effect on the determination of isomeric impurities even after 48 h. Therefore the mobile phase found to be stable up to 48 h.

#### Stability of analytical solution

The sample solutions of Vortioxetine hydrobromide spiked with isomeric impurities were prepared and analyzed immediately after 24 and 48 h to determine the stability of the analytical solution. The sample cooler temperature was maintained at about 8 °C. The results of these studies indicated that the sample solution is stable at 8 °C for 48 h.

#### Robustness

To evaluate the robustness of the developed method, the chromatographic conditions were deliberately altered, and the resolution between closely eluting peak pair of isomeric impurities and Vortioxetine was evaluated. The flow rate of the mobile phase was 1.0 mL min<sup>-1</sup>. To study the effect of flow rate on the resolution, it was altered by 0.1 units, i.e., from 0.9 to 1.1 mL min<sup>-1</sup>. The effect of column temperature on the resolution was studied at 27 and 33 °C instead of 30°. The effect of change in % of ethanol on the resolution was also studied at -1 % (24 %) and +1 % (26 %) instead of 25 %. All the other mobile phase components were held constant, as described above. In all the varied chromatographic conditions (flow rate, column temperature and % ethanol), the tailing factor of Vortioxetine was found <2.0 and the resolution between isomeric impurities (themselves) and with Vortioxetine peak found >2.0. This robustness study demonstrates that the developed analytical method is robust.

#### Application of the method

The analysis of tablet and bulk drug samples indicated that the method is specific and robust for the determination of isomeric impurities of Vortioxetine hydrobromide in these samples (Table 2). The developed method was found to be capable of the quantitative determination of isomeric impurities of Vortioxetine hydrobromide in its bulk drug and a pharmaceutical dosage form. The results are provided in Table 2.

**Table 2.** Results (%) of tablet analysis and bulk drug sample analysis

Sample source	Isomer-1	Isomer-2	Isomer-3
	Amount in %		
Formulation #1	0.01	0.03	ND
Bulk drug substance			
#1	ND	ND	ND
#2	ND	ND	ND
#3	ND	ND	ND

ND= Not detected

## CONCLUSION

A new, specific and robust NP-LC method has been developed that separates the isomeric impurities of Vortioxetine hydrobromide with excellent peak shape and resolution. The developed method was further validated to ensure compliance per ICH Q2(R1) guideline. This method was applied for testing of Vortioxetine drug substance and drug product samples.

## ACKNOWLEDGMENTS

The authors wish to thank the management of Megafine Pharma (P) Ltd. for giving support to this work. We would also like to thank colleagues in the division of Research and Development of Megafine Pharma (P) Ltd for their cooperation to carry out this work.

## REFERENCES

- Pehrson, A. L., Leiser, S. C., Gulinello, M., Dale E., Li, Y., Waller, J. A., Sanchez, C., Treatment of Cognitive Dysfunction in Major Depressive Disorder—a Review of the Preclinical Evidence for Efficacy of Selective Serotonin Reuptake Inhibitors, Serotonin-norepinephrine Reuptake inhibitors and the Multimodal-acting Antidepressant Vortioxetine, *Eur. J. Pharmacol.*, **2015**, 753, 19-31. <https://doi.org/10.1016/j.ejphar.2014.07.044>.
- Brignone, M., Diamond, F., Painchault, C., Takyar, S., Efficacy and tolerability of switching therapy to Vortioxetine versus other antidepressants in patients with major depressive disorder, *Curr. Med. Res. Opin.*, **2016**, 32, 351–366. <https://doi.org/10.1185/03007995.2015.1128404>.
- Gu, E. M., Huang, C., Liang, B., Yuan, L., Lan, T., Hu, G., Zhou, H., An UPLC–MS/MS method for the quantitation of Vortioxetine in rat plasma: Application to a pharmacokinetic study, *J. Chromy. B: Anal. Technol. Biomed. Life Sci.*, **2015**, 997, 70–74. <https://doi.org/10.1016/j.jchromb.2015.05.010>.
- Wróblewski, K., Petruczyni, A., Buszewski, B., Szultka-Mlynska, M., Juchnowicz, H., Waksmundzka-Hajnos, M., Determination of Vortioxetine in Human Serum and Saliva Samples by HPLC–DAD and HPLC–MS, *Acta Chrom.*, **2017**, 29(3), 325–344. <https://doi.org/10.1556/1326.2017.29.3.02>.
- Velamakanni, S. R., Padala, V., Polagani, S. R., Boya J., A Novel LC-MS/MS Method for Quantification of Vortioxetine in Human Plasma and its Application to Pharmacokinetic Studies, *J. Global Trends Pharm. Sci.*, **2017**, 8(4), 4584–4597. <https://www.jgtps.com/admin/uploads/OfaWNG.pdf>.
- Qin, M., Qiao, H., Yuan, Y., Shao, Q., A quantitative LC-MS/MS Method for Simultaneous Determination of Deuvortioxetine, Vortioxetine and their Carboxylic acid Metabolite in Rat Plasma, and its Application to a Toxic kinetic Study, *Anal. Methods*, **2018**, 9, 1023–1031. <https://doi.org/10.1039/C7AY02642K>
- Correa, D., Mennickent, S., Godoy, R., Vergara, C., Determination of Vortioxetine and its Degradation Product in Bulk and Tablets, by LC-DAD and MS/MS methods, *Biomed. Chromy.*, **2018**, 32(11). <https://doi.org/10.1002/bmc.4340>
- Dousa, M., Doubsky, J., Srbek, J., Utilization of Photochemically Induced Fluorescence Detection for HPLC Determination of Genotoxic Impurities in the Vortioxetine Manufacturing Process, *J. Chrom. Sci.*, **2016**, 54(9), 1625–1630. <https://doi.org/10.1093/chromsci/bmw116>
- Douša, M., Klvaňa, R., Doubský, J., Srbek, J., Richter, J., Exner, M., Gibala, P., HILIC–MS Determination of Genotoxic Impurity of 2-Chloro-N-(2-Chloroethyl)Ethanamine in the Vortioxetine Manufacturing Process, *J. Chrom. Sci.*, **2016**, 54(2), 119–124. <https://doi.org/10.1093/chromsci/bmv107>
- Dong, S., Yan, Z., Yang, H., A Sensitive Precolumn Derivatization Method for Determination of Piperazine in Vortioxetine Hydrobromide Using a C8 Column and High-Performance Liquid Chromatography–Mass Spectrometry, *Anal. Sci.*, **2016**, 32, 1333–1338. <https://doi.org/10.2116/analsci.32.1333>
- Li, J., Song, S., Zhang, H., Zhao J., Determination of Related Substances in Vortioxetine Hydrobromide Tablets by HPLC, *Chin. J. Pharmaceut.*, **2017**, 48(09), 1359–1364. <https://doi.org/10.16522/j.cnki.cjph.2017.09.020>
- Impurities in New Drug Substances, *Int. Conf. Harmonization (ICH), Methodology Q3A (R2)*. <https://www.fda.gov/media/112426/download>
- Good Manufacturing Practice Guide for Active Pharmaceutical Ingredients, *Int. Conf. Harmonization (ICH), Methodology Q7A*. <https://apic.cefic.org/pub/5GMPDev9911.PDF>
- The United States Pharmacopeia, Validation of Compendial Methods, USP 39, NF34, Section < 1225 >. <https://www.gmp-compliance.org/gmp-news/revise-usp-chapter-1225-validation-of-compndial-methods-approved>
- Validation of Analytical Procedure, *Int. Conf. Harmonization (ICH), Methodology Q2 (R1)*. [http://www.gmp-compliance.org/guidemgr/files/Q2\(R1\).PDF](http://www.gmp-compliance.org/guidemgr/files/Q2(R1).PDF)
- Snyder, L. R., Kirkland, J. J., Glajch, J. L., *Practical LC Method Development*, **1997**. <https://doi.org/10.1002/9781118592014>

Received: 01.02.2020.

Accepted: 11.04.2020.



# KINETIC STUDY OF Fe(II) AND Fe(III) COMPLEXES OF DOPAMINE, (-)-3-(3,4-DIHYDROXYPHENYL)-L-ALANINE AT PHYSIOLOGICAL pH

Nasreen Fatima<sup>[a]</sup>, Shazia Nisar<sup>[a]</sup> and Syed Zafar Abbas<sup>[a]\*</sup>

**Keywords:** Kinetics; mechanism; dopamine; UV-Vis spectrophotometry; pH effect.

The kinetics of complex formation of dopamine, (-)-3-(3,4-dihydroxyphenyl)-L-alanine (Levodopa or LD), with Fe(II) and Fe(III) has been studied spectrophotometrically. The reactions were carried out at a pH range of 3.0 to 9.2, at  $25 \pm 1^\circ\text{C}$ . Complex formation was not observed below pH 4.0. These investigations showed that the Fe(II) and Fe(III) complexes have identical spectra, indicative of same oxidation state of iron in these complexes. Fe(III)-LD complexation was studied only in non-buffered media. The reaction was very fast, and hence was studied using stopped flow technique. This reaction shows a linear dependence on [LD]. While, in case of Fe(II) complexation, a saturation pathway is followed. Rate laws have been deduced.

\* Corresponding Authors

Phone: +61 401308103

E-Mail: mehar\_zafar@yahoo.com

[a] Department of Chemistry, University of Karachi. Karachi-75270, Pakistan

affinity for metal ions, specifically iron, therefore, Levodopa is expected to chelate iron strongly.<sup>15-17</sup> We have studied the effect of pH on stoichiometry and kinetics. Formation constant and reaction mechanism were also evaluated.

## INTRODUCTION

Hemoglobin and myoglobin holds high concentration of iron, which is essential for the oxygen storage and means of transport in the body.<sup>1</sup> Excess iron levels results in enlargement of the liver, cardiac failure, diabetes and Hemochromatosis, a genetic disease, while a major consequence of iron deficiency is Anemia.<sup>2</sup> Ferrous ion ( $\text{Fe}^{\text{II}}$ ), is a vital trace element essential for nearly all creatures.<sup>3</sup> As iron is the most profuse metal for the human body, therefore most symbiosis are tremendously iron dependent. The brain comprises of considerably higher concentration of iron in comparison with other metals.<sup>4</sup> Ferritin mainly exists in the organic form, whilst hemosiderin present in free and reactive form. It is the major iron store in the brain.<sup>5</sup> Due to the presence of BBB (Blood Brain Barrier), iron crosses the endothelial cells and enters in the brain. Therefore, it *cannot* receive iron direct from the blood circulatory system.<sup>6</sup> Accumulation of iron, promotes Alzheimer disease, Hemochromatosis and Parkinson's Diseases (PD), as well.<sup>7-10</sup>

Parkinsonism is caused by deficiency of dopamine in the brain, which might lead to the death of neurons, responsible for production of dopamine in the substantia nigra (SNpc).<sup>11</sup> Deficiency of dopamine in the striatum lead to slow death of Dopaminergic neurons in a progressive way that decrease the capability to organize voluntary movement by the brain.<sup>12</sup>

Keeping in view the role of iron in PD, the present work was planned to evaluate the importance of Fe-LD interaction in this disease. Iron plays a fundamental role as a source for PD, that also supported by pharmacological facts. Number of iron chelators, have been revealed to scale down the intensity of symptoms of PD in patient.<sup>13-14</sup> Levodopa is (-)-3-(3,4-dihydroxyphenyl)-L-alanine, (Figure 1) is an alanine derivative, containing catechol moiety. Catechol has high

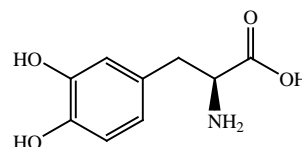


**Figure 1.** (-)-3-(3,4-Dihydroxyphenyl)-L-alanine commonly known as Levodopa.

## EXPERIMENTAL

Analytical grade reagents were used in all the experiments. Iron salts ( $\text{FeCl}_3 \cdot 6\text{H}_2\text{O}$  and  $(\text{NH}_4)_2\text{Fe}(\text{SO}_4)_2 \cdot 6\text{H}_2\text{O}$ ) were of Merck and Levodopa was obtained from Wild Wind. Stock and sample solutions were prepared in  $\text{CO}_2$  free distilled deionized water.

### Preparation of metal, ligand and buffer Solutions:

Accurate weight of Fe(II) and Fe(III) salts were dissolved in 100 mL volumetric flask, by using DDI water, to prepare solutions of desired concentration. To make buffers of pH 3.0, 4.0, 4.5, 5.0, 5.5 and 6.0, 100 mL of 1.0 M standardized NaOH solution was taken, its pH was altered by adding varying volumes of 1 M  $\text{CH}_3\text{COOH}$  to get the desired buffer value. Final volume was made up to 1 L with Deionized distilled water, ionic strength ( $\mu$ ) of 0.1 M of all buffer solutions were maintained. The buffer solutions of pH 7.4 and 9.2 were prepared by 2.0 M solution of Tris Base, with the ionic strength of 0.1 M.

### Kinetic measurements

The temperature was maintained at  $25 \pm 1^\circ\text{C}$ , throughout the experiment. All experiments were carried out in triplicate. Concentration of the metal ion was kept constant throughout the experiments, whereas that of the ligand was

kept from 1:1 to 100 folds, in order to get pseudo first order conditions. Flasks were plugged with stopper, mixed well and analyzed on Genesys 6 Thermo Electron Conformation for the recording of absorbance at  $\lambda_{\max}$ . The reactions of Fe(III) are extremely fast and were studied on stopped flow apparatus, manufactured by Applied Photo Physics. For machine and user interface, Global Oils Work software used in stopped flow apparatus. Only limited work was carried on Fe(III) because of unavailability of facilities.

## RESULTS AND DISCUSSION

The kinetical curves for complex formation between Fe(III) and Fe(II) in non-buffered media can be seen in Fig. 2 and 3.

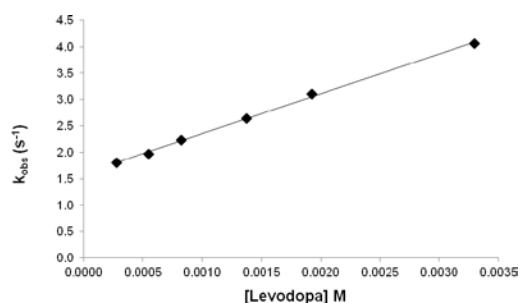


**Figure 2.** Plots of  $k_{\text{obs}}$  vs [Levodopa] for the formation of Fe(III)-LD in non-buffered medium;  $\lambda_{\max}=730$  nm.

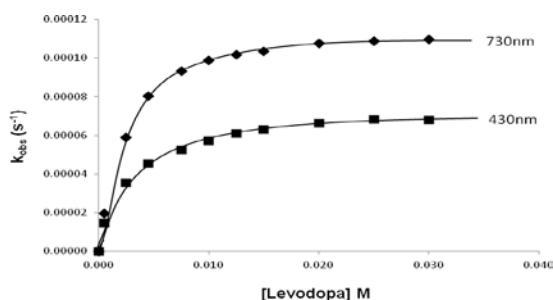


**Figure 3.** Plots of  $k_{\text{obs}}$  vs [Levodopa] for the formation of Fe(II)-LD in non-buffered medium.

The complex formation reaction between Fe(II) and LD was also studied in non-buffered and buffered media at  $25^\circ\text{C} \pm 1^\circ\text{C}$ . The corresponding plots of  $k_{\text{obs}}$  v/s [LD] at various pH, 4.0, 4.5, 5.0, 5.5, 6.0, 7.4 and 9.2 are given in Figs. 4 to 10, respectively.

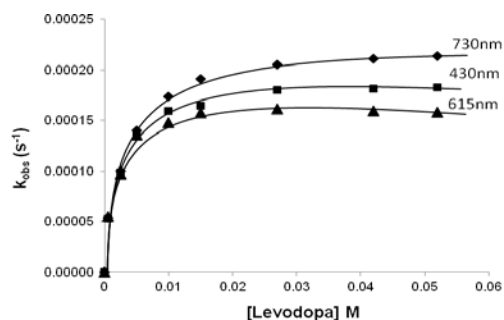


**Figure 4.** Plots of  $k_{\text{obs}}$  vs [Levodopa] for the formation of Fe(II)-LD Complex at pH 4.0.

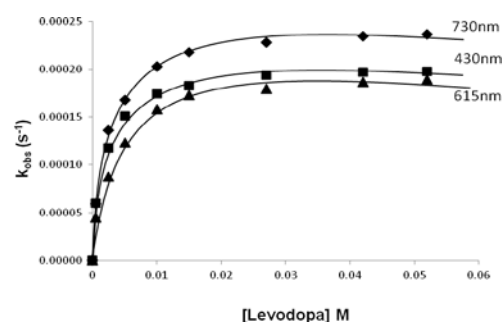


**Figure 5.** Plots of  $k_{\text{obs}}$  vs [Levodopa] for the formation of Fe(II)-LD complex at pH 4.5.

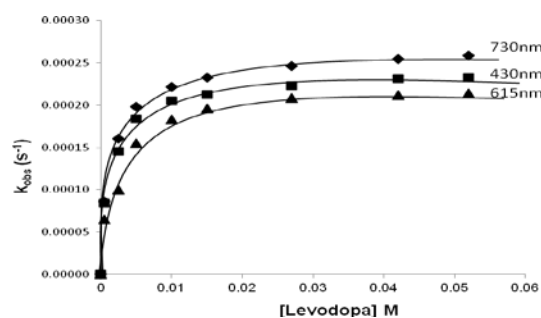


**Figure 6.** Plots of  $k_{\text{obs}}$  vs [Levodopa] for the formation of Fe(II)-LD complex at pH 5.0.

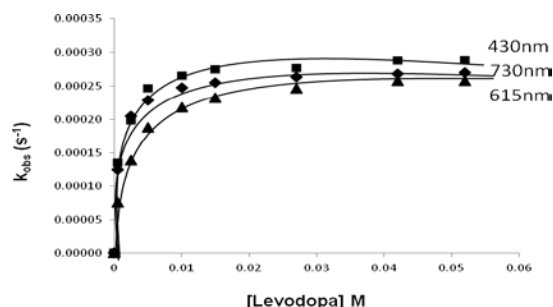


**Figure 7.** Plots of  $k_{\text{obs}}$  vs [Levodopa] for the formation of Fe(II)-LD complex at pH 5.5.

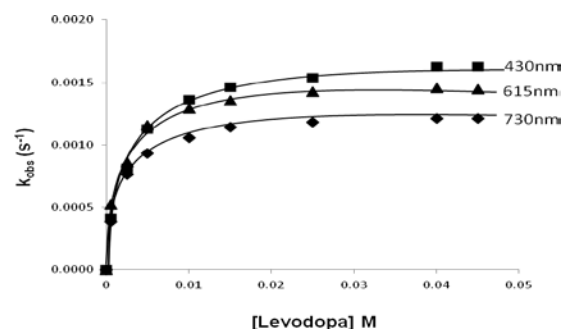


**Figure 8.** Plots of  $k_{\text{obs}}$  vs [Levodopa] for the formation of Fe(II)-LD complex at pH 6.0.

Reactions at pH range 4 to 5.5 were found to be slow, while, those at pH 6, 7.4 and 9.2 were very fast and hence were followed using stopped flow technique.

## Kinetics

The kinetics of formation of Fe(II)-LD and Fe(III)-LD complexes under the experimental conditions were studied spectrophotometrically. These reactions were studied in non-buffered solutions which were further observed under varying conditions of pH, using buffer solutions.

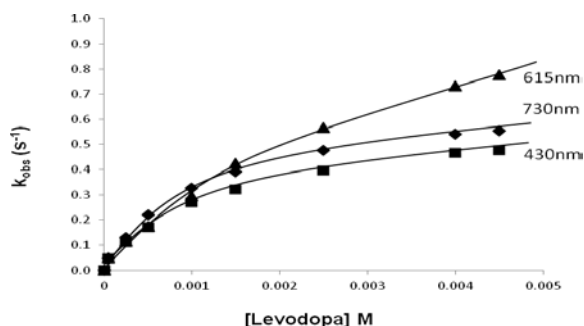


**Figure 9.** Plots of  $k_{obs}$  vs [Levodopa] for the formation of Fe(II)-LD complex at pH 7.0.

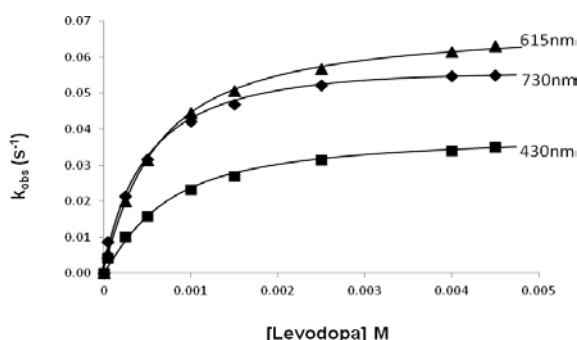


**Figure 10.** Plots of  $k_{obs}$  vs [Levodopa] for the formation of Fe(II)-LD complex at pH 9.2.

In the existing experiment  $k_{obs}$  values were evaluated from the slopes of plots of  $\ln |A_t - A_\infty|$  vs time. The kinetic results were fit to the eqn (1).

$$\ln[A_t - A_\infty] = e^{k_{obs} \times t} \quad (1)$$

The experimental rate constants reported here, are the average of three runs.  $k_{obs}$  versus ligand concentration plots showed hyperbolic and linear relationship, in different cases depending on the oxidation state of the metal. These linear and hyperbolic curves, indicated saturation and non-saturation behaviour with respect to the concentration of ligand in the sample. In the case of Fe(II), the hyperbolic dependence of  $k_{obs}$  on the [LD] suggests two pathways of the reaction, while in Fe(III) a linear pathway was observed.

### Fe(III)-LD complex in aqueous (non-buffered) medium

The sample analysis was performed on Stopped-flow machine which was attached with the UV-visible spectrophotometer. The reason to choose this technique is

because the reactions were founded very fast and accomplished within millisecond time scale.

The plot of the  $k_{obs}$  values vs. [LD], at 730 nm is presented in Fig 2. The nonzero intercept and the linearity in the plot are indicative of two term rate law for the reaction of complex formation.

$$k_{obs} = k_0 + k [LD] \quad (2)$$

where

$k_0$  indicates the rate constant for the independent pathway,<sup>[3]</sup> while

$k'$  is the rate constant for the pathway that depends upon [LD].

Values of  $k_0$  were compared with  $k$  and were found to be negligible.

$$k_0 \ll k$$

As the values of  $k_0$  are insignificant they may be taken as negligible. Therefore, it is concluded that,

$$k_{obs} = k [LD] \quad (3)$$

and

$$\text{Rate} = k_{obs} [\text{Fe(III)}] \quad (4)$$

### Fe(II)-LD complex in non-buffered medium

Formation kinetics of Fe(II)-LD in aqueous solution was examined at  $25 \pm 1$  °C. Hyperbolic relationship was observed between  $k_{obs}$  and [L], which is followed by Eqn (4).

$$k_{obs} = \frac{k'[L]}{1+k''[L]} \quad (4)$$

where [L] denotes the concentration of ligand, LD.

In this model parameter  $k'$  represents the 2<sup>nd</sup> order rate constant,  $k''$  defines the approach to saturation and has the units of equilibrium constant. The  $k_{max}$  is evaluated by the ratio of  $k'/k''$ .  $k_{obs}$  is equal to  $k_{max}$ , when the rate approaches a plateau as a function of ligand saturation, while at low ligand concentrations it is equal to  $k'$ . Overlay plot of  $k_{obs}$  values for the Fe(II)-LD is given in Fig. 8.

### Fe(II)-LD complex in buffered medium pH 4.0 to 9.2

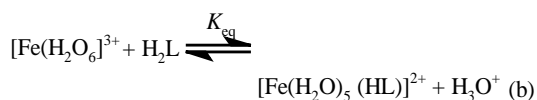
Kinetic parameters were calculated for Fe(II)-LD and the plots of  $k_{obs}$  vs. [LD], at pH span of 4.0 to 9.2, are shown in figure 4 to 10, at 430 nm, 615 nm and 730 nm. These plots are indicative of saturation kinetics with the reverence to [LD]. Fitting of the data to equation 4 gave the values of  $k$ ,  $k'$  and  $k''$  (Table 1).

**Table 1.** Kinetic parameters for the reaction of Fe(II) and Fe(III) with LD.

Fe(III)-LD at 730 nm					
Medium	R <sup>2</sup>	Sum of squares	k <sub>o</sub>	k	
	0.998453	5.48E-03	1.60	7.55E+02	
Fe(II)-LD at 430 nm					
Medium	R <sup>2</sup>	Sum of squares	k'	k''	k = k'/k''
Aqueous	0.996307	1.93E-11	2.68E-02	3.60E+02	7.45E-05
pH 4.0	0.991805	2.77E-10	9.98E-02	5.29E+02	1.89E-04
pH 4.5	0.994929	1.99E-10	1.28E-01	6.30E+02	2.03E-04
pH 5.0	0.990621	4.74E-10	1.94E-01	8.37E+02	2.32E-04
pH 5.5	0.986697	9.88E-10	4.00E-01	1.40E+03	2.85E-04
pH 6.0	0.993128	1.86E-08	7.06E-01	4.16E+02	1.70E-03
pH 7.4	0.995255	8.65E-04	4.88E+2	8.10E+02	6.02E-01
pH 9.2	0.997760	3.07E-06	5.33E+1	1.312E+3	4.06E-02
Fe(II)-LD at 615 nm					
pH 4.0	0.988901	2.92E-10	1.29E-01	7.77E+02	1.66E-04
pH 4.5	0.991773	3.10E-10	7.14E-02	3.58E+02	2.00E-04
pH 5.0	0.980497	9.12E-10	9.85E-02	4.41E+02	2.24E-04
pH 5.5	0.990313	6.37E-10	1.38E-01	5.22E+02	2.64E-04
pH 6.0	0.987146	2.63E-08	1.99E+00	7.43E+02	2.68E-03
pH 7.4	0.997066	1.61E-03	4.02E+02	2.98E+02	1.35E+00
pH 9.2	0.999767	1.07E-06	1.13E+02	1.58E+03	7.15E-02
Fe(II)-LD at 730 nm					
Aqueous	0.998427	2.28E-11	5.04E-02	4.18E+02	1.20E-04
pH 4.0	0.990804	4.33E-10	8.11E-02	3.62E+02	2.24E-04
pH 4.5	0.997425	1.48E-10	1.25E-01	5.10E+02	2.44E-04
pH 5.0	0.992513	4.68E-10	1.94E-01	7.53E+02	2.57E-04
pH 5.5	0.995616	2.84E-10	4.14E-01	1.55E+03	2.67E-04
pH 6.0	0.995353	6.73E-09	8.65E-01	6.99E+02	1.24E-03
pH 7.4	0.998615	3.49E-04	6.33E+02	9.25E+02	6.84E-01
pH 9.2	0.997923	7.04E-06	1.38E+02	2.27E+03	6.07E-02

### Proposed mechanism for saturation pathway of Fe(II)-LD chelation

On the basis of observations and fitting of the data to specified equations, following mechanism can be proposed for saturation pathway.



$$\text{Rate} = \frac{d[\text{Fe}(\text{L})_n^{+1}]}{dt} = k_1[\text{FeL}]^{1+} \quad (5)$$

as we know that

$$K_{\text{eq}} = \frac{[\text{FeL}]^{1+}}{[\text{Fe}^{3+}][\text{L}^{2-}]} \quad (6)$$

$$[\text{Fe}^{3+}]_{\text{T}} = [\text{Fe}^{3+}] + [\text{FeL}]^{1+} \quad (7)$$

$$[\text{Fe}^{3+}] = [\text{Fe}^{3+}]_{\text{T}} - [\text{FeL}]^{1+} \quad (8)$$

$$[\text{FeL}]^{1+} = K_{\text{eq}} [\text{Fe}^{3+}]_{\text{T}} [\text{L}^{2-}] - K_{\text{eq}} [\text{FeL}]^{1+} [\text{L}^{2-}]$$

$$[\text{FeL}]^{1+} + K_{\text{eq}} [\text{FeL}]^{1+} [\text{L}^{2-}] = K_{\text{eq}} [\text{Fe}^{3+}]_{\text{T}} [\text{L}^{2-}]$$

$$[\text{FeL}]^{1+} (1 + K_{\text{eq}} [\text{L}^{2-}]) = K_{\text{eq}} [\text{Fe}^{3+}]_{\text{T}} [\text{L}^{2-}]$$

$$[\text{FeL}]^{1+} = \frac{K_{\text{eq}} [\text{Fe}^{3+}]_{\text{T}} [\text{L}^{2-}]}{1 + K_{\text{eq}} [\text{L}^{2-}]} \quad (9)$$

$$\text{Rate} = k [\text{FeL}]^{1+}$$

$$\text{Rate} = \frac{k \times K_{\text{eq}} [\text{Fe}^{3+}]_{\text{T}} [\text{L}^{2-}]}{1 + K_{\text{eq}} [\text{L}^{2-}]} \quad (10)$$

$$\text{Rate} = k_{\text{obs}} [\text{Fe}^{3+}]_{\text{T}}$$

$$k_{\text{obs}} = \frac{k \times K_{\text{eq}}[\text{L}^2]}{1 + K_{\text{eq}}[\text{L}^2]} \quad (11)$$

Final rate law is eqn. (12).

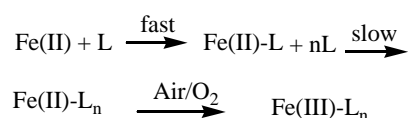
$$\text{Rate} = \frac{k \times K_{\text{eq}}[\text{L}^2] \times [\text{Fe}^{3+}]}{1 + K_{\text{eq}}[\text{L}^2]} \quad (12)$$

We have assumed that  $k \times K_{\text{eq}} = k'$  and  $K_{\text{eq}} = k''$ .

So,  $k = k'/k''$ .

### Effect of pH

Water exchange rate constant of  $\text{Fe}(\text{H}_2\text{O})_6^{2+}$  is  $4.4 \times 10^6$ , and that of  $\text{Fe}(\text{H}_2\text{O})_6^{3+}$  is  $1.6 \times 10^2$ .<sup>18</sup> As the  $\text{H}_2\text{O}$  exchange in  $\text{Fe}^{2+}(\text{aq})$  is 10,000 times faster than  $\text{Fe}^{3+}(\text{aq})$ , our results are in good agreement with this literature value, when the complexation reaction is carried, starting with  $\text{Fe}^{3+}$ . When  $\text{Fe}^{2+}$  was used as metal ion source, the reaction was found to be  $10^{10}$  times slower. The reason for this observation might be multistep reaction, involving oxidation of  $\text{Fe}^{2+}$  to  $\text{Fe}^{3+}$ , which is catalyzed by the presence of LD. As  $\text{Fe}^{3+}$ , a  $d^5$  system is inert for substitution, the preferred reaction should be as follows.



On the other hand,  $d^5$  system has low CFAE, and is highly inert regardless of nature of ligand. However,  $d^6$  with strong field is extremely inert. The coordination of 1<sup>st</sup> LD molecule with  $\text{Fe}^{2+}$  might make it highly inert and therefore, the further reaction slows down unexpectedly. LD exhibits LMCT bands only when it is coordinated with higher oxidation states of metal ion. Hence, the complex formation with  $\text{Fe}^{3+}$  would be preferred in this case.<sup>19-20</sup>

The reaction was studied at various pH values and the data presented here shows that the saturation pathway is important at higher pH. At pH 6.0 the reaction is too fast. At pH 7.4 and 9.2 again the same path is followed and the values of rate constants are higher than at lower pH.

This is well documented that the iron LD complexation process is highly pH dependent and lowering the pH would cause a slower rate of reaction. Iron complex formation with LD is prohibited in highly acidic media where  $\text{pH} < 4.0$ .<sup>21</sup>

A significant change in the values of  $k_{\text{obs}}$  in the experimental concentration range of LD, suggests that pH is the main trigger for iron complexation process and the data suggests that the chelation process is also following saturation pathway in the case of Fe(II). We can conclude here that the first-order pathway is dominating over the saturation pathway.

### Effect of pH on the value of $k_{\text{obs}}$ at different $\lambda_{\text{max}}$

According to the values of  $k_{\text{obs}}$  given in the Table 1, the following order at different wavelengths was observed.

The calculated values for kinetic parameters for chelation of Fe(II) with LD at pH 4.0, 4.5 and 5.0, are in the order of  $615 \text{ nm} < 430 \text{ nm} < 730 \text{ nm}$ , while at pH 5.5, the sequence was changed to  $615 \text{ nm} < 730 \text{ nm} < 430 \text{ nm}$ . It is observed in Fig. 8, that peak shifting is very clear at pH 6.0. Values at 730 nm, decrease in contrast to the values at 615 nm and 430 nm, and stands as  $730 \text{ nm} < 615 \text{ nm} < 430 \text{ nm}$ . The trend of the  $k_{\text{obs}}$  values for Fe(II)-LD chelation under the provided conditions, are exactly reverse of the one observed at pH 5.5,  $430 \text{ nm} < 730 \text{ nm} < 615 \text{ nm}$ .

### Statistical proof of the pH dependence of $k_{\text{obs}}$

The SigmaPlot™ Ver. 12.0 statistical software was employed to determine the statistics i.e. significant difference of the kinetic data of Fe<sup>II</sup>-LD complex at different pH and different wavelengths using the One Way ANOVA and Pair *t*-test method.

One Way ANOVA: One Way ANOVA ( $P < 0.050$ ) at SigmaPlot™ software is applied for  $k_{\text{obs}}$  values. Outcome of such statistics is that at different pH all wavelengths (430, 615 and 730 nm) are significantly different. It reflects that with increase or change in pH (4.0 to 9.2) at each wavelength  $k_{\text{obs}}$  values are not agreed with each other. The result verifies that the Fe(II)-LD complexation is pH dependent.

One way ANOVA for the set of all  $k_{\text{obs}}$  values at different wavelength at particular pH, shows overall results ( $p < 0.050$ ) of no significant difference among the kinetics data at all three wavelengths.

Pair *t*-test: The Pair *t*-test was applied on the same set of all pH data at particular wavelengths. The overall result of such statistics ( $P < 0.050$ ) also shows the same significant difference reconfirming the pH dependency of the reaction.

The data of all three wavelengths at respective pH were also evaluated by Student's 't' test. The results of statistics ( $P < 0.050$ ) show no significant difference among the kinetics of different wavelength at same pH. This consequence proves the same reaction was measured on different wavelengths at respective pH.

### CONCLUSION

No complexation was detected below pH 4.5. This is another point of evidence for the existence of Fe in complexes in +3 oxidation state (Fe at low pH exists in  $\text{Fe}^{+2}$  form and is not oxidized).

Formation of complex at pH 4 or higher suggests that no interaction between metal and ligand takes place in stomach, but as the ligand moves through the blood the complexation with body iron becomes important. This interaction may lead to anemia.

Complexation at pH 9.2 shows that Fe-LD complexes might exist in brain because Parkinson's disease is also characterized by iron overload in the brain and the deficiency of Dopamine can be a consequence of excess amounts of iron in brain.<sup>7-10</sup>

## REFERENCES

- <sup>1</sup>Yoshikawa, S. and Caughey, W., Infrared evidence of cyanide binding to iron and copper sites in bovine heart cytochrome c oxidase. Implications regarding oxygen reduction, *J. Biol. Chem.*, **1990**, *265*, 7945-7958. <http://intl.jbc.org/cgi/content/abstract/265/14/7945>
- <sup>2</sup>Weinberg, J., Harding, P. and Humes, H., Mitochondrial bioenergetics during the initiation of mercuric chloride-induced renal injury. I. Direct effects of in vitro mercuric chloride on renal mitochondrial function, *J. Biol. Chem.*, **1982**, *257*, 60-67.
- <sup>3</sup>Zaidi S. Z. A. and Fatima, N. Interaction of Antiparkinsonian Drug molecule, (-)-3-(3,4-dihydroxyphenyl)-L-alanine with Bioessential Metals Study by Simple Spectrophotometric Method, *Int. J. Adv. Res.*, **2015**, *3*, 1009-1018.
- <sup>4</sup>Galvani, P. Colleoni, M. Origi M. and Santagostino, A., Mitochondrial toxicity of iron and the protective role of ferritin on dopaminergic PC12 cell line, *Toxicol. in vitro*, **1995**, *9*, 365-368. [https://doi.org/10.1016/0887-2333\(95\)00031-3](https://doi.org/10.1016/0887-2333(95)00031-3)
- <sup>5</sup>Burdo J. R. and Connor, J. R. Brain iron uptake and homeostatic mechanisms: an overview, *Biometals*, **2003**, *16*, 63-75. <https://doi.org/10.1023/A:1020718718550>
- <sup>6</sup>Pappolla, M. Omar, R. Kim K. and Robakis, N., Immunohistochemical evidence of oxidative [corrected] stress in Alzheimer's disease, *Am. J. Pathol.*, **1992**, *140*, 621.
- <sup>7</sup>Maynard, C. J., Cappai, R., Volitakis, I., Cherny, R. A., White, A. R., Beyreuther, K., Masters, C. L., Bush A. I. and Li, Q.-X., Overexpression of Alzheimer's disease amyloid- $\beta$  opposes the age-dependent elevations of brain copper and iron, *J. Biol. Chem.*, **2002**, *277*(47), 44670-6. DOI: [10.1074/jbc.M204379200](https://doi.org/10.1074/jbc.M204379200)
- <sup>8</sup>Shachar, D. B., Kahana, N., Kampel, V., Warshawsky A. and Youdim, M. B., Neuroprotection by a novel brain permeable iron chelator, VK-28, against 6-hydroxydopamine lesion in rats, *Neuropharmacology*, **2004**, *46*, 254-263. <https://doi.org/10.1016/j.neuropharm.2003.09.005>
- <sup>9</sup>Kaur, D., Yantiri, F., Rajagopalan, S., Kumar, J., Mo, J. Q., Boonplueang, R., Viswanath, V., Jacobs, R., Yang L. and Beal, M. F., Genetic or pharmacological iron chelation prevents MPTP-induced neurotoxicity in vivo: a novel therapy for Parkinson's disease, *Neuron*, **2003**, *37*, 899-909. [https://doi.org/10.1016/S0896-6273\(03\)00126-0](https://doi.org/10.1016/S0896-6273(03)00126-0)
- <sup>10</sup>Hirsch, E., Graybiel A. M. and Agid, Y. A., Melanized dopaminergic neurons are differentially susceptible to degeneration in Parkinson's disease, *Nature*, **1988**, *334*, 345-348. <https://doi.org/10.1038/334345a0>
- <sup>11</sup>Chinta, S. J. and Andersen, J. K., Dopaminergic neurons, *Int. J. Biochem. Cell Biol.*, **2005**, *37*, 942-946. <https://doi.org/10.1016/j.biocel.2004.09.009>
- <sup>12</sup>Linert, W. and Jameson, G., Redox reactions of neurotransmitters possibly involved in the progression of Parkinson's Disease, *J. Inorg. Biochem.*, **2000**, *79*, 319-326. [https://doi.org/10.1016/S0162-0134\(99\)00238-X](https://doi.org/10.1016/S0162-0134(99)00238-X)
- <sup>13</sup>Paris, I., Martinez-Alvarado, P., Cárdenas, S., Perez-Pastene, C., Graumann, R., Fuentes, P., Olea-Azar, C., Caviades P. and Segura-Aguilar, J., Dopamine-dependent iron toxicity in cells derived from rat hypothalamus, *Chem. Res. Toxicol.*, **2005**, *18*, 415-419. <https://doi.org/10.1021/tx0497144>
- <sup>14</sup>Iffat, A., Maqsood Z. and Fatima, N., Study of complex formation of Fe(III) with tannic acid, *J. Chem. Soc. Pak.*, **2005**, *27*, 174.
- <sup>15</sup>Fatima, N., Zaidi, S., Nisar S. and Qadri, M., pH Effect on Stoichiometry and Stability of Ferrous Complexes of (-)-3-(3,4-dihydroxyphenyl)-L-alanine, *Pak. J. Chem.*, **2013**, *3*, 23-28. <https://doi.org/10.15228/2013.v03.i01.p04>
- <sup>16</sup>Siddiq, F. Fatima, I. Malik, A. Afza, N. Iqbal, L. Lateef, M. Hameed S. and Khan, S. W., Biologically active bergenin derivatives from *Bergenia stracheyi*, *Chem. Biodiver.*, **2012**, *9*, 91-98. <https://doi.org/10.1002/cbdv.201100003>
- <sup>17</sup>Atwood, J. D., *Inorganic and organometallic reaction mechanisms*, VCH Publishers, **1997**.
- <sup>18</sup>Zaidi S. Z. A. and Fatima, N., A Comparative Study for Chelation of Iron (II) and Iron (III) with Levodopa - An Antiparkinsonian Drug Molecule, *Eur. Chem. Bull.*, **2014**, *3*, 648-653. DOI: <http://dx.doi.org/10.17628/ecb.2014.3.648-653>
- <sup>19</sup>Fiaz, T., Fatima, N., Zaidi, S. Z. A., Abbas T. and Kazimi, M. R., Investigation of Iron Complex Formation of Anti-Hypertensive Drug: Methyl dopa, *Am. J. Anal. Chem.*, **2015**, *6*, 551. <https://doi.org/10.4236/ajac.2015.66053>
- <sup>20</sup>Fiaz, T., Fatima, N., Zaidi S. Z. A. and Kazimi, T. A. M. R., Investigation of iron complex formation of antihypertensive drug methyl dopa was studied, *Am. J. Anal. Chem.*, **2016**, *6*, 551-558. <https://doi.org/10.4236/ajac.2015.66053>
- <sup>21</sup>Lewis, R. A., Austen K. F. and Soberman, R. J., Leukotrienes and other products of the 5-lipoxygenase pathway: biochemistry and relation to pathobiology in human diseases, *New Engl. J. Med.*, **1990**, *323*, 645-655. <https://doi.org/10.1056/NEJM199009063231006>

Received: 04.08.2019.

Accepted: 11.04.2020.



# INTERACTION OF NINHYDRIN WITH *N*-HYDROXYUREA AND *N*-ALKOXYUREAS IN ACETIC ACID

Vasiliy G. Shtamburg,<sup>[a]\*</sup> Victor V. Shtamburg,<sup>[a]</sup> Andrey A. Anishchenko,<sup>[b]</sup> Svitlana V. Shishkina,<sup>[c]</sup> Irina S. Konovalova<sup>[c]</sup> and Alexander V. Mazepa<sup>[d]</sup>

**Keywords:** Ninhydrin, *N*-hydroxyurea, *N*-alkoxyureas, synthesis, structure, C–C bond elongation.

We have found that ninhydrin reacted with *N*-hydroxyurea and *N*-alkoxyureas in acetic acid with the predominant formation of diastereomers of 1,3a,8a-trihydroxy-1,3,3a,8a-tetrahydroindeno[1,2-*d*]imidazole-2,8-dione and 1-alkoxy-3a,8a-dihydroxy-1,3,3a,8a-tetrahydroindeno[1,2-*d*]imidazole-2,8-diones, respectively, with *sic*-orientation of 3a,8a-HO-groups. The X-ray structural analysis of 1,3a*S*,8a*R*-trihydroxy-1,3,3a,8a-tetrahydroindeno[1,2-*d*]imidazole-2,8-dione and 1-*n*-butyloxy-3a*S*,8a*R*-dihydroxy-1,3,3a,8a-tetrahydroindeno[1,2-*d*]imidazole-2,8-dione has demonstrated their specific structural features.

## \* Corresponding Authors

Phone: +380-97-651-61-72

E-Mail: stamburg@gmail.com

[a] 49005 Ukraine, Dnepr, Gagarina st., 8. Ukrainian State University of Chemical Technology.

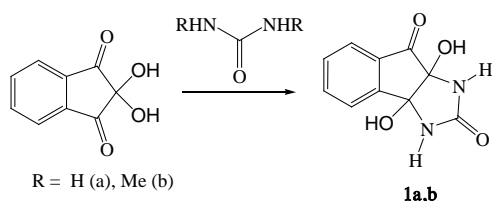
[b] 49050 Ukraine, Dnepr, Nauchnaya st. 25. O. Gonchar Dnepropetrovsk National University.

[c] 61001 Ukraine, Kharkov, Science ave., 60. SSI "Institute for Single Crystals", National Academy of Sciences of Ukraine.

[d] 65080 Odessa, Luystdorskaya Doroga st., 86. A.V. Bogatsky Physico-Chemical Institute of NAS of Ukraine.

## INTRODUCTION

Nitrogen-containing heterocyclic systems, such as hydantoin and imidazolidin-2-ones, are common in pharmaceutical materials. It is therefore important to create the reaction strategies that give access to such biologically active synthones. As it is known,<sup>1-4</sup> ninhydrin (indane-1,2,3-trione hydrate) reacts with urea and *N,N'*-dimethylureas yielding 3a,8a-dihydroxy-1,3,3a,8a-tetrahydroindeno[1,2-*d*]imidazole-2,8-diones (**1a,b**) (Scheme 1).

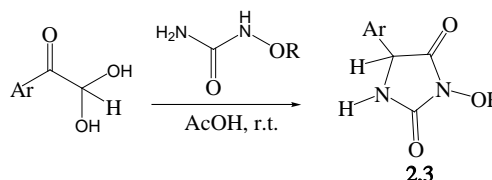


**Scheme 1.** Ninhydrin's interaction with the ureas.

Compounds **1a,b** were used as the essential intermediates in the diastereoselective synthesis of some dihydrofuran derivatives<sup>3</sup> and pharmaceuticals.<sup>3,5</sup>

The study of the vicinal polycarbonyl compounds interaction with *N*-hydroxyurea and its derivatives<sup>6-10</sup> has recently been started by our research group and needs to be continued. Derivatives of *N*-hydroxyurea are common in pharmaceuticals. But the ninhydrin's interaction with *N*-hydroxyurea and *N*-alkoxyureas has not been investigated in contrast to the arylglyoxal reactions with *N*-hydroxyurea and *N*-alkoxyureas.<sup>6-10</sup>

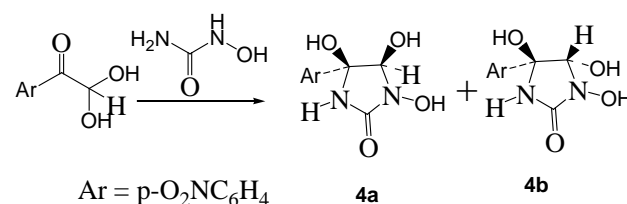
Earlier we have found<sup>8</sup> that most of arylglyoxals reacted with *N*-hydroxyurea and *N*-alkoxyureas in acetic acid producing 3-hydroxyhydantoin **2** and 3-alkoxyhydantoin **3** (Scheme 2).



Ar = *p*-XC<sub>6</sub>H<sub>4</sub>, X = H (a), F(b), Cl(c), Br(d)  
R = H(2), Me, Et, Bu(3)

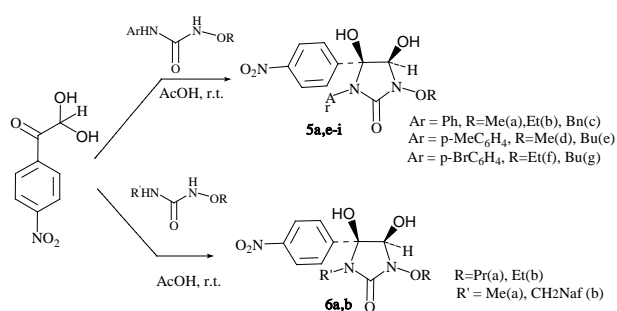
**Scheme 2.** Interaction of the most of arylglyoxals with *N*-hydroxyurea and *N*-alkoxyureas in the acetic acid.

In aqueous medium this reaction can have ambiguous results and the product's nature strongly depends on the nature of arylglyoxal.<sup>6</sup> 4-Nitrophenylglyoxal, however, reacts with *N*-hydroxyurea producing<sup>9</sup> the mixture of 5-aryl-3,4,5-trihydroxyimidazolidin-2-ones **4a** and **4b** in molar ratio approximately 3:1 (Scheme 3).



**Scheme 3.** Interaction of 4-nitrophenylglyoxal with *N*-hydroxyurea.

Moreover, 4-nitrophenylglyoxal diastereoselectively reacts with *N*-alkoxy-*N'*-arylsureas and *N*-alkoxy-*N'*-alkylureas in acetic acid at 17–20° C mainly producing 3-alkoxy-1-aryl-4*S*,5*S*-dihydroxy-5-(4-nitrophenyl)imidazolidin-2-ones **5** and 3-alkoxy-1-alkyl-4*S*,5*S*-dihydroxy-5-(4-nitrophenyl)imidazolidin-2-ones **6**.<sup>10</sup> These diastereomers **5,6** have *cis* orientation of 4-HO- and 5-HO-moieties (Scheme 4).



**Scheme 4.** Interaction of 4-nitrophenylglyoxal with *N*-alkoxy-*N'*-arylureas and *N*-alkoxy-*N'*-alkylureas.

Thus the goal of our present research is to investigate the interaction of ninhydrin with *N*-hydroxyurea and *N*-alkoxyureas in acetic acid medium.

## EXPERIMENTAL

<sup>1</sup>H NMR spectra were recorded on a Varian VXP-300 spectrometer (300 MHz). <sup>13</sup>C NMR spectra were recorded on a Varian VXP-300 spectrometer (75 MHz). The solvent DMSO-*d*<sub>6</sub> was used. <sup>1</sup>H NMR chemical shifts relative to the residual solvent protons as an internal standard [(CD<sub>3</sub>)<sub>2</sub>SO: 2.500 ppm] were reported. Solvent carbon atoms served as an internal standard for <sup>13</sup>C NMR spectra [(CD<sub>3</sub>)<sub>2</sub>SO: 39.52 ppm]. Mass spectra were recorded on a VG 70-70EQ mass spectrometer in fast atom bombardment mode (FAB). The solvents were purified and dried according to the standard procedures.

### 1,3a,8a-Trihydroxy-1,3,3a,8a-tetrahydroindeno[1,2-*d*]imidazole-2,8-dione (7)

**A.** *N*-Hydroxyurea (74.6 mg, 0.981 mmol) was dissolved in a solution of ninhydrin (145.6 mg, 0.817 mmol) in acetic acid (7 mL) by stirring at 16 °C. The reaction solution was maintained at 8 °C for 23 h, then it was heated to 16 °C, the obtained white precipitate was filtered out, dried under vacuum (3 mmHg) at 25 °C, washed with MeCN (2 mL) and dried under vacuum (3 mmHg), giving 190 mg (98 %) *cis*-3a,8a-dihydroxydiastereomer of **7**, colorless crystals, m. p. 169–171 °C (with decomp.), m. p. 172–174 °C (with decomp., THF–hexane). <sup>1</sup>H NMR (300 MHz, DMSO-*d*<sub>6</sub>) δ = 6.646 (1H, s, OH), 7.268 (1H, s, OH), 7.615 (1H, t, *J* = 7.5 Hz, Ar), 7.750 (1H, d, *J* = 7.2 Hz, Ar), 7.762 (1H, d, *J* = 7.2 Hz, Ar), 7.859 (1H, t, *J* = 7.5 Hz, Ar), 8.409 (1H, s, NH), 9.131 (1H, s, NOH). <sup>13</sup>C NMR (75 MHz, DMSO-*d*<sub>6</sub>) δ = 84.33 (C–OH), 89.36 (C–OH), 123.44 [C(H) Ar], 124.92 [C(H) Ar], 130.46 [C(H) Ar], 132.28 [C<sub>q</sub> Ar], 136.53 [C(H) Ar], 150.82 [C<sub>q</sub> Ar], 156.05 [HN(C=O)NOH], 195.63 (C=O). MS (FAB) *m/z* 237 [M+H]<sup>+</sup> (90), 176 [M+H-H<sub>2</sub>O-HCNO]<sup>+</sup> (68), 90(57), 72(100). Anal. Calc. for C<sub>10</sub>H<sub>8</sub>N<sub>2</sub>O<sub>5</sub>: C 50.85, H 3.41, N 11.86. Found: C 50.87, H 3.51, N 11.69.

**B.** Ninhydrin (149.1 mg, 0.837 mmol) was dissolved in the solution of *N*-hydroxyurea (71.6 mg, 0.941 mmol) in acetic acid (5 mL) by stirring at 20 °C for 3 h. The obtained white precipitate was filtered out, dried under vacuum (3 mmHg) at 25 °C, yielding 182.3 mg (92 %) of *cis*-3a,8a-

dihydroxydiastereomer **7**, colorless crystals, m. p. 169–171 °C (with decomp.).

### 1-Methoxy-3a*S*,8a*R*-dihydroxy-1,3,3a,8a-tetrahydroindeno[1,2-*d*]imidazole-2,8-dione (8a)

**A.** Ninhydrin (150.3 mg, 0.844 mmol) was dissolved in the solution of *N*-methoxyurea (76 mg, 0.844 mmol) in acetic acid (6 mL) by stirring at 20 °C for 1 h. The reaction solution was maintained at 20 °C for 1 h, maintained at 5 °C for 20 h, then acetic acid was evaporated under vacuum (3 mmHg) at 18 °C, the residue was extracted with water (3 mL) at 5 °C. The obtained precipitate was filtered off, dried under vacuum (3 mmHg) giving 142 mg (67 %) of *cis*-3a,8a-dihydroxydiastereomer of **8a**, colorless crystals, m. p. 197–199 °C (with decomp., THF–hexane). <sup>1</sup>H NMR (300 MHz, DMSO-*d*<sub>6</sub>) δ = 3.598 (3H, s, NOME), 6.792 (1H, s, OH), 7.524 (1H, s, OH), 7.632 (1H, t, *J* = 7.5 Hz, Ar), 7.748 (1H, d, *J* = 7.5 Hz, Ar), 7.784 (1H, d, *J* = 7.5 Hz, Ar), 7.879 (1H, t, *J* = 7.5 Hz, Ar), 8.663 (1H, s, NH). <sup>13</sup>C NMR (75 MHz, DMSO-*d*<sub>6</sub>): δ = 64.36 (NOME), 84.37 (C–OH), 88.92 (C–OH), 123.63 [C(H) Ar], 124.90 [C(H) Ar], 130.57 [C(H) Ar], 131.91 [C<sub>q</sub> Ar], 136.83 [C(H) Ar], 150.73 [C<sub>q</sub> Ar], 155.19 [N(C=O)N], 196.14 (C=O). MS (FAB) *m/z* 501(2M+H)<sup>+</sup> (10), 251 (M+H)<sup>+</sup> (100), 191 (30), 161 (16). Anal. Calc. for C<sub>11</sub>H<sub>10</sub>N<sub>2</sub>O<sub>5</sub>: C 52.80, H 4.03, N 11.20. Found: C 52.82, H 4.03, N 11.14.

**B.** Ninhydrin (130 mg, 0.730 mmol) was dissolved in the solution of *N*-methoxyurea (66 mg, 0.730 mmol) in acetic acid (6 mL) by stirring at 19 °C for 1 h. The reaction mixture was maintained at 16 °C for 2 h, then acetic acid was evaporated under vacuum (3 mmHg) at 20 °C, giving 182 mg (99 %) of mixture of *cis*-3a,8a-dihydroxydiastereomer **8a** (89 %) and *trans*-3a,8a-dihydroxydiastereomer **8b** (11 %). This mixture was extracted by water (10 mL) at 4 °C for 25 h, the precipitate was filtered off, washed with water (5 mL), the combined aqueous filtrate was evaporated under vacuum (3 mmHg) at 20 °C, giving 91 mg (50 %) of **8a**.

### 1-Ethoxy-3a*S*,8a*R*-dihydroxy-1,3,3a,8a-tetrahydroindeno[1,2-*d*]imidazole-2,8-dione (9a)

**A.** Ninhydrin (214.9 mg, 1.206 mmol) was dissolved in the solution of *N*-ethoxyurea (125.6 mg, 1.206 mmol) in acetic acid (6 mL) by stirring at 14 °C for 6 h, the reaction solution was maintained at 17 °C for 22 h, then it was frozen and acetic acid was evaporated under vacuum (3 mmHg). The obtained residue was washed with water (2 mL) at 5 °C, dried under vacuum (3 mmHg), giving 230 mg (72 %) of *cis*-3a,8a-dihydroxydiastereomer **9a**, colorless crystals, m. p. 161–163 °C (with decomp., THF–hexane). <sup>1</sup>H NMR (300 MHz, DMSO-*d*<sub>6</sub>): δ = 1.072 (3H, t, *J* = 7.0 Hz, NOCH<sub>2</sub>Me), 3.731–3.894 (2H, m, NOCH<sub>2</sub>Me), 6.795 (1H, s, OH), 7.488 (1H, s, OH), 7.625 (1H, t, *J* = 7.5 Hz, Ar), 7.751 (1H, d, *J* = 7.2 Hz, Ar), 7.775 (1H, d, *J* = 7.2 Hz, Ar), 7.873 (1H, t, *J* = 7.5 Hz, Ar), 8.650 (1H, s, NH). <sup>13</sup>C NMR (75 MHz, DMSO-*d*<sub>6</sub>): δ = 13.73 (Me), 71.73 (NOCH<sub>2</sub>), 84.42 (C–OH), 89.14 (C–OH), 123.55 [C(H) Ar], 124.88 [C(H) Ar], 130.54 [C(H) Ar], 132.00 [C<sub>q</sub> Ar], 136.78 [C(H) Ar], 150.72 [C<sub>q</sub> Ar], 155.55 [N(C=O)N], 196.07 (C=O). MS (FAB) *m/z* 265 [M+H]<sup>+</sup> (100), 204 [M+H-H<sub>2</sub>O-HNCO]<sup>+</sup> (95), 177 (31), 161 (21), 150 (27), 131 (30), 105 (33). Anal. Calc. for C<sub>12</sub>H<sub>12</sub>N<sub>2</sub>O<sub>5</sub>: C 54.55, H 4.58, N 10.60. Found: C 54.38, H 4.30, N 10.70.

**B.** Ninhydrin (173 mg, 0.973 mmol) was dissolved in the solution of *N*-ethoxyurea (101 mg, 0.973 mmol) in acetic acid (6 mL) by stirring at 17 °C for 1.5 h, the reaction solution was maintained at 15 °C for 1.5 h, then it was frozen and acetic acid was evaporated under vacuum (3 mmHg). The obtained residue was washed with benzene (6 mL) at 10 °C and dried under vacuum (3 mmHg) giving 254 mg (99 %) mixture of diastereomes of *cis*-3a,8a-dihydroxydiastereomer **9a** (92 %) and *trans*-3a,8a-dihydroxydiastereomer **9b** (8 %). This mixture was extracted by water (12 mL) at 4 °C for 23 h, solid phase was filtered off, dried under vacuum (3mmHg), giving 174 mg (67.6 %) of *cis*-3a,8a-dihydroxydiastereomer **9a**.

#### 1-*n*-Butyloxy-3a*S*,8a*R*-dihydroxy-1,3,3a,8a-tetrahydroindeno[1,2-*d*]imidazole-2,8-dione (**10a**)

**A.** Ninhydrin (183 mg, 1.027 mmol) was dissolved in the solution of *N*-*n*-butyloxyurea<sup>11</sup> (136 mg, 1.027 mmol) in acetic acid (6 mL) by stirring at 18 °C for 3 h. The reaction solution was maintained at 18 °C for 21 h, then it was frozen and acetic acid was evaporated under vacuum (3 mmHg). The obtained residue was washed with water (4 mL) at 5 °C and dried under vacuum (3 mmHg) giving 229 mg (77 %) of *cis*-3a,8a-dihydroxydiastereomer **10a**, colorless crystals, m. p. 163-164 °C (with decomp.). <sup>1</sup>H NMR (300 MHz, DMSO-*d*<sub>6</sub>): δ = 0.852 (3H, t, *J* = 7.2 Hz, NO(CH<sub>2</sub>)Me), 1.335 (2H, sex, *J* = 7.2 Hz, NOCH<sub>2</sub>CH<sub>2</sub>CH<sub>2</sub>Me), 1.464 (2H, quint, *J* = 7.2 Hz, NOCH<sub>2</sub>CH<sub>2</sub>CH<sub>2</sub>Me), 3.706–3.857 (2H, m, NOCH<sub>2</sub>), 6.750 (1H, s, OH), 7.390 (1H, s, OH), 7.618 (1H, t, *J* = 7.2 Hz, Ar), 7.756 (1H, d, *J* = 6.6 Hz, Ar), 7.777 (1H, d, *J* = 6.6 Hz, Ar), 7.865 (1H, t, *J* = 7.2 Hz, Ar), 8.609 (1H, s, NH). <sup>13</sup>C NMR (75 MHz, DMSO-*d*<sub>6</sub>): δ = 13.77 (Me), 18.56 (CH<sub>2</sub>), 29.90 (CH<sub>2</sub>), 76.03 (NOCH<sub>2</sub>), 84.37 (C–OH), 89.08 (C–OH), 123.51 [C(H) Ar], 124.86 [C(H) Ar], 130.48 [C(H) Ar], 132.01 [C<sub>q</sub> Ar], 136.71 [C(H) Ar], 150.72 [C<sub>q</sub> Ar], 155.40 [N(C=O)N], 195.96 (C=O). MS (FAB) *m/z* 293 [M+H]<sup>+</sup>(100), 232 [M+H-H<sub>2</sub>O-HNCO]<sup>+</sup> (39), 177 (75), 161(23), 150 (15), 131 (25), 105 (14). Anal. Calc. for C<sub>14</sub>H<sub>16</sub>N<sub>2</sub>O<sub>5</sub>: C 57.53, H 5.52, N 9.58. Found: C 57.36, H 5.71, N 9.37.

**B.** Ninhydrin (138 mg, 0.774 mmol) was dissolved in the solution of *N*-*n*-butyloxyurea<sup>11</sup> (102 mg, 0.774 mmol) in acetic acid (6 mL) at stirring at 19 °C for 1h, the reaction solution was maintained at 17 °C for 2 h, then it frozen and acetic acid was evaporated under vacuum (3 mmHg). The obtained residue was washed by benzene (3 mL), dried under vacuum, giving 209 mg (92%) of *cis*-3a,8a-dihydroxydiastereomer**10a** and *trans*-3a,8a-dihydroxydiastereomer**10b** (94:6). This mixture was extracted by water (5.5 mL) at 4 °C for 26 h, the white precipitate was filtered off, washed with cold water (3.5 mL) and dried under vacuum (3 mmHg) at 20 °C, to give 148 mg (65 %) *cis*-3a,8a-dihydroxydiastereomer **10a**, white powder, m. p. 160-161 °C (with decomp.).

#### 1-Benzoyloxy-3a*S*,8a*R*-dihydroxy-1,3,3a,8a-tetrahydroindeno[1,2-*d*]imidazole-2,8-dione (**11a**)

**A.** Ninhydrin (81.0 mg, 0.459 mmol) was dissolved in the solution of *N*-benzyloxyurea (76.2 mg, 0.459 mmol) in acetic acid (4 mL) by stirring at 16 °C. The reaction solution

was maintained at 16 °C for 25 h, then acetic acid was evaporated under vacuum (3 mmHg). The obtained residue was washed with water (5 mL) at 5 °C and dried under vacuum (3 mmHg), giving 108.4 mg (72 %) *cis*-3a,8a-dihydroxydiastereomer **11a**, colourless crystals, m. p. 174-176 °C (with decomp.). <sup>1</sup>H NMR (300 MHz, DMSO-*d*<sub>6</sub>): δ = 4.745 (1H, d, *J* = 10.2 Hz, NOCH<sub>2</sub>), 4.896 (1H, d, *J* = 10.2 Hz, NOCH<sub>2</sub>), 6.850 (1H, s, OH), 7.298–7.386 (3H, m, Ph), 7.396–7.444 (2H, m, Ph), 7.566 (1H, s, OH), 7.634 (1H, t, *J* = 7.5 Hz, C<sub>6</sub>H<sub>4</sub>), 7.749–7.788 (2H, m, C<sub>6</sub>H<sub>4</sub>), 7.884 (1H, t, *J* = 7.5 Hz, C<sub>6</sub>H<sub>4</sub>), 8.719 (1H, s, NH). <sup>13</sup>C NMR (75 MHz, DMSO-*d*<sub>6</sub>): δ = 78.41 (NOCH<sub>2</sub>), 84.43 (C–OH), 89.17 (C–OH), 123.62 [C(H) C<sub>6</sub>H<sub>4</sub>], 124.84 [C(H) C<sub>6</sub>H<sub>4</sub>], 128.16 [C(H) Ph], 128.33 [C(4)H Ph], 129.01[C(H) Ph], 130.48 [C(H) C<sub>6</sub>H<sub>4</sub>], 131.95 [C<sub>q</sub> C<sub>6</sub>H<sub>4</sub>], 135.48 [C(1) Ph], 136.76 [C(H) C<sub>6</sub>H<sub>4</sub>], 150.72 [C<sub>q</sub> C<sub>6</sub>H<sub>4</sub>], 155.23 [N(C=O)N], 195.89 (C=O). MS (FAB) *m/z* 327 [M+H]<sup>+</sup>(9), 91 Bn<sup>+</sup> (100). Anal. Calc. for C<sub>17</sub>H<sub>14</sub>N<sub>2</sub>O<sub>5</sub>: C 62.58, H 4.32, N 8.58. Found: C 62.69, H 4.20, N 8.45.

**B.** Ninhydrin (50.1 mg, 0.281 mmol) was dissolved in the solution of *N*-benzyloxyurea (46.7 mg, 0.281 mmol) in acetic acid (3 mL) by stirring at 18 °C for 2 h. The reaction solution was maintained at 16 °C for 14 h, then acetic acid was evaporated under vacuum (3 mmHg). The obtained residue was washed by benzene (4 mL) and dried under vacuum (3 mmHg) to give 86.2 mg (94 %) of mixture of *cis*-3a,8a-dihydroxydiastereomer **11a** and *trans*-3a,8a-dihydroxydiastereomer **11b** (91:9). This mixture was dissolved in THF (2 mL) then hexane (5 mL) was added to it. After the maintaining at 4 °C for 72 h the obtained precipitate was filtered off, dried, extracted by water (3 mL) at 4 °C for 48 h. The resulting precipitate was filtered off and dried under vacuum (3 mmHg), giving 61 mg (66 %) of **11a**.

Crystals of compound **7** were grown from AcOH at 14 °C. The studied crystals are triclinic, C<sub>10</sub>H<sub>8</sub>N<sub>2</sub>O<sub>5</sub>, at 20 °C, *a* = 7.430(5) Å, *b* = 7.827(4) Å, *c* = 10.237(4) Å, *α* = 76.91(4)°, *β* = 77.88(5)°, *γ* = 66.53(6)°, *V* = 527.0(5) Å<sup>3</sup>, *M<sub>r</sub>* = 236.18, *Z* = 2, space group P1̄, *d<sub>calc.</sub>* = 1.488 g cm<sup>-3</sup>, *μ*(MoK<sub>α</sub>) = 0.122 mm<sup>-1</sup>, *F*(000) = 244.

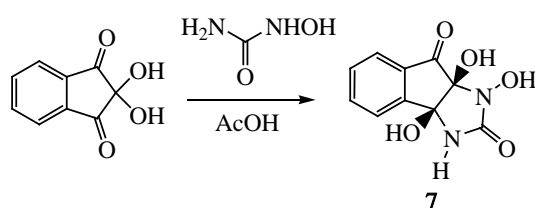
Crystals of compound **10a** were grown from THF-C<sub>6</sub>H<sub>14</sub> at -14 °C. The studied crystals are tetragonal, C<sub>14</sub>H<sub>16</sub>N<sub>2</sub>O<sub>5</sub>, at 20 °C, *a* = 22.2342(16) Å, *c* = 6.1638(10) Å, *V* = 3047.1(7) Å<sup>3</sup>, *M<sub>r</sub>* = 292.29, *Z* = 8, space group P4<sub>2</sub>/n, *d<sub>calc.</sub>* = 1.274 g cm<sup>-3</sup>, *μ*(MoK<sub>α</sub>) = 0.098 mm<sup>-1</sup>, *F*(000) = 1232. X-ray structural study of compounds **7** and **10a** was performed on an “Xcalibur 3” diffractometer (MoK<sub>α</sub>-radiation, graphite monochromator, Sapphire-3 CCD detector, ω-scanning, 2θ<sub>max</sub> = 50°).

The structure was solved by the direct methods with the SHELX-2016<sup>12</sup> software. The positions of the hydrogen atoms were located from electron density difference maps and refined by the “riding” model with *U<sub>iso</sub>* = *nU<sub>eq</sub>* of the carrier atoms (*n* = 1.5 for methyl and hydroxyl groups and *n* = 1.2 for other hydrogen atoms). Full-matrix least-squares refinement of the structures against *F*<sup>2</sup> in anisotropic approximation for non-hydrogen atoms was converged to *wR*<sub>2</sub> = 0.194 using 1846 reflections (*R*<sub>1</sub> = 0.078 for 699 reflections with *F* > 4σ(*F*), *S* = 0.903) for compound **7**, *wR*<sub>2</sub> = 0.201 using 2688 reflections (*R*<sub>1</sub> = 0.0695 for 1645 reflections with *F* > 4σ(*F*), *S* = 1.038) for compound **10a**. The

atomic coordinates, molecular geometry parameters, and crystallographic data of compound **7** and **10a** were deposited to the Cambridge Crystallographic Data Center, 12 Union Road, CB2, 1EZ UK [fax:+44-1223-336033, e-mail: deposit@ccdc.cam.ac.uk and is available on request quoting the deposit number CCDC 1976149 (**7**), 1971812 (**10a**).

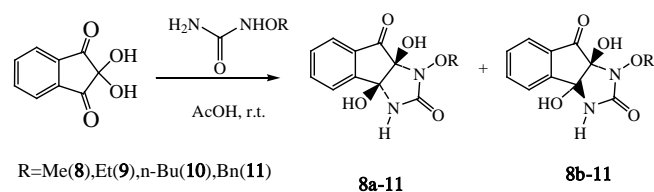
## RESULTS AND DISCUSSION

The ninhydrin interaction with *N*-hydroxyurea in acetic acid at 16–20 °C produces 1,3a,8a-trihydroxy-1,3,3a,8a-tetrahydroindeno[1,2-*d*]imidazole-2,8-dione (**7**) as single *cis*-3a(HO),8a(HO)-diastereomer with high yield (Scheme 4). The alternative *trans*-3a(HO),8a(HO)-diastereomer formation was not observed (Scheme 5).



**Scheme 5.** The synthesis of 1,3a,8a-trihydroxy-1,3,3a,8a-tetrahydroindeno[1,2-*d*]imidazole-2,8-dione **7**.

Ninhydrin reacts with *N*-alkoxyureas in the same conditions yielding mixtures of diastereomers of 1-alkoxy-3a,8a-dihydroxy-1,3,3a,8a-tetrahydroindeno[1,2-*d*]imidazole-2,8-diones **8–11** (Scheme 6).



**Scheme 6.** The synthesis of 1-alkoxy-3a,8a-dihydroxy-1,3,3a,8a-tetrahydroindeno[1,2-*d*]imidazole-2,8-diones **8–11**.

In these mixtures the diastereomers **8a–11a** with *cis* orientation of hydroxyl groups at C-3a, 8a carbon atoms dominate. Usually, the ratio **8a–11a/8b–11b** is 9:1–10:1. The diastereomers **8b–11b** with *trans* orientation of 3a-HO and 8a-HO-groups have been observed in the trace amounts of the reaction mixtures (<sup>1</sup>H NMR). The *cis*-3a,8a-dihydroxy diastereomers **8a–11a** can be easily obtained in pure form by the washing of the reaction mixture with water.

In the <sup>1</sup>H NMR spectra of compounds **7**, **8a–11a** the singlets of protons of *cis* 3a-HO and 8a-HO groups are situated in the different fields (6.64–6.85 ppm and 7.26–7.56 ppm) whereas the singlets of *trans* 3a-HO and 8a-HO moieties of diastereomers **8b–11b** are situated closely in the 6.99–7.17 ppm region (Table 1). The singlets of NH-protons of *cis*-3a,8a-dihydroxy diastereomers **8a–11a** are situated in the lower field than the same singlets of NH-protons of *trans*-3a,8a-dihydroxy diastereomers **8b–11b**.

**Table 1.** The typical <sup>1</sup>H NMR chemical shifts of 3a,8a-HO-protons and NH-protons of compounds **7**, **8a–11a** and **8b–11b**.

<i>cis</i> Diastereomer			<i>trans</i> Diastereomer		
Compd.	shifts, ppm		Compd.	shifts, ppm	
	OH	NH		OH	NH
<b>7</b>	6.646; 7.268	8.409	-	-	-
<b>8a</b>	6.792; 7.524	8.663	<b>8b</b>	7.047	8.534
<b>9a</b>	6.795; 7.488	8.650	<b>9b</b>	6.988; 7.042	8.514
<b>10a</b>	6.750; 7.390	8.609	<b>10b</b>	7.000; 7.070	8.507
<b>11a</b>	6.850; 7.566	8.719	<b>11b</b>	7.136; 7.176	8.595

In the <sup>13</sup>C NMR spectra of compounds **7**, **8a–11a** the chemical shifts of carbon atoms connected with HO-groups, NOCH<sub>2</sub> (NOME for compound **8a**) carbon atoms, and the carbon atoms of carbonyl groups are typical (Table 2).

**Table 2.** The typical <sup>13</sup>C NMR chemical shifts of carbon atoms of compounds **7**, **8a–11a**.

Compound	Shifts, ppm			
	C–OH	NOCH <sub>2</sub>	NC(=O)N	C=O
<b>7</b>	84.33; 89.36		156.05	195.63
<b>8a</b>	84.37; 88.92	64.36	155.19	196.14
<b>9a</b>	84.42; 89.14	71.73	155.55	196.07
<b>10a</b>	84.37; 89.08	76.03	155.40	195.96
<b>11a</b>	84.43; 89.17	78.41	155.23	195.89

Finally, the structure of compound **7** and **10a** have been proved by XRD study (Figures 1–3, Tables 3 and 4). The molecular structure of compound **7** is similar to the molecular structure of compound **10a**. The molecular structures of compounds **7** and **10a** contains *cis*-fused indane and imidazolidine moiety (Fig. 1, 2) with the angle between the indane and imidazolidine planes is 64° (**7**), 60° (**10a**). At that two hydroxyl groups are *cis*-oriented to each other (the O(2)–C(2)–C(3)–O(3) torsion angle in Table 3). However, some difference is revealed in the compensation of steric repulsion appeared due to *cis*-fusing. The C(3) atom deviates on 0.42 Å from the mean plain of remaining atoms of the heterocycle and on 0.24 Å from the mean plane of five-membered carbocycle in molecule **7**. In molecule **10a**, the N(2) atom deviates on 0.20 Å from the mean plain of remaining heterocyclic atoms while the carbocycle is planar. The endocyclic C(2)–C(3) bond which is joint for *cis*-fused cycles is elongated (Table 3) as compared to C(sp<sup>3</sup>)–C(sp<sup>3</sup>) ordinary bond (1.54 Å)<sup>13</sup> that is typical.<sup>14,15</sup>

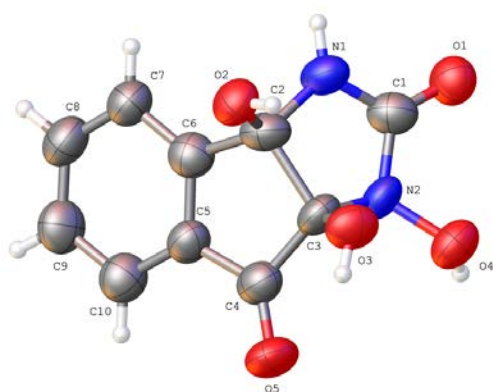


**Figure 1.** Molecular structure of 1,3a*S*,8a*R*-trihydroxy-1,3,3a,8a-tetrahydroindeno[1,2-*d*]imidazole-2,8-dione **7** with atoms represented by thermal vibration ellipsoids at 50 % probability level.

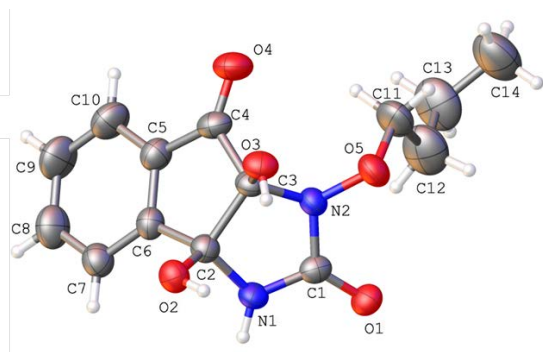


**Figure 2.** Molecular structure of 1-*n*-butyloxy-3a*S*,8a*R*-dihydroxy-1,3,3a,8a-tetrahydroindeno[1,2-*d*]imidazole-2,8-dione **10a** with atoms represented by thermal vibration ellipsoids at 50 % probability level.

**Table 3.** Some molecular characteristics in the **7** and **10a** crystals.

Bond	<b>7</b>	<b>10a</b>
O(2)–C(2)–C(3)–O(3), °	-21.8(7)	6.3(3)
C(2)–C(3), Å	1.619(7)	1.585(3)
C(3)–C(4), Å	1.575(8)	1.535(3)
C(2)–C(6), Å	1.557(8)	1.499(3)
O(2)–C(2), Å	1.439(6)	1.395(2)
O(3)–C(3), Å	1.411(6)	1.390(2)
N(1)–C(1), Å	1.369(7)	1.334(2)
N(2)–C(1), Å	1.409(7)	1.364(2)
C(4)=O(4), Å	1.206(3)	
C(1)=O(1), Å	1.242(2)	1.272 (6)
C(4)=O(5), Å		1.250(7)
∑N(1), °	360	360
∑N(2), °	341.9	348.5

The C(3)–C(4) bond in molecules **7**, **10a** is elongated (Table 3) compare to average length of C(sp<sup>3</sup>)–C(sp<sup>2</sup>) ordinary bond (1.510 Å).<sup>13</sup> In the molecule **7**, the endocyclic C(2)–C(6) bond is elongated compare to the same C(2)–C(6) bond in the molecule **10a** (Table 3) and average length of C(sp<sup>3</sup>)–C(sp<sup>2</sup>) ordinary bond.

The O(2)–C(2) and O(3)–C(3) ordinary bonds are similar in molecules **7** and **10a** (Table 3). In molecules **4a**, **5**, **6** the similar *cis* oriented vicinal (H)O–C bonds are so different.<sup>9,10</sup>

The N(1) atom has a planar configuration while the N(2) atom has a pyramidal configuration (Table 3) in the both molecules. At that the N(1)–C(1) amide bond is shorter than N(2)–C(1) amide bond (Table 3) indicating stronger conjugation between N(1) lone pair and C(1)=O(1) carbonyl bond as compared to conjugation between N(2) lone pair and C(1)=O(1) carbonyl bond in both molecules. The similar phenomenon is typical for 3-hydroxy- and 3-alkoxy-5-arylimidazolidine-2,4-diones,<sup>6,8</sup> *N*-methoxyurea<sup>11</sup> and in the cyclic *N*-alkoxyureas **5,6**.<sup>10</sup>

The N(2)–O(4)H bond [1.429(5) Å] in molecule **7** is longer than N(2)–O(5)Bu bond [1.397(2) Å] in molecule **10a**, and N–OH bond [1.398(7) Å] in molecule **4a**,<sup>9</sup> N–OH bond [1.3745(17) Å] in 3-hydroxy-5-phenylimidazolidine-2,4-dione.<sup>6</sup>

In molecule **10a** the butyloxy moiety has +*ac*-conformation to the C(1)–N(2) endocyclic bond [the C(1)–N(2)–O(5)–C(11) torsion angle is 115.1(2)°] and the butyl fragment is turned relatively to the N(2)–O(5) bond [the N(2)–O(5)–C(11)–C(12) torsion angle is -75.6(2)°]. The C(13) and C(14) atoms are disordered on two position **A** and **B** with the population ratio of 60:40 due to the rotation around the C(11)–C(12) bond. The O(5)–C(11)–C(12)–C(13) torsion angle is -175.7(2)° in conformer **A** and 167.7(2)° in conformer **B** while the C(11)–C(12)–C(13)–C(14) torsion angle is -168.3(2)° in conformer **A** and 68.7(2)° in conformer **B**. In the both molecules **7** and **10a** the ketone carbonyl bond is shorter as compared to urea carbonyl bond.

In the crystal phase, molecules **7** and **10a** form the centrosymmetrical dimers bound by the O(4)–H(4)...O(1) (**7**), O(2)–H(2)...O(1) and O(3)–H(3)...O(1) (**10a**) intermolecular hydrogen bonds (Table 3, Figure 3). These dimers form the chains along [1 0 0] crystallographic direction due to the intermolecular hydrogen bond N(1)–H(1)...O(5) in the **7** crystal and along [001] crystallographic direction due to the N(1)–H(1)...O(3) intermolecular hydrogen bond in the **10a** crystal (Table 3, Figure 3). The neighboring chains link by the O(3)–H(3)...O(4) and O(2)–H(2)...O(1) intermolecular hydrogen bonds in the **10a** crystal (Table 4).

**Table 4.** Intermolecular hydrogen bonds in the **7** and **10a** crystals.

Crystal	Hydrogen bond	Symmetry operations	H...A, Å	D–H...A, deg.
<b>7</b>	O(4)–H(4)...	1-x, 2-y,	1.94	160
	H(4)...O(1)	2-z		
	N(1)–H(1)...	-1+x, y,	2.21	156
	H(1)...O(5)	z		
	O(3)–H(3)...	2-x, 1-y,	2.20	139
	H(3)...O(4)	2-z		
	O(2)–H(2)...	1-x, 1-y,	2.11	161
	H(2)...O(1)	2-z		
	O(2)–H(2)...	1-x, 1-y,	2.01	156
	H(2)...O(1)	1-z		
<b>10a</b>	O(3)–H(3)...	1-x, 1-y,	1.92	165
	H(3)...O(1)	1-z		
	N(1)–H(1)...	x, y,	2.07	173
	H(1)...O(3)	-1+z		

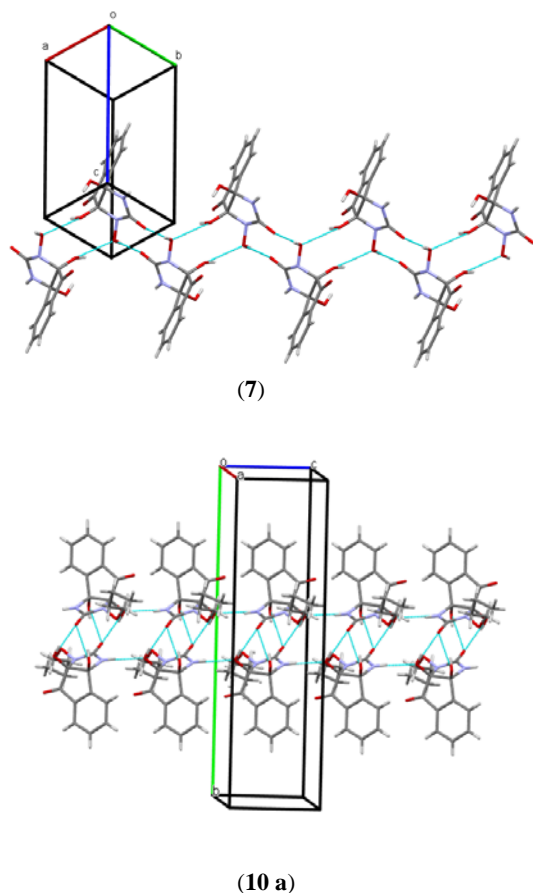
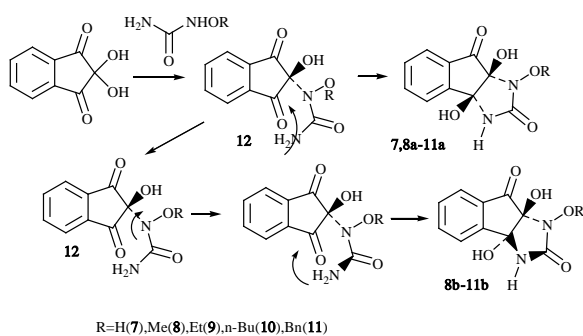


**Figure 3.** The arrangement of the molecules in compound **7**, **10a** in the crystal.



**Scheme 7.** The proposed formation mechanism of the compounds **7–11**.

The formation of tricyclic compounds **7–11** may be realized in the following way (Scheme 7). At the first stage the ninhydrin's interaction with *N*-hydroxyurea or *N*-alkoxyureas on *N*-hydroxyamino group or *N*-alkoxyamino group takes place, forming ureas **12**. In the same manner the arylglyoxals react with *N*-hydroxyurea,<sup>6–8</sup> *N*-alkoxyureas,<sup>9</sup> *N*-alkoxy-*N'*-arylureas<sup>10</sup> and *N*-alkoxy-*N'*-alkylureas.<sup>10</sup>

On the second stage compounds **7** and **8a–11a** are formed due to the intramolecular cyclization. In these heterocycles the vicinal HO-groups of hemiaminal moieties have *cis* mutual orientation.

In the ureas **12** the rotation around N–C bond with further cyclization gives diastereomers **8b–11b** having *trans* mutual orientation of the vicinal HO-groups. Probably, this rotation is retarded and proceeds more slowly than the cyclization yielding *cis*-3a,8a-dihydroxydiastereomers **7** and **8a–11a**.

## CONCLUSIONS

We have found that ninhydrin reacts with *N*-hydroxyurea and *N*-alkoxyureas in acetic acid with the predominant formation of the diastereomers of the 1,3a,8a-trihydroxy-1,3,3a,8a-tetrahydroindeno[1,2-*d*]imidazole-2,8-dione and 1-alkoxy-3a,8a-dihydroxy-1,3,3a,8a-tetrahydroindeno[1,2-*d*]imidazole-2,8-diones having the *cis*-orientation of 3a,8a-HO-groups. The structures of 1,3a,8aR-trihydroxy-1,3,3a,8a-tetrahydroindeno[1,2-*d*]imidazole-2,8-dione **7** and 1-*n*-butyloxy-3a,8aR-dihydroxy-1,3,3a,8a-tetrahydroindeno[1,2-*d*]imidazole-2,8-dione **10a** have been investigated by XRD study.

## REFERENCES

- Shapiro, R., Chatterjee, N., Cyclization Reactions of Ninhydrin with Aromatic Amines and Ureas, *J. Org. Chem.*, **1970**, 35(2), 447–450. <https://doi.org/10.1021/jo00827a034>
- Van Slyke, D. D., Hamilton, P. B., The Synthesis and Properties of Ninhydrin Ureide. *J. Biol. Chem.*, **1943**, 150(2), 471–476.
- Azizian, J., Karimi, A. R., Soleimani, E., Mohammadi, A.A., Mohammadzadeh, M. R., Highly Functionalized Dihydrofuran Derivatives: Synthesis by Diastereoselective Intramolecular Wittig Reaction, *Heteroatom. Chem.*, **2006**, 17(4), 277–279. DOI: 10/1002hc
- Jong, J. A. W., Moret, M.-E., Verhaar, M. C., Hennink, W. E., Gerritsen, K. G. F., Van Nostrum, C. F., Effect of Substituents on the Reactivity of Ninhydrin with Urea, *ChemistrySelect*, **2018**, 3, 1224–1229. DOI: 10/1002slct201800040.
- Jong, J. A. W., Smakman, R., Moret, M.-E., Verhaar, M. C., Hennink, W. E., Gerritsen, K. G. F., Van Nostrum, C. F., Reactivity of (Vicinal) Carbonyl Compounds with Urea, *ACS Omega*, **2019**, 4, 11928–11937. DOI: 10/10021acsomega.9b01177
- Shtamburg, V. G., Anishchenko, A. A., Shtamburg, V. V., Shishkin, O. V., Zubatyuk, R. I., Mazepa, A. V., Rakipov, I. M., Kostyanovsky, R. G., Synthesis and crystal structure of new imidazolidine-2,4-dione and imidazolidin-2-one derivatives, *Mendeleev Commun.*, **2008**, 18, 102–104. DOI: 10.1016/j.mencom.2008.03.018.
- Kostyanovsky, R. G., Shtamburg, V. G., Shishkin, O. V., Zubatyuk R. I., Shtamburg, V. V., Anishchenko, A. A., Mazepa, A. V., Pyramidal nitrogen in the crystal of *N*-[(benzoyl)-(hydroxy)methyl]-*N*-benzyloxy-*N'*-(2-bromophenyl)urea. *Mendeleev Commun.*, **2010**, 20, 167–169. DOI: 10.1016/j.mencom.2010.05.015.
- Shtamburg, V. G., Shtamburg, V. V., Anishchenko, A. A., Zubatyuk R. I., Mazepa, A. V., Klotz, E. A., Kravchenko, S. V., Kostyanovsky, R. G., Single-stage synthesis of 3-hydroxy- and 3-alkoxy-5-arylimidazolidine-2,4-diones by reaction of arylglyoxal hydrates with *N*-hydroxy- and *N*-alkoxyureas, *Chem. Heterocycl. Comp.*, **2015**, 51(6), 553–559, DOI 10.1007/s10593-015-1735-0
- Shtamburg, V. G., Shtamburg, V. V., Anishchenko, A. A., Mazepa, Shishkina, S. V., Konovalova, I. S., Synthesis and structure of 3,4,5-trihydroxy-5-(4-nitrophenyl)imidazolidin-2-one, *Eur. Chem. Bull.*, **2019**, 8(4), 110–114. DOI: 10.17628/ecb.2019.8.110-114.

- <sup>10</sup>Shtamburg, V. G., Shtamburg, V. V., Anishchenko, A. A., Shishkina, S. V., Mazepa, A. V., Konovalova, I. S., 3-Alkoxy-1,5-diaryl-4,5-dihydroxyimidazolidin-2-ones and 3-Alkoxy-1-alkyl-5-aryl-4,5-dihydroxyimidazolidin-2-ones: Synthesis and Structure, *Eur. Chem. Bull.*, **2019**, 8(9), 282–290. DOI: <http://dx.doi.org/10.17628/ecb.2019.8.282-290>
- <sup>11</sup>Shtamburg, V. G., Klots, E. A., Pleshkova, A. P., Avramenko, V. I., Ivonin, S. P., Tsygankov, A. V., Kostyanovsky, R. G., Geminal systems. 50. Synthesis and alcoholysis on *N*-acyloxy-*N*-alkoxy derivatives of ureas, carbamates and benzamide, *Russ. Chem. Bull., Int. Ed.*, **2003**, 52(10), 2251–2260. <https://doi.org/10.1023/B:RUCB.0000011887.405.29.b0>
- <sup>12</sup>Sheldrick, G. M., SHELXT – integrated space-group and crystal-structure determination, *Acta Crystallogr., Sect. A: Found. Crystallogr.*, **2015**, A71(1), 3–8. <https://doi.org/10.1007/S2053273314026370>
- <sup>13</sup>Burgi, H.-B., Dunitz, J. D., *Structure correlation*. Vol. 2. VCH. Weinheim, 1994, 741–784. <https://doi.org/10.1107/S0108768195009931>
- <sup>14</sup>Agapiou, K., Cauble, D. F., Krische, M. J., Copper-Catalyzed Tandem Conjugate Addition–Electrophilic Trapping: Ketones, Esters, and Nitriles as Terminal Electrophiles, *J. Am. Chem. Soc.*, **2004**, 126(14), 4528–4529. DOI: 10.1021/ja030603l.
- <sup>15</sup>Deng, Q.-H., Wadepohl, H., Gade, L. H., Highly Enantioselective Copper-Catalyzed Alkylation of  $\beta$ -Ketoesters and Subsequent Cyclization to Spirolactones/Bi-spirolactones, *J. Am. Chem. Soc.*, **2012**, 134(6), 2946–2949. DOI: 10.1021/ja211859w.

Received: 19.01.2020.

Accepted: 19.04.2020.



# SYNTHESIS AND ANTI-PROLIFERATIVE SCREENING OF NEW THIAZOLE COMPOUNDS

J. P. Sonar,<sup>[a]</sup> S. D. Pardeshi,<sup>[a]</sup> S. A. Dokhe,<sup>[a]</sup> K. R. Kharat,<sup>[b]</sup> A. M. Zine,<sup>[a]</sup>  
László Kótai,<sup>[c]</sup> R. P. Pawar,<sup>[d]\*</sup> S. N. Thore<sup>[d]\*</sup>

**Keywords:** Synthesis, anti-proliferative, thiazole, oxadiazole, pyrazole.

A new series of thiazole compounds are synthesized and their anticancer activity was tested against breast cancer cells MCF7. The starting ethyl 2-(4-hydroxyphenyl)-4-methylthiazole-5-carboxylate was alkylated by alkyl bromides in DMF. The resulted ethyl 4-methyl-2-(4-(alkyloxy)phenyl)thiazole-5-carboxylate compounds were refluxed with hydrazine hydrate in ethanol to afford 4-methyl-2-(4-(alkyloxy)phenyl)thiazole-5-carbohydrazide compounds. These hydrazides were reacted with various cyclizing reagents to give various 1,3,4-oxadiazole and pyrazole-ring containing thiazole compounds. The antiproliferative activity was calculated on the basis of IC<sub>50</sub> values. The (5-amino-3-phenyl-1H-pyrazol-1-yl)(4-methyl-2-(4-(ethoxy)phenyl)thiazol-5-yl)methanone has comparable activity with standard Paclitaxel.

\* Corresponding Authors

E-Mail: [snthore@rediffmail.com](mailto:snthore@rediffmail.com), [rppawar@yahoo.com](mailto:rppawar@yahoo.com)

- [a] Department of Chemistry, Vinayakrao Patil Mahavidyalaya, Vaijapur, Aurangabad-423701, Maharashtra, India  
 [b] Department of Biotechnology, Deogiri College, Station Road, Aurangabad- 431 005, Maharashtra, India.  
 [c] Research Centre for Natural Sciences, Budapest, Hungary  
 [d] Department of Chemistry, Deogiri College, Station Road, Aurangabad- 431 005, Maharashtra, India.

## INTRODUCTION

Heterocycles including 1,3,4-oxadiazoles and pyrazoles have always attracted the attention of researchers as they showed various biological activities. The 1,3,4-oxadiazole is a key core used against various fungi<sup>1</sup> and bacteria-caused diseases.<sup>2</sup> It also reported to possess anti-viral,<sup>3</sup> anti-inflammatory,<sup>4,5</sup> anti-cancer<sup>6,7</sup> and central nervous system depressant<sup>8</sup> activities. Some important drugs like Raltegravir and Furamizole contain 1,3,4-oxadiazole cores<sup>9</sup> (Fig. 1).

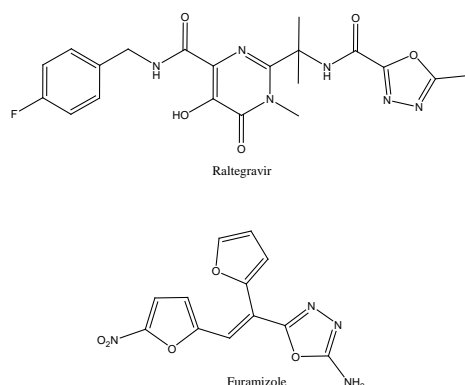


**Figure 1.** Important drugs containing 1,3,4-oxadiazole

Pyrazoles are the important core of organic synthesis abundantly found in the naturally occurring compounds.<sup>10</sup> It is found in agrochemical products as herbicides, insecticides, fungicides, etc. In medicines was found to have a variety of activities; such as anti-inflammatory, anti-cancer, anti-

convulsant, antifungal, antidiabetic, antiviral and anti-bacterial activities.<sup>11-14</sup> Some of them are depicted as bellow<sup>12</sup> (Fig. 2).

On observing these various biological properties associated with five-membered heterocycles, inspired us for the synthesis of 5-substituted 4-methyl-2-(4-(alkyloxy)phenyl)thiazole.

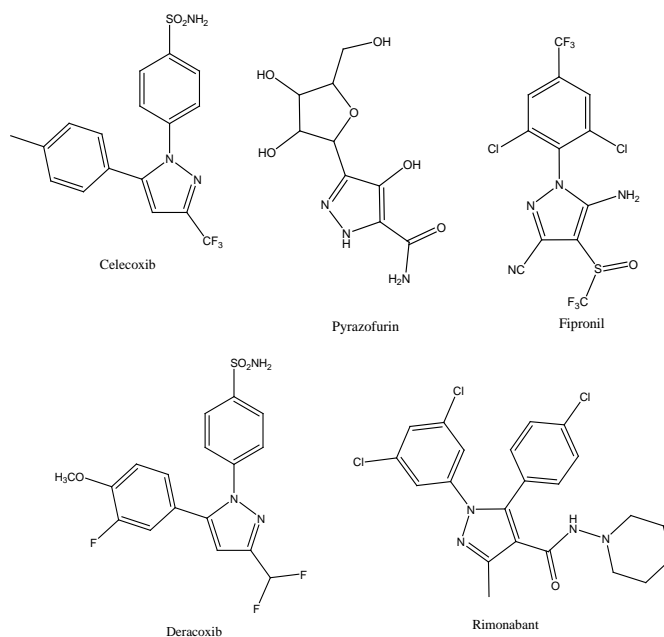
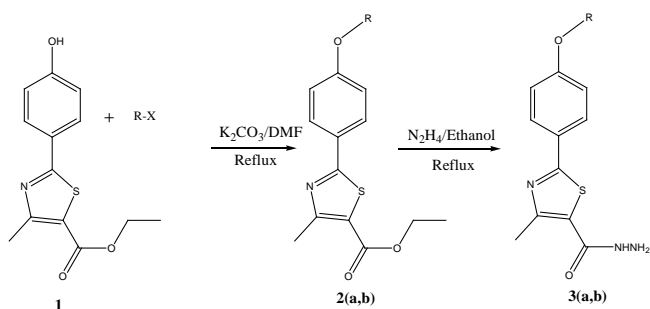


**Figure 2.** Important drugs containing pyrazole

## RESULTS AND DISCUSSION

The parent ethyl 2-(4-hydroxyphenyl)-4-methylthiazole-5-carboxylate (**1**) was synthesized by the reaction of 4-hydroxy benzothioamide with ethyl-2-chloroacetate in ethanol. Then, the obtained compound **1** was purified by flash chromatography with n-hexane: ethyl acetate (1:1)

system. The compound **1** was then treated with n-pentyl bromide or ethyl iodide in presence of tetrabutyl ammonium iodide (TBAI), catalytic amount of KI, potassium carbonate and DMF as solvent at reflux condition to give compound ethyl 4-methyl-2-(4-(alkyloxy)phenyl)thiazole-5-carboxylates (**2a**, **2b**). Compound **2a** and **2b** were treated with hydrazine hydrate to give 4-methyl-2-(4-(alkyloxy)phenyl)thiazole-5-carbohydrazides (**3a**, **3b**). Compound **3a** and **3b** were reacted with difference cyclizing reagents to give different azole scaffolds.

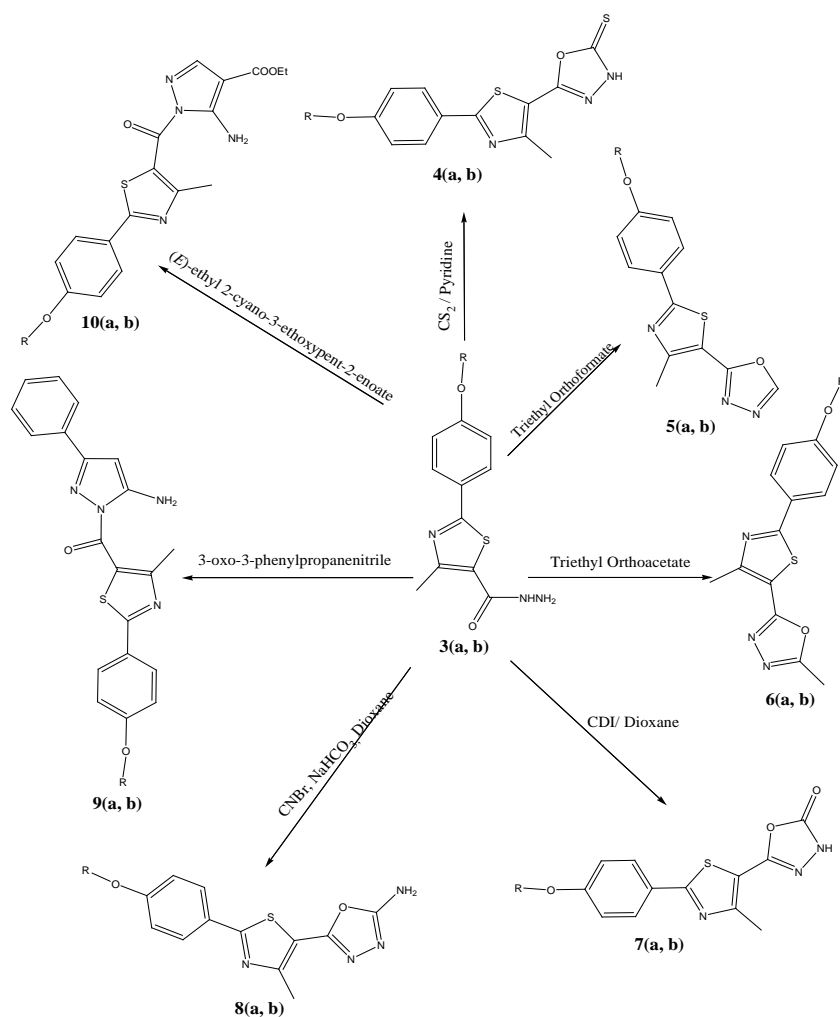


**Scheme 1.** Synthesis of hydrazide derivatives 3(a,b)

The key intermediate **3a** was treated with carbon disulphide and pyridine to afford 5-(4-methyl-2-(4-(pentyloxy)phenyl)thiazol-5-yl)-1,3,4-oxadiazole-2(3H)-thione (**4a**).

The hydrazide **3a** was treated with triethyl orthoformate and triethylorthoacetate to give 2-(4-methyl-2-(4-(pentyloxy)phenyl)thiazol-5-yl)-1,3,4-oxadiazole (**5a**) and 2-methyl-5-(4-methyl-2-(4-(pentyloxy)phenyl)thiazol-5-yl)-1,3,4-oxadiazole (**6a**) respectively. The hydrazide **3a** on treatment with CDI in dioxane gave 5-(4-methyl-2-(4-(pentyloxy)phenyl)thiazol-5-yl)-1,3,4-oxadiazol-2(3H)-one (**7a**).

The intermediate **3a** on treatment with cyanogen bromide and sodium hydrogen carbonate gave 5-(4-methyl-2-(4-(pentyloxy)phenyl)thiazol-5-yl)-1,3,4-oxadiazol-2-amine (**8a**). The same compound was reacted with 3-oxo-3-phenylpropanenitrile and yielded (5-amino-3-phenyl-1H-pyrazol-1-yl)(4-methyl-2-(4-(pentyloxy)phenyl)thiazol-5-yl)methanone (**9a**). The compound **3a** was treated with (*E*)-ethyl 2-cyano-3-ethoxypent-2-enoate and gave (ethyl-5-amino-1H-pyrazol-1-yl-4-carboxylate)(4-methyl-2-(4-(pentyloxy)phenyl)thiazol-5-yl)methanone 10(a).



Where compounds (a) R = Penty and (b) R = Ethyl group

**Scheme 2.** Synthesis of various heterocycles **4(a,b)** to **10(a,b)** from hydrazide **3(a,b)**

In a similar way, hydrazide **3b** was treated with various cyclizing agents to obtain compounds **4b-10b** and screened for anti-proliferative activity against breast cancer cells MCF7.

**Table 1.** Evaluation of IC<sub>50</sub> values of 4-methyl-2-(4-(alkyloxy)phenyl)thiazole derivatives

Sr. No.	Compound	IC <sub>50</sub> Value (μM)
1	<b>4a</b>	26.21
2	<b>5a</b>	15.16
3	<b>6a</b>	12.65
4	<b>7a</b>	15.82
5	<b>8a</b>	59.12
6	<b>9a</b>	NA
7	<b>10a</b>	NA
8	<b>4b</b>	NA
9	<b>5b</b>	NA
10	<b>6b</b>	NA
11	<b>7b</b>	14.81
12	<b>8b</b>	93.94
13	<b>9b</b>	5.87
14	<b>10b</b>	NA
15	Paclitaxel (standard drug)	4.8

The breast cancer cells MCF7 were treated with compounds and the anti-proliferative effect was evaluated by MTT assay.

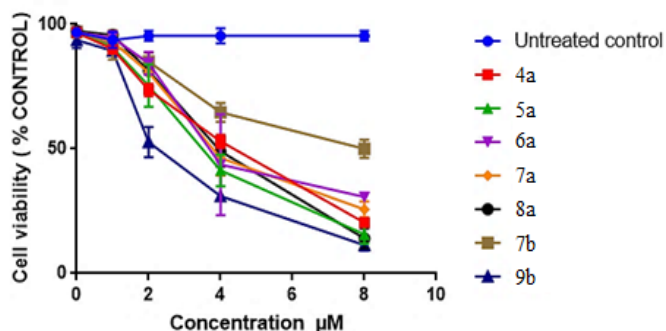


**Figure 3.** Dose-dependent study of cell viability

As shown in (Fig. 3), a dose-dependent decrease in the growth of cancer cells was observed with increasing concentration of the compounds. Compounds **4a**, **5a**, **6a**, **7a**, **8a** and **7b** showed less to moderate anti-proliferative activity while compound **9b** was found to show comparable activity (IC<sub>50</sub>) to standard anticancer drug Paclitaxel. Among the cells, the IC<sub>50</sub> value of **6a** and **9b** in MCF7 were found to be low i.e. 12.65 ± 0.5 and 5.87 ± 1 μM, respectively. This suggested that treatment with compounds inhibited the growth and induced apoptosis in these cells.

Significantly decreased cell viability was found in compounds treated T-47D cells ( $p < 0.0001$  compared to untreated control).

## EXPERIMENTALS

All the melting points were recorded by open capillary method and are uncorrected. IR spectra were recorded on Shimadzu IR Affinity 1 spectrophotometer in KBr disc. <sup>1</sup>H NMR were recorded on a BRUKER AVANCE II 400MHz spectrometer in CDCl<sub>3</sub>/ DMSO d<sub>6</sub>, chemical shifts are in ppm relative to TMS. Mass spectra were taken on a Macro mass spectrometer by electron spray method (Es). The structures of various synthesized compounds were assigned on the basis of spectral studies and it has been reported in experimental protocols. The progress of reaction was monitored on Alumina coated TLC plates in ethyl acetate and n-hexane system.

The anti-cancer effect of compounds on the breast cancer cells MCF7 was evaluated by MTT Assay Kit (Thermo Inc. USA). The cells were plated at ~ 1 × 10<sup>3</sup> cells in 96 well plates containing 100 μL of DMEM and 0,1,2,4,8 μM compounds were added to each well. In three different wells same concentration was used. Cell death was analysed after 24 hours at 37°C. <sup>15</sup> MTT reagent (5 mg/mL) was added and kept for four hours incubation. The procedure was followed according to the manufacturer's instructions. The absorbance was recorded at 490 nm using a 96 well Multiscan Ascent (Thermo Inc. USA). The inhibitory effect of compounds on cell growth was assessed as percent cell viability, where cells without treatment were considered 100% viable. The statistical differences were evaluated by Students two-tailed t-test.

### Synthesis of ethyl 4-methyl-2-(4-(alkyloxy)phenyl)thiazole-5-carboxylates (**13a** and **13b**)

Compound **1** (2.63 g, 0.01 mol) was mixed with powdered potassium carbonate (2.07 gm, 0.015 mol) and DMF (25 mL). To this reaction mixture n-pentyl bromide or ethyl iodide (0.011 mol) with catalytic amount of TBAI and KI were added. The mixture was allowed to reflux for 8 h. The resulting mixture was cooled and poured onto 100 g of ice. The precipitate obtained was filtered, dried at room temperature and purified by column chromatography using hexane: ethyl acetate system (9:1).

**2a:** Yield: 2.1 g (63 %); mp: 47-48 °C; IR (KBr, cm<sup>-1</sup>): 2950, 1700, 1608, 1516, 1441, 1370, 1253, 1174, 1091; <sup>1</sup>H NMR (DMSO-d<sub>6</sub>): 0.96 (t, 3H, -CH<sub>3</sub>), 1.33 (t, 3H, CH<sub>3</sub>), 1.36-1.45 (m, 4H, 2CH<sub>2</sub>), 1.75 (quintate, 2H, CH<sub>2</sub>), 2.67 (s, 3H, Ar-CH<sub>3</sub>), 4.02 (t, 2H, O-CH<sub>2</sub>), 4.29 (t, 2H, O-CH<sub>2</sub>), 7.87 (d, 2H, *J* = 8 Hz, 2Ar-H), 7.89 (d, 2H, *J* = 8 Hz, 2Ar-H); M.W. = 333; Mass: (M+1) = 334.

**2b:** Yield: 1.8 gm (61 %); mp: 98-99 °C; IR (KBr, cm<sup>-1</sup>): 2984, 1695, 1602, 1522, 1446, 1394, 1370, 1322, 1253, 1181, 1121, 1045; <sup>1</sup>H NMR (DMSO-d<sub>6</sub>): 1.32 (t, 3H, -CH<sub>3</sub>), 1.37 (t, 3H, CH<sub>3</sub>), 2.66 (s, 3H, Ar-CH<sub>3</sub>), 4.10 (q, 2H, O-CH<sub>2</sub>), 4.28 (q, 2H, O-CH<sub>2</sub>), 7.01 (d, 2H, *J* = 8 Hz, 2Ar-H), 7.87 (d, 2H, *J* = 8 Hz, 2Ar-H); M.W. = 291; (M+1) = 292.

**Synthesis of 4-methyl-2-(4-(alkyloxy)phenyl)thiazole-5-carbohydrazide (3a and 3b)**

Compound **3a** or **3b** (0.006 mol) was dissolved in 15 mL of ethanol. To this mixture hydrazine hydrate (99 %) (0.5 mL, 0.009 mol) was added and refluxed for 3 hours. After the completion of reaction, the reaction mixture was cooled and poured over 50 gms of crushed ice and filtered off. The crude product was recrystallized using ethanol to afford fine yellow colored needle shaped crystals.

**3a:** Yield: 1.8 g (94 %); mp: 144-145 °C; IR: (KBr,  $\text{cm}^{-1}$ ): 3300, 3200, 2941, 1620, 1524, 1474, 1258, 1178;  $^1\text{H NMR}$  ( $\text{DMSO-d}_6$ ): 0.91 (t, 3H,  $-\text{CH}_3$ ), 1.33-1.44 (m, 4H,  $2\text{CH}_2$ ), 1.75 (quintate, 2H,  $\text{CH}_2$ ), 2.58 (s, 3H, Ar- $\text{CH}_3$ ), 4.02 (t, 2H, O- $\text{CH}_2$ ), 4.49 (s, 2H, NH $_2$ ), 7.01 (d, 2H,  $J=8\text{ Hz}$ , 2Ar-H), 7.83 (d, 2H,  $J=8\text{ Hz}$ , 2Ar-H), 9.48 (s, 1H, NH); M.W.= 319; (M+1) = 320.

**3b:** Yield: 1.6 g (96 %); mp: 161-162 °C; IR (KBr,  $\text{cm}^{-1}$ ): 3304, 2984, 1630, 1610, 1522, 1450, 1370, 1322, 1265, 1173, 1117, 1049;  $^1\text{H NMR}$  ( $\text{DMSO-d}_6$ ): 1.38 (t, 3H,  $-\text{CH}_3$ ), 2.59 (s, 3H, Ar- $\text{CH}_3$ ), 4.08 (q, 2H, O- $\text{CH}_2$ ), 4.46 (s, 2H, NH $_2$ ), 7.00 (d, 2H,  $J=8\text{ Hz}$ , 2Ar-H), 7.83 (d, 2H,  $J=8\text{ Hz}$ , 2Ar-H), 9.46 (s, 1H, NH); M.W.= 277; (M+1) = 278.

**5-(4-Methyl-2-(4-(alkyloxy)phenyl)thiazol-5-yl)-1,3,4-oxadiazole-2(3H)-thione (4a and 4b)**

A mixture of **3a** or **3b** (0.002 mole) and carbon disulfide (3 mL) in pyridine (10 mL) was refluxed for 6 h. After completion of the reaction, the solvent was removed using rotary evaporator and the residue obtained was triturated with ice-water mixture and neutralized using dilute HCl. The separated solid was filtered, washed and dried and recrystallized using ethanol to give **4a** as pale yellow crystals.

**4a:** Yield: 0.580 g (80 %); mp: 186-187 °C; IR: (KBr,  $\text{cm}^{-1}$ ): 3075, 2925, 1603, 1516, 1441, 1383, 1303, 1262, 1178;  $^1\text{H NMR}$  ( $\text{DMSO-d}_6$ ): 0.89 (t, 3H,  $-\text{CH}_3$ ), 1.31-1.42 (m, 4H,  $2\text{CH}_2$ ), 1.71 (quintate, 2H,  $\text{CH}_2$ ), 2.65 (s, 3H, Ar- $\text{CH}_3$ ), 4.00 (t, 2H, O- $\text{CH}_2$ ), 7.02 (d, 2H,  $J=8\text{ Hz}$ , 2Ar-H), 7.88 (d, 2H,  $J=8\text{ Hz}$ , 2Ar-H); M.W.= 361, (M+1) = 362.

**4b:** Yield: 0.560 g (87 %); mp: 231-232 °C; IR (KBr,  $\text{cm}^{-1}$ ): 3088, 2935, 2752, 1602, 1510, 1442, 1382, 1305, 1261, 1173, 1081, 1045;  $^1\text{H NMR}$  ( $\text{DMSO-d}_6$ ): 1.36 (t, 3H,  $-\text{CH}_3$ ), 2.66 (s, 3H, Ar- $\text{CH}_3$ ), 4.12 (q, 2H, O- $\text{CH}_2$ ), 7.07 (d, 2H,  $J=8\text{ Hz}$ , 2Ar-H), 7.94 (d, 2H,  $J=8\text{ Hz}$ , 2Ar-H), 9.29 (s, 1H, Ar-H); M.W.= 319; (M+1) = 320.

**2-(4-Methyl-2-(4-(alkyloxy)phenyl)thiazol-5-yl)-1,3,4-oxadiazole (5a, 5b)**

Compound **3a** or **3b** (0.002 mol) was refluxed in triethyl orthoformate (10 mL) for 14 h. The extra solvent was removed under vacuum. Thus, the solid obtained was recrystallized by ethanol to afford yellowish crystals.

**5a:** Yield: 0.473 gm (72 %); mp: 81 °C; IR: (KBr,  $\text{cm}^{-1}$ ): 3133, 2958, 1603, 1516, 1449, 1379, 1316, 1258, 1174, 1091;  $^1\text{H NMR}$  ( $\text{DMSO-d}_6$ ): 0.91 (t, 3H,  $-\text{CH}_3$ ), 1.35-1.39

(m, 4H,  $2\text{CH}_2$ ), 1.73-1.76 (quintate, 2H,  $\text{CH}_2$ ), 2.75 (s, 3H, Ar- $\text{CH}_3$ ), 4.06 (t, 2H, O- $\text{CH}_2$ ), 7.08 (d, 2H,  $J=8\text{ Hz}$ , 2Ar-H), 7.96 (d, 2H,  $J=8\text{ Hz}$ , 2Ar-H), 9.37 (s, 1H, Ar-H); M.W.= 329; (M+1) = 330.

**5b:** Yield: 0.43 g (75 %); mp: 145-146 °C; IR (KBr,  $\text{cm}^{-1}$ ): 3119, 2984, 1606, 1519, 1437, 1378, 1270, 1305, 1265, 1177, 1045;  $^1\text{H NMR}$  ( $\text{DMSO-d}_6$ ): 1.38 (t, 3H,  $-\text{CH}_3$ ), 2.75 (s, 3H, Ar- $\text{CH}_3$ ), 4.11 (q, 2H, O- $\text{CH}_2$ ), 7.02 (d, 2H,  $J=8\text{ Hz}$ , 2Ar-H), 7.92 (d, 2H,  $J=8\text{ Hz}$ , 2Ar-H), 9.29 (s, 1H, Ar-H); M.W.= 287; (M+1) = 288.

**2-Methyl-5-(4-methyl-2-(4-(alkyloxy)phenyl)thiazol-5-yl)-1,3,4-oxadiazole (6a, 6b):**

Compound **6a** and **6b** were prepared by refluxing **3a** or **3b** (0.002 mol) in triethyl orthoacetate (10 mL) for 16 h. After the completion of reaction the extra solvent was removed under reduced pressure. The solid obtained was recrystallized by using ethanol to give yellow coloured crystals.

**6a:** Yield: 0.510 g (74 %); mp: 83-84 °C; IR: (KBr,  $\text{cm}^{-1}$ ): 2958, 1603, 1574, 1445, 1420, 1399, 1303, 1258, 1178, 1020;  $^1\text{H NMR}$  ( $\text{DMSO-d}_6$ ,  $\delta$  ppm): 0.92 (t, 3H,  $-\text{CH}_3$ ), 1.40 (m, 4H,  $2\text{CH}_2$ ), 1.75 (quintate, 2H,  $\text{CH}_2$ ), 2.54 (s, 3H, Ar- $\text{CH}_3$ ), 2.73 (s, 3H, Ar- $\text{CH}_3$ ), 4.02 (t, 2H, O- $\text{CH}_2$ ), 6.98 (d, 2H,  $J=8\text{ Hz}$ , 2Ar-H), 7.86 (d, 2H,  $J=8\text{ Hz}$ , 2Ar-H); M.W.= 343, (M+1) = 344.

**6b:** Yield: 0.457 gm (76 %); mp: 147-148 °C; IR (KBr,  $\text{cm}^{-1}$ ): 2991, 1596, 1571, 1474, 1441, 1375, 1312, 1258, 1170, 1120, 1041;  $^1\text{H NMR}$  ( $\text{DMSO-d}_6$ ,  $\delta$  ppm): 1.38 (t, 3H,  $-\text{CH}_3$ ), 2.52 (s, 3H, Ar- $\text{CH}_3$ ), 2.73 (s, 3H, Ar- $\text{CH}_3$ ), 4.11 (q, 2H, O- $\text{CH}_2$ ), 7.04 (d, 2H,  $J=8\text{ Hz}$ , 2Ar-H), 7.91 (d, 2H,  $J=8\text{ Hz}$ , 2Ar-H); M.W.= 301; (M+1) = 302.

**5-(4-Methyl-2-(4-(alkyloxy)phenyl)thiazol-5-yl)-1,3,4-oxadiazol-2(3H)-one (7a, 7b)**

The mixture of **3a** or **3b** (0.002 mol) and  $\text{N,N}'$ -carbonyl diimidazole (CDI) (0.486 gm, 0.003 mol) in dioxane (20 mL) was refluxed for 6 hours. After completion of reaction the mixture was allowed to cool and solvent was removed under reduced pressure. The solid obtained was recrystallized from ethanol to give colorless crystals.

**7a:** Yield: 0.552 g (80 %); mp: 175-176 °C; IR: (KBr,  $\text{cm}^{-1}$ ): 3264, 2944, 2752, 1820, 1758, 1603, 1520, 1445, 1386, 1316, 1270, 1174, 1054;  $^1\text{H NMR}$  ( $\text{DMSO-d}_6$ ,  $\delta$  ppm): 0.91 (t, 3H,  $-\text{CH}_3$ ), 1.34-1.43 (m, 4H,  $2\text{CH}_2$ ), 1.73 (quintate, 2H,  $\text{CH}_2$ ), 2.62 (s, 3H, Ar- $\text{CH}_3$ ), 4.01 (t, 2H, O- $\text{CH}_2$ ), 7.00 (d, 2H,  $J=8\text{ Hz}$ , 2Ar-H), 7.86 (d, 2H,  $J=8\text{ Hz}$ , 2Ar-H); M.W.= 345; (M+1) = 346.

**7b:** Yield: 0.51 g (84 %); mp: 229-230 °C (Decomp.); IR: (KBr,  $\text{cm}^{-1}$ ): 3292, 2978, 1635, 1523, 1445, 1389, 1322, 1260, 1171, 1115, 1078, 818;  $^1\text{H NMR}$  ( $\text{DMSO-d}_6$ ,  $\delta$  ppm): 1.38 (t, 3H,  $-\text{CH}_3$ ), 2.59 (s, 3H, Ar- $\text{CH}_3$ ), 4.10 (q, 2H, O- $\text{CH}_2$ ), 4.49 (s, 1H, NH), 7.01 (d, 2H,  $J=8\text{ Hz}$ , 2Ar-H), 7.84 (d, 2H,  $J=8\text{ Hz}$ , 2Ar-H); M.W.= 303; (M+1) = 304.

**5-(4-Methyl-2-(4-(alkyloxy)phenyl)thiazol-5-yl)-1,3,4-oxadiazol-2-amine (8a and 8b)**

The solution of sodium bicarbonate (1.92 g, 0.0114 mol) in 10 mL of water was added to a solution of **3a** or **3b** (0.002 mol) in 20 mL dioxane at room temperature. After 10 minutes of stirring cyanogens bromide (0.266 g, 0.0025 mol) was added with stirring. After 3 h of stirring, the solid precipitates out filtered, dried and recrystallized from isopropyl alcohol to afford brown-colored product.

**8a:** Yield: 0.62 g (90 %); mp: 176-177 °C; IR: (KBr,  $\text{cm}^{-1}$ ): 3417, 3334, 3108, 3050, 2950, 1679, 1603, 1571, 1516, 1449, 1375, 1325, 1241, 1178, 1012;  $^1\text{H NMR}$  (DMSO- $d_6$ ,  $\delta$  ppm): 0.91 (t, 3H, -CH<sub>3</sub>), 1.39 (m, 4H, 2CH<sub>2</sub>), 1.75 (quintate, 2H, CH<sub>2</sub>), 2.67 (s, 3H, Ar-CH<sub>3</sub>), 4.02 (t, 2H, O-CH<sub>2</sub>), 7.01 (d, 2H,  $J=8$  Hz, 2Ar-H), 7.29 (s, 2H, NH<sub>2</sub>), 7.87 (d, 2H,  $J=8$  Hz, 2Ar-H); M.W.= 344; (M+1) = 345

**8b:** Yield: 0.58 g (96 %); mp: 230-231 °C; IR: 3416, 3336, 3101, 1686, 1602, 1569, 1518, 1445, 1389, 1322, 1255, 1176, 1115, 1036 (KBr,  $\text{cm}^{-1}$ );  $^1\text{H NMR}$  (DMSO- $d_6$ ,  $\delta$  ppm): 1.38 (t, 3H, -CH<sub>3</sub>), 2.67 (s, 3H, Ar-CH<sub>3</sub>), 4.10 (q, 2H, O-CH<sub>2</sub>), 4.46 (s, 2H, NH<sub>2</sub>), 7.01 (d, 2H,  $J=8$  Hz, 2Ar-H), 7.28 (s, 2H, NH<sub>2</sub>), 7.87 (d, 2H,  $J=8$  Hz, 2Ar-H); M.W.= 302; (M+1) = 303.

**(5-Amino-3-phenyl-1H-pyrazol-1-yl)(4-methyl-2-(4-(alkyloxy)-phenyl) thiazol-5-yl)methanone (9a, 9b)**

A mixture of **3a** or **3b** (0.001 mol) and 3-oxo-3-phenylpropanenitrile (0.145 g, 0.001 mol) in ethanol was refluxed for 6 h. After completion of reaction, the reaction mixture was allowed to cooled and solvent was removed under reduced pressure. Resulting solid was purified by column chromatography using n-hexane and ethyl acetate (9:1).

**9a:** Yield: 0.360 g (80 %); mp: 144-145 °C; IR: (KBr,  $\text{cm}^{-1}$ ): 3492, 3383, 2933, 1654, 1603, 1483, 1366, 1329, 1262, 1170, 945;  $^1\text{H NMR}$  (DMSO- $d_6$ ,  $\delta$  ppm): 0.92 (t, 3H, -CH<sub>3</sub>), 1.34-1.49 (m, 4H, 2CH<sub>2</sub>), 1.79 (quintate, 2H, CH<sub>2</sub>), 2.84 (s, 3H, Ar-CH<sub>3</sub>), 4.05 (t, 2H, O-CH<sub>2</sub>), 5.87 (s, 1H, Ar-H), 6.84 (s, 2H, NH<sub>2</sub>), 7.01 (d, 2H,  $J=8$  Hz, 2Ar-H), 7.41-7.50 (m, 3H, 3Ar-H), 7.88 (d, 2H,  $J=8$  Hz, 2Ar-H), 8.00 (d, 2H,  $J=8$  Hz, 2Ar-H); M.W.= 446; (M+1) = 447.

**9b:** Yield: 0.327 g (81 %); mp: 204-205 °C; IR: (KBr,  $\text{cm}^{-1}$ ): 3416, 3225, 2988, 1663, 1602, 1479, 1367, 1328, 1255, 1171, 1042, 892;  $^1\text{H NMR}$  (DMSO- $d_6$ ,  $\delta$  ppm): 1.41 (t, 3H, -CH<sub>3</sub>), 2.84 (s, 3H, Ar-CH<sub>3</sub>), 4.12 (q, 2H, O-CH<sub>2</sub>), 5.88 (s, 1H, Ar-H), 6.88 (s, 2H, NH<sub>2</sub>), 7.04 (d, 2H,  $J=8$  Hz, 2Ar-H), 7.41-7.50 (m, 3H, 3Ar-H), 7.9 (d, 2H,  $J=8$  Hz, 2Ar-H), 8.00 (d, 2H,  $J=8$  Hz, 2Ar-H); M.W.= 404; (M+1) = 405.

**(Ethyl 5-amino-1H-pyrazol-1-yl-4-carboxylate)(4-methyl-2-(4-(alkyloxy)phenyl)thiazol-5-yl)methanone (10a, 10b)**

A mixture of **3a** or **3b** (0.001 mol) and ethyl (ethoxymethylene)cianoacetate (0.169 g, 0.001 mol) in ethanol (10 mL) was heated under reflux for 10 hours. After completion of reaction the reaction mixture was allowed to

cool and the solvent was reduced under reduced pressure. The resulting solid was purified by column chromatography using n-hexane and ethyl acetate (9:1).

**10a:** Yield: 0.360 g (81 %); mp: 173-174 °C; IR: (KBr,  $\text{cm}^{-1}$ ): 3458, 3334, 2975, 1687, 1670, 1612, 1553, 1479, 1362, 1329, 1287, 1253, 1174, 1108, 1049, 887;  $^1\text{H NMR}$  (CDCl<sub>3</sub>,  $\delta$  ppm): 0.94 (t, 3H, -CH<sub>3</sub>), 1.36 (t, 3H, -CH<sub>3</sub>), 1.40-1.48 (m, 4H, 2CH<sub>2</sub>), 1.81 (quintate, 2H, CH<sub>2</sub>), 2.89 (s, 3H, Ar-CH<sub>3</sub>), 4.02 (t, 2H, O-CH<sub>2</sub>), 4.31 (t, 2H, O-CH<sub>2</sub>), 6.91 (d, 2H,  $J=8$  Hz, 2Ar-H), 7.24 (s, 2H, NH<sub>2</sub>), 7.75 (s, 1H, Ar-H), 8.00 (d, 2H,  $J=8$  Hz, 2Ar-H); M.W.= 442; (M+1) = 443.

**10b:** Yield: 0.345 g (86 %); mp: 205-206 °C; IR: (KBr,  $\text{cm}^{-1}$ ): 3449, 3336, 2978, 1691, 1669, 1602, 1557, 1361, 1328, 1288, 1249, 1171, 1104, 886;  $^1\text{H NMR}$  (CDCl<sub>3</sub>,  $\delta$  ppm): 1.36 (t, 3H, -CH<sub>3</sub>), 1.44 (t, 3H, -CH<sub>3</sub>), 2.89 (s, 3H, Ar-CH<sub>3</sub>), 4.10 (q, 2H, O-CH<sub>2</sub>), 4.31 (q, 2H, O-CH<sub>2</sub>), 6.95 (d, 2H,  $J=8$  Hz, 2Ar-H), 7.24 (s, 2H, NH<sub>2</sub>), 7.75 (s, 1H, Ar-H), 8.00 (d, 2H,  $J=8$  Hz, 2Ar-H); M.W.= 400; (M+1) = 401.

**CONCLUSION**

A series of new thiazole derivatives was synthesized and screened for antiproliferative activity. Compounds **4a**, **5a**, **6a**, **7a**, **8a**, **7b** showed less activity while compound **9b** was found to show moderate activity (IC<sub>50</sub>) as compare to standard anticancer drug Paclitaxel.

**ACKNOWLEDGEMENT**

The authors are thankful to The Principal, V. P. Mahavidyalaya, Vaijapur and The Principal, Deogiri College, Aurangabad for providing laboratory facilities. The authors are also thankful to The Director, SAIF, Chandigarh for providing spectral analysis.

**REFERENCES**

- Wani, M. Y., Ahmad, A., Shiekh, R. A., Alghamdi, K. J., Sobral, A. J., Imidazole clubbed 1,3,4-oxadiazole derivatives as potential antifungal agents, *Biorg. Med. Chem.*, **2015**, *23*, 4172-4180. <https://doi.org/10.1016/j.bmc.2015.06.053>
- Farshori, N. N., Banday, M. R., Ahmad, A., Khan, A. U., Rauf, A., Synthesis, characterization, and in vitro antimicrobial activities of 5-alkenyl/hydroxyalkenyl-2-phenylamine-1,3,4-oxadiazoles and thiadiazoles, *ChemInform abstract:Bioorg.Med. Chem. Lett.*, **2010**, *20*, 1933-1938. <https://doi.org/10.1016/j.bmc.2010.01.126>
- Li, Z., Zhan, P., Liu, X., 1,3,4-Oxadiazole: a privileged structure in antiviral agents, *Mini Rev. Med. Chem.*, **2011**, *11*(13), 1130-11342. <https://doi.org/10.2174/138955711797655407>
- Durgashivaprasad, E., Mathew, G., Sebastian, S., Reddy, S. A., Mudgal, J., Nampurath, G. K., Novel 2,5-disubstituted-1,3,4-oxadiazoles as anti-inflammatory drugs, *Indian J. Pharmacol.*, **2014**, *46*, 521-526. <https://doi.org/10.4103/0253-7613.140584>
- Kumar, A., D'Souza, S. S., Nagaraj, S. R., Gaonkar, S. L., Salimath, B. P., Rai, K. M., Antiangiogenic and antiproliferative effects of substituted-1,3,4-oxadiazole derivatives is mediated by down regulation of VEGF and inhibition of translocation of HIF-1 $\alpha$  in Ehrlich ascites tumor cells, *Cancer Chemother. Pharmacol.*, **2009**, *64*, 1221-1233. <https://doi.org/10.1007/s00280-009-0992-y>

- <sup>6</sup>Singh, P., Sharma, P. K., Sharma, J. K., Upadhyay, A., Kumar, N., Synthesis and evaluation of substituted diphenyl-1,3,4-oxadiazole derivatives for central nervous system depressant activity, *Org. Med. Chem. Lett.*, **2012**, 2, 28-36. <https://doi.org/10.1186/2191-2858-2-8>
- <sup>7</sup>Bansal, S., Bala, M., Suthar, S. K., Choudhary, S., Bhattacharya, S., Bhardwaj, V., Singla, S., Joseph, A., Design and synthesis of novel 2-phenyl-5-(1,3-diphenyl-1H-pyrazol-4-yl)-1,3,4-oxadiazoles as selective COX-2 inhibitors with potent anti-inflammatory activity, *Eur. J. Med. Chem.*, **2014**, 80, 167-174. <https://doi.org/10.1016/j.ejmech.2014.04.045>
- <sup>8</sup>Khanam, R., Ahmad, K., Hejazi, I. I., Siddique, I. A., Kumar, V., Bhat, A. R., Azam, A., Athar, F., Inhibitory growth evaluation and apoptosis induction in MCF-7 cancer cells by new 5-aryl-2-butylthio-1,3,4-oxadiazole derivatives, *Cancer Chemother. Pharmacol.*, **2017**, 80, 1027-1042. <https://doi.org/10.1007/s00280-017-3414-6>
- <sup>9</sup>Steigbigel, R. T., Cooper, D. A., Kumar, P. N., Eron, J. E., Schechter, M., Markowitz, M., Loutfy, M. R., Lennox, J. L., Gatell, J. M., Rockstroh, J. K., Katlama, C., Yeni, P., BENCHMRK Study Teams, Raltegravir with Optimized Background Therapy for Resistant HIV-1 Infection, *New Engl. J. Med.*, **2008**, 359(4), 339-354. <https://doi.org/10.1056/nejmoa0708975>
- <sup>10</sup>Kumar, V., Kaur, K., Gupta, G. K., Sharma, A. K., Pyrazole containing natural products: Synthetic preview and biological significance, *Eur. J. Med. Chem.*, **2013**, 69, 735-753. <https://doi.org/10.1016/j.ejmech.2013.08.053>
- <sup>11</sup>Ju, Y., Varma, R. S.; Aqueous N-Heterocyclization of Primary Amines and Hydrazines with Dihalides: Microwave-Assisted Syntheses of N-Azacycloalkanes, Isoindole, Pyrazole, Pyrazolidine, and Phthalazine Derivatives, *J. Org. Chem.*, **2006**, 71(1), 135-141. <https://doi.org/10.1021/jo051878h>
- <sup>12</sup>Küçükgülzel, Ş. G.; Şenkardeş, S.; Recent advances in bioactive pyrazoles, *Eur. J. Med. Chem.*, **2015**, 97, 786-815. <https://doi.org/10.1016/j.ejmech.2014.11.059>
- <sup>13</sup>Alam, O., Naim, Md. J., Nawaz, F., Alam, Md. J., Alam, P., Current status of pyrazole and its biological activities; *J. Pharm. Bioallied. Sci.*, **2016**, 8(1), 2-17. <https://doi.org/10.4103/0975-7406.171694>
- <sup>14</sup>Faria, J. V., Vegi, P. F., Miguita, A. G. C., Santos, M. S. D., Boechat, N.; Bernardino, A. M. R.; Recently reported biological activities of pyrazole compounds, *Bioorg. Med. Chem.*, **2017**, 25(21), 5891-5903. <https://doi.org/10.1016/j.bmc.2017.09.035>
- <sup>15</sup>Dake, S. A., Raut, D. S., Kharat, K. R., Mhaske, R. S., Deshmukh, S. U., Pawar, R. P., Ionic liquid promoted synthesis, antibacterial and in vitro antiproliferative activity of novel a-aminophosphonate derivatives, *Bioorg. Med. Chem. Lett.*, **2011**, 21, 2527-2532. <https://doi.org/10.1016/j.bmcl.2011.02.039>

Received: 15.02.2020.

Accepted: 20.04.2020.



# NEODYMIUM(III) SORPTION ONTO SODIUM BENTONITE AND MAGNETIC ACTIVATED CARBON: A COMPARATIVE STUDY

Abdelkader Miraoui<sup>[a]</sup> and Mohamed Amine Didi<sup>[a]\*</sup>

**Keywords:** Neodymium, sodium bentonite, magnetic activated carbon removal, kinetics.

In this paper, the liquid-solid extraction of neodymium(III) by sodium bentonite and magnetic activated carbon was reported. Neodymium (Nd) is a key element that widely applied in high-tech industries; various parameters, such as: the time, metal concentration, ionic strength, effect of initial pH etc., have been studied to assess the efficiency of sodium bentonite and magnetic activated carbon for the removal of Nd(III). Optimal extraction yield was achieved at pH equal to 9.1 for sodium bentonite and in the range of pH<sub>i</sub> from 3.1 to 9.2 for the magnetic activated carbon. The time needed for magnetic activated carbon to absorb the maximum of Nd(III) is 100 min and 60 min for sodium bentonite. The experimental capacity obtained was 528 mg g<sup>-1</sup> for magnetic activated carbon and 503 mg g<sup>-1</sup> for sodium bentonite. In order to validate the performance of this extractants, kinetics and diffusional studies were also developed throughout this study. Adsorption equilibrium data were calculated for Langmuir and Freundlich isotherms. It was found that the sorption of Nd(III) on sodium and magnetic activated carbon was better suited to the Freundlich adsorption model.

\* Corresponding Authors

Fax: +21352639237

E-Mail: madidi13@yahoo.fr

[a] Laboratory of Separation and Purification Technologies,  
Department of Chemistry- Faculty of Sciences, Box119,  
Tlemcen University -13000, Algeria.

## INTRODUCTION

The rare earth elements (REEs), including lanthanide elements as well as yttrium and scandium, are 17 in number. They are divided conventionally into two groups: the light group (Sc, La, Ce, Pr, Nd, Pm, Sm, Eu, Gd) and the heavy group (Y, Tb, Dy, Ho, Er, Tm, Yb, Lu). The REEs are widely used in various field, such as chemical engineering, metallurgy, nuclear energy, optical, magnetic, luminescence, laser materials, high-temperature superconductors and secondary batteries, catalysis, red phosphors etc.<sup>1-4</sup> Rare earth elements (REEs) are of great importance owing to their unique physical and chemical properties best suited for the creation of advanced materials for high-technology devices.<sup>5,6</sup> A significant increase of rare earth metals production is expected in the coming years due to increasing demand for them.<sup>7</sup> Rare earth ores tend to be localized, and often include radioactive elements<sup>8</sup>, they occur together in nature in some minerals, e.g. bastnasite, monazite and xenotime.<sup>9</sup>

Neodymium is one of the most abundant rare earth elements. Neodymium (Nd) is an important member of the first triad of the lanthanide series and its atomic number being 60.<sup>2,5,6,9</sup> Neodymium compounds were first commercially used as a glass dye and they are still used as a popular additive in glass. Its color, due to the Nd(III) ion, is often reddish-purple but changes with the type of lighting due to fluorescent effects. Neodymium oxides are also used as a laser material to replace ruby in order to produce a coherent light, as components of advanced materials such as high temperature ceramics and superconductors, and in catalytic systems.<sup>10</sup> Neodymium gains great attention due to

high demand in the Nd-Fe-B magnet industry, especially in high performance electric motors in hybrid electric vehicles and direct-drive wind turbine generators.<sup>1, 3,11</sup> Neodymium-iron-boron permanent magnets is costs less than samarium-cobalt permanent magnets.<sup>2,5</sup> Currently, (Nd-Fe-B) permanent magnets are used in hard disk drives, motors in hybrid cars and MRI machines, among others.<sup>8</sup> Since the development of the iron-neodymium-boron (Nd-Fe-B) permanent magnet in 1980, the production volume of neodymium metal has increased dramatically. Currently, about 10,000 tons of Nd-FeB alloy magnets are produced annually.<sup>3,8,12</sup> The separation from other rare earth elements requires energy consuming procedures; therefore, there is an industrial demand for the recycling of neodymium from scrap to save time and energy.<sup>8,12</sup>

Various methods can be used to recover this metal from aqueous solutions. Traditional methods, for example such as ion exchange, precipitation and solvent extraction have been found to be ineffective at a very low concentration of contaminated metal ions.<sup>2</sup> Adsorption is the most popular method in which activated carbon or ion exchange resins are usually applied. Adsorption phenomenon in solution systems plays a vital role in many areas of practical environmental technology, which are mainly in water and wastewater treatment due to several advantages such as high efficiency, simple operation and easy recovery/reuse of adsorbent.<sup>13</sup>

In recent years, the preparation of organic-inorganic superabsorbent composites has attracted great attention because of their relatively low production cost, high water absorbency and their considerable range of applications in agriculture and horticulture.<sup>14</sup> Recently, clays and clay minerals were found to be very important for preparation of this super absorbent nanocomposite.<sup>15</sup> The bentonite materials exhibit highly interesting properties, e.g. high specific surface area, cation exchange capacity (CEC), porosity, and tendency to retain water or other polar and non-polar compounds.<sup>16</sup>

An innovative technology that gains attention is the use of magnetic materials for magnetic separation of pollutants from effluents. In environmental applications, magnetic separation can be a promising method for a novel purification technique because it produces no contaminants such as flocculants and has the capability to treat a large amount of wastewater within a short time, and magnetic adsorbent can be quickly separated from a medium by a simple magnetic process.<sup>17,18</sup>

In this paper, the liquid-solid extraction of neodymium is performed by sodic bentonite and magnetic activated carbon. Various parameters have been studied to assess the performance of sodic bentonite and magnetic activated carbon for the removal of Nd(III). The nature and the properties of the sorbent materials play an important role in the effective retention of analytes from the sample solution.<sup>19</sup>

## EXPERIMENTAL

### Reagents

Neodymium solution at  $10^{-2}$  M was prepared by dissolving of neodymium nitrate (3.3025 g) in 1 L of distilled water (purchased from Sigma-Aldrich). The initial pH of the sample solutions were adjusted by using dilutes  $\text{HNO}_3$  or  $\text{NaOH}$  (from Sigma-Aldrich).  $\text{NaNO}_3$  (from Merck)  $\text{Na}_2\text{S}_2\text{O}_3$  (from Merck) were used in the salt effect. Arsenazo III solution ( $10^{-3}$  M) from Fluka was prepared by dissolving 0.0820 g sample in absolute ethanol. Hydrochloric acid (from Organics), sulfuric acid (from Fluka), nitric acid (from Cheminova) and acetic acid (from Riedel de Haen) were used from elution study.

The natural bentonite used in this study was obtained from deposits in the area of Maghnia, Algeria. For synthesis of magnetic activated carbon,  $\text{FeCl}_2 \cdot 4\text{H}_2\text{O}$  (from Sigma Aldrich),  $\text{FeCl}_3 \cdot 6\text{H}_2\text{O}$  (from Panreac), activated carbon (Aldrich Chemical Company Inc.),  $\text{NH}_4\text{OH}$  (from Sigma-Aldrich),  $\text{HNO}_3$  and  $\text{Fe}(\text{NO}_3)_2$  (from Sigma Aldrich) were used.

### Apparatus

The extraction of Nd(III) was studied by the batch process using a stirring vibrator (Haier model). pH measurements were performed with a pH meter using a combined electrode mark (Adwa). Thermogravimetric analyses of samples (TGA) were performed using a SDT Q600 thermogravimetric analyzer at a heating rate of  $20^\circ\text{C min}^{-1}$ , under nitrogen atmosphere, at Tlemcen-Algeria. FTIR was performed using a Cary 630 FTIR from Agilent Technologies, at Tlemcen-Algeria. The BET- $\text{N}_2$  method was used to determine the specific surface area of the bleaching earths, using a Volumetric Analyzer (Nova-1000). A magnet and centrifugation for the recovery of the magnetic activated carbon and sodium bentonite, respectively, in the aqueous phase were used. Samples containing Nd(III) were analyzed by spectrophotometer (Analytik Jena Specord 210 Plus) with Arsenazo III as ligand.

### Preparation of sodium bentonite

For the purification of bentonite, 120 g of natural bentonite was dispersed in 1.5 L of distilled water, and after agitation during 15 min; a buffer solution of sodium citrate (pH 7.3) was added. The mixture was heated under agitation at  $75^\circ\text{C}$  for 20 min and then, 15 g of sodium thiosulfate ( $\text{Na}_2\text{S}_2\text{O}_4$ ) was slowly added. After 15 min under agitation, the mixture was cooled and centrifuged at a rotational speed of 6000 rpm for 15 min. The solid recovered was washed two times with  $\text{HCl}$  0.05 M (1.5 L) during 3 h.

To convert the purified bentonite into sodium form an amount of bentonite was dispersed in  $\text{NaCl}$  solution (1 M) with a 1/5 mass ratio and after agitation for 2 h, the solid was separated by centrifugation at a rotational speed of 6000 rpm for 15 min, this operation was repeated three times. The solid was washed three times with distilled water, and it was dried at  $40^\circ\text{C}$  for 3 days.<sup>13</sup>

The chemical composition of purified bentonite was found to be 64.7 %  $\text{SiO}_2$ , 18.1 %  $\text{Al}_2\text{O}_3$ , 0.95 %  $\text{Fe}_2\text{O}_3$ , 2.66 %  $\text{MgO}$ , 0.8 %  $\text{K}_2\text{O}$ , 0.61 %  $\text{CaO}$ , 0.2 %  $\text{TiO}_2$ , 1.43 %  $\text{Na}_2\text{O}$ , 0.05% As, 10.0% loss on ignition. The cation-exchange capacity (CEC) of bentonite was determined according to the ammonium acetate saturation method and was found to be 0.070 equiv. per 100 g of dry natural-Bt and 0.098 equiv per 100 g of dry Na-Bt. The BET specific surface area increase from  $50\text{ m}^2\text{ g}^{-1}$  in natural-Bt to  $95\text{ m}^2\text{ g}^{-1}$  in Na-Bt.<sup>13</sup>

### Preparation of magnetic activated carbon

Dissolved  $\text{FeCl}_3$  (7.8 g, 28 mmol) and  $\text{FeSO}_4$  (3.9 g, 14 mmol) in 400 mL of water at  $70^\circ\text{C}$ . Added 3.3, 6.6 or 9.9 g of activated carbon in different solutions to obtain the following adsorbent:iron oxide w/w ratios 1.0:1.0, 1.5:1.0 and 2.0:1.0. To these suspensions added a solution of  $\text{NaOH}$  (100 mL, 5 mol  $\text{L}^{-1}$ ) drop wise to precipitate the iron oxides. Washed the obtained solid materials with distilled water and dried in an oven at  $100^\circ\text{C}$  for 2 h. After the preparation a simple test with a magnet (0.3 T) was carried out showing that the whole material is completely attracted to the magnet.<sup>20</sup>

### Extraction and analysis procedure

The batch experiments were carried out to evaluate the adsorption processes and the equilibrium states of Neodymium mobilization. Nd(III) solution was prepared by dilution of the high purity stock standard solution ( $10^{-2}$  mol  $\text{L}^{-1}$ ). 4 mL of Nd(III) solution of known concentration, and 0.01 g of solid adsorbent (sodium bentonite or magnetic activated carbon) were mixed in an Erlenmeyer flask with stopper, under vigorous stirring. Both liquid and solid phases were separated by centrifugation for sodium bentonite and by magnet for magnetic activated carbon. The solid phase was regenerated for other applications and the liquid phase was measured by the UV-visible spectrometer.<sup>21</sup> The sample of Nd(III) was analyzed by a mixture of 100  $\mu\text{L}$  Arsenazo III and 100  $\mu\text{L}$  of Nd(III) in a medium of pH=3.0. The product of interaction of Arsenazo III with Nd(III) was determined at  $\lambda_{\text{max}}=653\text{ nm}$ .<sup>22</sup>

The percentage of neodymium ions that was extracted by the magnetic particles was determined by Eqn. (1) and the rate of Nd uptake,  $q_t$  ( $\text{mg g}^{-1}$ ), was determined by Eqn. (2), where  $C_i$ ,  $C_t$  and  $C_e$  were the initial, time and equilibrium Nd(III) concentration ( $\text{mol L}^{-1}$ ), respectively;  $V$  (4 mL) was the volume solution;  $M$  molecular weight ( $\text{g mol}^{-1}$ ), and  $m$  was the mass of the particles magnetic used (0.01 g).<sup>18,21</sup>

$$\varphi = \frac{C_i - C_e}{C_i} 100 \quad (1)$$

where  $\varphi$  is the extraction yield in %.

$$q(\text{mg} / \text{g}) = (C_0 - C_e)V \frac{M}{m} \quad (2)$$

### Desorption procedure

After saturation of the magnetic particle by the neodymium ions, the regeneration of adsorbents is an important aspect in adsorption, using the HCl, HNO<sub>3</sub>, H<sub>2</sub>SO<sub>4</sub>, CH<sub>3</sub>COOH. We can determine the best eluting agent with Eqn. (3).<sup>18,21</sup>

## RESULTS AND DISCUSSION

### TGA of magnetic activated carbon

TGA of magnetic activated carbon showed a weight loss due to water vapor of approximately 10 % at temperatures lower the 100 °C and a weight loss of 65 % between 350 and 500 °C relating to the oxidation of carbon. A residual weight of 25 % was found after the oxidation of the activated carbon, bonded to the Fe oxide in the composite.

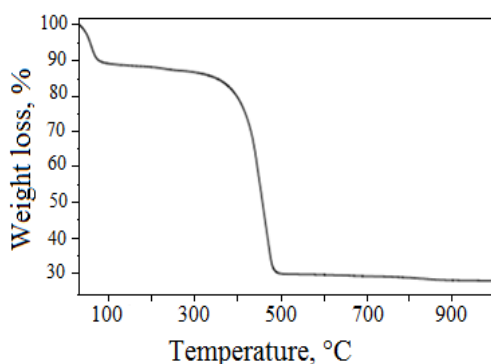


Figure 1. TGA patterns of magnetic activated carbon.

### BET Analysis

BET surface area and microporous volumes obtained for both composites are shown in Table 1.

BET analysis showed that the specific surface area and micropore volume are affected by the presence of iron oxide in the magnetic activated carbon. It is found that the specific surface area decreases from 931 to 656  $\text{m}^2 \text{g}^{-1}$  and we also noticed a decrease in the volume of micropores from 0.263 to 0.176  $\text{cm}^3 \text{g}^{-1}$ . In both cases, a reduction of 30 % corresponds to the presence of iron oxide in the magnetic activated carbon.

Table 1. BET surface areas and microporous volumes for magnetic activated carbon.

Composite	BET surface area ( $\text{m}^2 \text{g}^{-1}$ )	$V_{\text{micropores}}$ ( $\text{cm}^3 \text{g}^{-1}$ )
Activated carbon	931	0.263
Magnetic activated carbon	656	0.176

### XRD analyses of magnetic activated carbon

The XRD analyses of magnetic activated carbon suggest the presence of magnetite or a maghemite in the structure of composites (Figure 2). The peaks of magnetic activated carbon appear broader suggesting smaller crystallite size (ca. 25 nm for Fe oxide and 16 nm for the magnetic activated carbon, obtained by Scherrer's equation). Weak diffraction peaks at  $d=2.45$  and  $2.70 \text{ \AA}$  are also observe which might be related to the presence of small amounts of goethite and also some hematite.

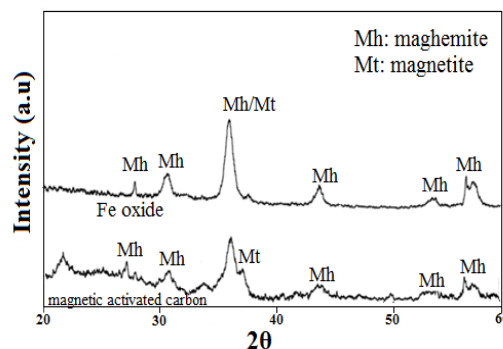


Figure 2. XRD for the magnetic activated carbon and Fe oxide.

### SEM micrograph

The morphologies of the magnetic activated carbon were studied by scanning electron microscopy (SEM) (Figure 3).

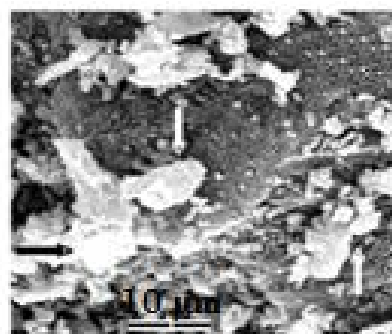
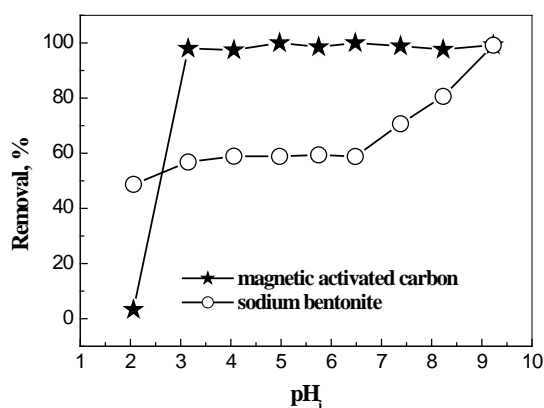


Figure 3. SEM micrograph of magnetic activated carbon.

### Effect of initial pH

Both the pH and the ionic strength of solutions are regarded as the key factors during adsorption process, which is related to the formation of soluble metal complexes and subsequently their stabilities in aqueous solutions. It is well known that surface charge of adsorbent can be modified by charging the pH of the solution and the chemical species in the solution depends on this parameter.<sup>1,23</sup> Sorption of thorium by magnetic activated carbon and sodium bentonite were studied at different pH ranging from 2.0 to 9.2 and the results are shown in Figure 4. The amount of magnetic particles, the initial concentration, and the contact time were kept to be constants. It is evident that percentage of extraction increases with increasing pH value in the range of 2.0 to 9.2 for sodium bentonite. At low pH values, protons are strongly competing with adsorbates.<sup>24-26</sup> Hence, adsorbent is less able to retain neodymium and adsorption of Nd is very low. After pH 2.0, adsorption of Nd increases sharply up to pH 3.0, for magnetic activated carbon. This evolution can be explained by the La Chatelier principle, when hydronium ions concentration decreases more (pH increase), the metal ions were extracted more and converted to the product. At this pH, (pH=3.0), the maximum yield extraction of Nd(III) was achieved.<sup>6,27</sup>



**Figure 4.** Removal of Nd(III) by magnetic activated carbon and sodium bentonite as a function of initial pH,  $[\text{Nd(III)}]_0=10^{-3} \text{ mol L}^{-1}$ ,  $w=0.01 \text{ g}$ ,  $V=4 \text{ mL}$ ,  $\varnothing=250 \text{ rpm}$ , room temperature.

### Effect of contact time

The fast recovery of target element on adsorbent is very important in a large scale application. Thus, the influence of contact time on the recovery of Nd(III) was examined to determine the time required for the attainment of adsorption equilibrium. The effect of equilibration time on the extraction of  $10^{-3} \text{ M}$ . Nd(III) with  $0.01 \text{ g}$  of sodium bentonite and magnetic activated carbon has been studied in the range 1-180 min.<sup>1, 28</sup>

Figure 5 illustrates the extraction yield as a function of time. It is seen that initially neodymium extraction yield increases as a function of time. For sodium bentonite, it reaches a maximum of 97 % in 10 min. For magnetic activated carbon, the time taken to reach a maximum of 97 % is 50 min. This difference can probably be attributed to a number of available active adsorption sites onto the two solid extractants.<sup>1</sup> After 10 min for sodium bentonite and 50 min for magnetic activated carbon, the Nd(III) adsorption did not change with time anymore. Hence, a contact time of

10 min and 50 min for sodium bentonite and magnetic activated carbon respectively, were sufficient to reach equilibrium. For sodium bentonite and magnetic activated carbon the  $t_{50}$  is 3 and 8 min, respectively. The equilibrium values of Nd uptake ( $q_e$ ) on the magnetic activated carbon and sodium bentonite are  $57.23 \text{ mg g}^{-1}$  and  $57.62 \text{ mg g}^{-1}$ , respectively.

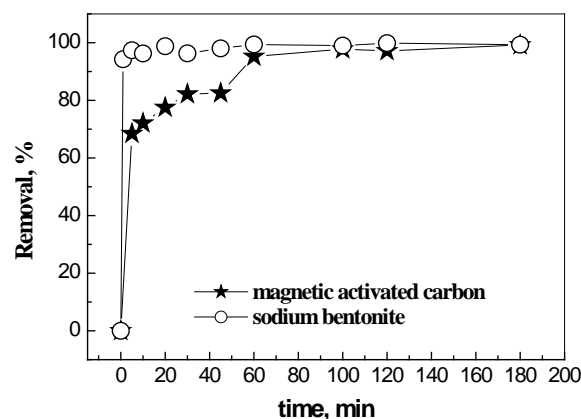


**Figure 5.** Removal of Nd(III) by magnetic activated carbon and sodium bentonite as a function of time,  $[\text{Nd(III)}]_0=10^{-3} \text{ mol L}^{-1}$ ,  $w=0.01 \text{ g}$ ,  $V=4 \text{ mL}$ ,  $\varnothing=250 \text{ rpm}$ , room temperature

### Adsorption kinetics

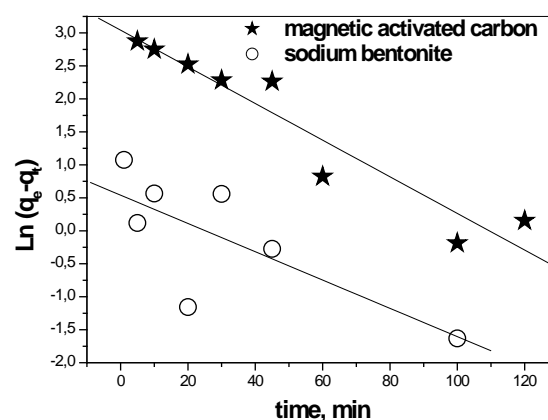


**Figure 6.** Pseudo-first order plot of Nd(III) adsorption kinetics onto the magnetic activated carbon and sodium bentonite as a function of time,  $w=0.01 \text{ g}$ ,  $V=4 \text{ mL}$ ,  $\varnothing=250 \text{ rpm}$ , room temperature.

Kinetics of sorption describing the solute uptake rate, which, in turn, governs the residence time of the sorption reaction, is one of the important characteristics defining the efficiency of sorption.<sup>29</sup> Two popularly used kinetic models, pseudo-first-order ( Eqn. 4) and pseudo-second-order ( Eqn. 5),<sup>27</sup> were used to fit the data, as shown in Figures 6 and 7, indicating the linear forms of the pseudo-first order and the pseudo-second order kinetics respectively.

$$\ln(q_e - q_t) = \ln q_e - k_1 t \quad (4)$$

$$\frac{t}{q_t} = \frac{1}{k_2 q_e^2} + \frac{t}{q_e} \quad (5)$$

Here  $q_e$  and  $q_t$  are the amounts of sorbed Nd(III) on magnetic activated carbon and sodium bentonite at equilibrium and at time  $t$ , respectively ( $\text{mg g}^{-1}$ ),  $k_1$  is the first-order adsorption rate constant ( $\text{min}^{-1}$ ),  $k_2$  is the pseudo-second-order adsorption rate constant ( $\text{g mg}^{-1} \text{min}^{-1}$ ).

The results presented in Figure 6, Figure 7 and Table 2 indicate that the pseudo-second-order kinetic model yields a better fit and suggest that the chemisorption processes could be a rate-limiting step. The correlation coefficients obtained are, 0.998 for magnetic activated carbon and 0.999 for sodium bentonite and the theoretical  $q_e$  values calculated from the pseudo-second-order equation are in agreement with the experimental data (Table 2), suggesting that adsorption system of neodymium by magnetic activated carbon and sodium bentonite are a pseudo-second-order reaction.

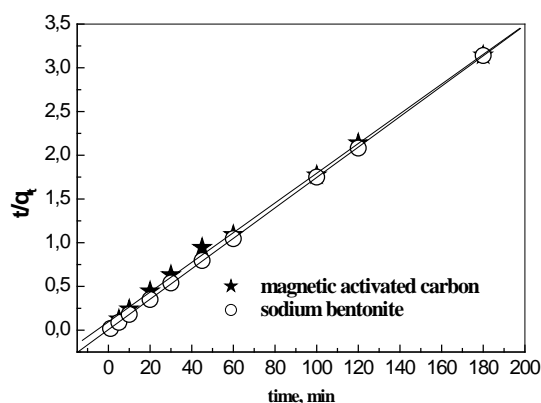


**Figure 7.** Pseudo-second order plot of Nd(III) adsorption kinetics onto the magnetic activated carbon and sodium bentonite as a function of time,  $w = 0.01$  g,  $V = 4$  mL,  $\Phi = 250$  rpm, room temperature.

**Table 2.** Comparison of the Pseudo-First order and Pseudo-Second order models for sorption of neodymium on magnetic activated carbon and sodium bentonite at ambient temperature.

Composite	$q_e$ (exp.) $\text{mg g}^{-1}$	Pseudo-first order	Pseudo-second order
Magnetic activated carbon	57.23	$R=0.954$ $q_e(\text{calc.}) =$ $20.92 \text{ mg g}^{-1}$ $K_1=0.021$	$R=0.998$ $q_e(\text{calc.}) =$ $58.82 \text{ mg g}^{-1}$ $K_2=0.003$
Sodium bentonite	57.62	$R=0.749$ $q_e(\text{calc.}) =$ $1.716 \text{ mg g}^{-1}$ $k_1=0.021$	$R=0.999$ $q_e(\text{calc.}) =$ $58.89 \text{ mg g}^{-1}$ $k_2=0.057$

Boyd relationship represents an intra-particle diffusion model as follows.<sup>30</sup>

$$\frac{q_t}{q_e} = 1 - \frac{6}{\pi^2} \sum_{n=1}^{\infty} \frac{e^{-x_n^2}}{n^2} \exp\left(-\frac{Dn^2\pi^2}{r^2}t\right) \quad (6)$$

Here  $D$  is the intra-particle diffusion coefficient and  $r$  is the particle radius. For short times (when  $q_t/q_e$  is less than 0.3), Eqn. (6) can be reduced to Eqn. (7).

$$q_t = k_{1D}\sqrt{t} \quad (7)$$

where  $k_{1D}$  is the intra-particle diffusion constant. The significant property of this equation is that, if the intra-particle diffusion is the only rate-limiting step, then the linear plot of  $q_t$  versus  $\sqrt{t}$  should pass through the origin. On the other hand, if the intercept of plots do not equal zero, then it indicates that the intra-particle diffusion is not the sole rate determining step.<sup>31</sup> Then Eqn. (7) is modified to Eqn. (8).<sup>32</sup>

$$q_t = k_{1D}\sqrt{t} + S \quad (8)$$

where  $S$  is a constant and reflects the boundary layer effect. Investigation of various reports about the sorption rate shows that the intra-particle diffusion model is the most popular one for the diffusion rate-controlling step that has been used in conjunction with the surface reaction models to recognize the adsorption kinetics.

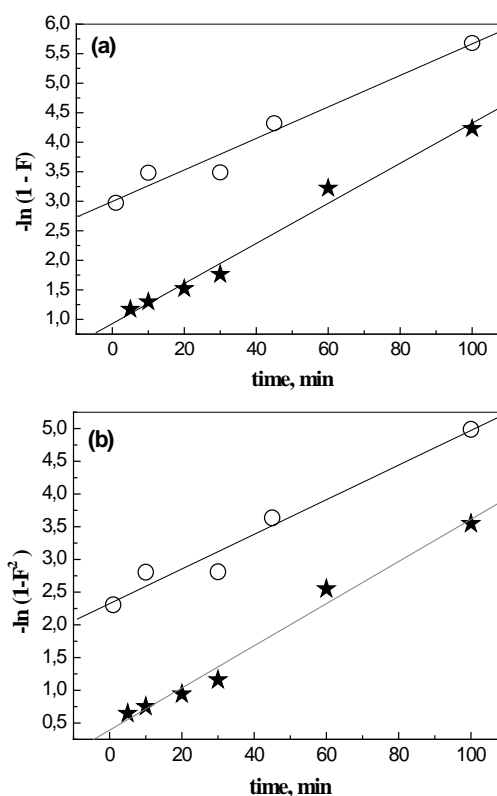


**Figure 8.** Intra-particle diffusion kinetic models for the adsorption of Nd(III), (a) magnetic activated carbon, (b) sodium bentonite,  $[\text{Nd(III)}]_0 = 10^{-3} \text{ mol L}^{-1}$ ,  $w = 0.01$  g,  $V = 4$  mL,  $\Phi = 250$  rpm, room temperature.

The plot of the Boyd relationship for the sorption of neodymium, at initial concentration equal to  $1 \text{ mmol L}^{-1}$ , by sodium bentonite and magnetic activated carbon is shown in Figure 8. Based on this Figure, it may be seen that the intra-particle diffusion of Nd(III) onto the sodium bentonite and magnetic activated carbon occurred in 2 stages. The first linear represent the external mass transfer or film diffusion (boundary layer) and the rapid distribution of Nd(III) molecules onto the outer surface of sodium and magnetic activated carbon. The second linear portion corresponds to the intra-particle diffusion and binding of Nd(III) molecules

into the internal active sites of the extractants. Moreover, the second stage of the lines does not pass through the origin. This means that the intra-particle diffusion, although important over longer contact time periods, is not the rate-limiting step in the adsorption process of Nd(III).<sup>13,18</sup>

### Diffusion study

The neodymium (III) transport from the solution phase to the surface of sodium bentonite and magnetic activated carbon occurs in several steps. The overall adsorption process may be controlled either by one or more of these steps. (i) The diffusion of ions from the solution to the surface of sodium bentonite and magnetic activated carbon, (ii) the diffusion of ions within the solid extractant, (iii) the chemical reaction between ions and functional groups of the extractants. If the liquid film diffusion controls the rate of exchange, the following relation can be used ( Eqn. 9).

$$-\ln(1-F) = kt \quad (9)$$

If the case of diffusion of ions in the sodium bentonite and magnetic activated carbon phase controlling process, then Eqn. (10) is used.

$$-\ln(1-F) = kt \quad (10)$$

where  $F$  is the fractional attainment of equilibrium, which is expressed as  $F=q/q_e$ . In both eqns. (9) and (10),  $k$  is the kinetic coefficient or rate constant.  $k$  is defined by eqn (11).

$$k = \frac{D_r \pi^2}{r_0^2} \quad (11)$$

where  $D_r$  is the diffusion coefficient in the sodium bentonite and magnetic activated carbon phase and  $r$  is the average radius of solids extractants.

When the adsorption of metal ion involves mass transfer accompanied by chemical reaction the process can be explained by the moving boundary model. This model assumes a sharp boundary that separates a completely reacted shell from an unreacted core and that advances from the surface toward the center of the solid with the progression of adsorption. In this case, the rate equation is given by Eqn. (12).<sup>27, 29</sup>

$$3-3(1-F)^{2/3}-2F = kt \quad (12)$$

The results of application of both the mathematical models are shown in Figure 9.

The comparison of the kinetic and diffusion parameters of Nd(III) sorption onto magnetic activated carbon and sodium bentonite (Table 3), shows that the adsorption of Nd(III) can be controlled by both diffusion model (film diffusion and particle diffusion) for both the extractants.

### Effect of initial metal concentration

Solutions of Nd(III) of different concentrations were prepared and mixed each with the same mass of adsorbent (0.01 g). The results showed that the amount of Nd(III) sorbed per unit mass of the particles magnetic increased with the initial metal concentration (Fig. 10). At a concentration of  $10^{-2}$  M of Nd(III), sorption capacities reach  $528 \text{ mg g}^{-1}$  for magnetic activated carbon and  $503 \text{ mg g}^{-1}$  for sodium bentonite. This sorption capacity is very interesting for liquid–solid extraction, because in the literature, most studies were done with liquid–liquid extraction.<sup>33-37</sup>

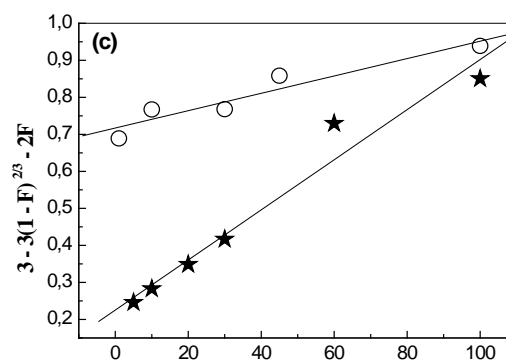


**Figure 9.** Plots of diffusion study for Nd(III) sorption on magnetic activated carbon (\*) and sodium bentonite (O) at different time.  $[\text{Nd(III)}]_0=10^{-3} \text{ mol L}^{-1}$ ,  $w=0.01 \text{ g}$ ,  $V=4 \text{ mL}$ ,  $\Phi=250 \text{ rpm}$ , room temperature: Film diffusion (a), interne diffusion (b), chemical reaction (c).

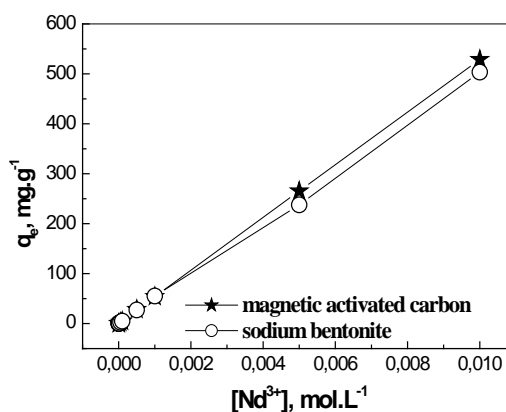


**Figure 10.** Removal of Nd(III) magnetic activated carbon and sodium bentonite as a function of  $[\text{Nd}]$ .  $w=0.01 \text{ g}$ ,  $V=4 \text{ mL}$ ,  $\Phi=250 \text{ rpm}$ , room temperature.

**Table 3.** Kinetic and diffusion parameters of neodymium sorption onto magnetic activated carbon and sodium bentonite.

$[\text{Nd(III)}]=10^{-3} \text{ M}$	Film diffusion Eqn. (9)	Particle diffusion Eqn. (10)	Chemical reaction Eqn. (12)
Magnetic activated carbon	$K=0.033 \text{ min}^{-1}$ $R=0.991$	$K=0.032 \text{ min}^{-1}$ $R=0.991$	$K=0.006 \text{ min}^{-1}$ $R=0.979$
Sodium bentonite	$K=0.026 \text{ min}^{-1}$ $R=0.981$	$K=0.026 \text{ min}^{-1}$ $R=0.981$	$K=0.002 \text{ min}^{-1}$ $R=0.951$

### Isotherm adsorption

The sorption data, commonly known as adsorption isotherms, are basic requirements for the design of adsorption systems.<sup>18</sup> The Freundlich and Langmuir isotherms are the most commonly used adsorption isotherms for describing a non-linear equilibrium of adsorbate between solution and adsorbent at a fixed temperature.<sup>1</sup> For the interpretation of both models, we have used the following equations.<sup>38</sup>

$$\frac{C_e}{q_e} = \frac{C_e}{q_m} + \frac{1}{q_m K_L} \quad (13)$$

$$\ln q_e = \ln K_F + n \ln C_e \quad (14)$$

where  $C_e$  is the equilibrium concentration of Nd(III) (in mg L<sup>-1</sup>),  $q_e$  is the amount of Nd(III) sorbed on the sodium and magnetic bentonite (mg g<sup>-1</sup>),  $K_L$  is the Langmuir adsorption constant (L mg),  $q_m$  is the maximum amount of Nd that can be sorbed,  $K_F$  is the Freundlich adsorption constant and  $n$  is a constant that indicates the capacity and intensity of the adsorption, respectively.

The Freundlich isotherm correlated better than Langmuir isotherm with the experimental data from adsorption equilibrium of neodymium ions by magnetic activated carbon and sodium bentonite ( Figures 11 and 12; Table 4). The correlation coefficients of Freundlich isotherm and Langmuir isotherm are very high.

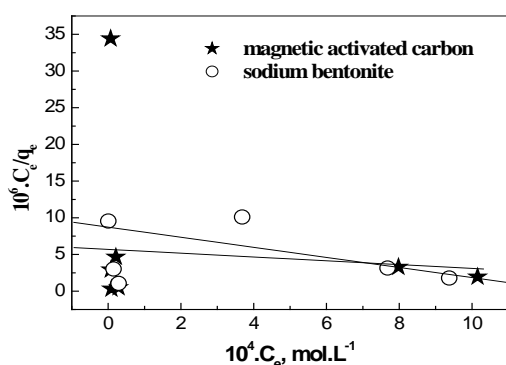


**Figure 11.** Langmuir isotherm plot for the sorption of Nd(III) onto and magnetic activated carbon and sodium bentonite.

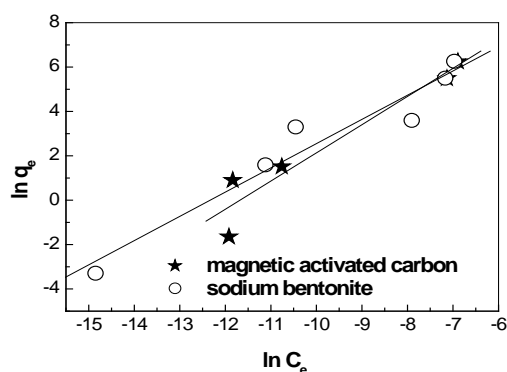


**Figure 12.** Freundlich isotherm plot for the sorption of Nd(III) onto and magnetic activated carbon and sodium bentonite.

### Effect of ionic strength

The effect of NaNO<sub>3</sub>, NH<sub>4</sub>NO<sub>3</sub> and Na<sub>2</sub>S<sub>2</sub>O<sub>3</sub> on the performance of extraction was studied. Figures 13 and 14 show the influence of ionic strength on sorption of neodymium by magnetic carbon activated and sodium bentonite.

**Table 4.** Isotherm models parameters for the adsorption of Nd(III) on magnetic activated carbon and sodium bentonite.

Composite	Langmuir isotherm	Freundlich isotherm
Magnetic activated carbon	$R=0.254$	$R=0.961$ $K_F=2757954.94$ $n=1.269$
Sodium bentonite	$R=0.268$	$R=0.968$ $K_F=707858.858$ $n=1.092$

Changing the ionic strength by the addition of an electrolyte influences adsorption in at least two ways,<sup>39,40</sup> one by affecting interfacial potential and therefore the activity of electrolyte ions and adsorption and secondly by affecting the competition of the electrolyte ions and adsorbing anions for sorption sites. Figures 13 and 14 show that the addition of all salts, increase the ionic strength and decrease extraction yield of Nd by magnetic activated carbon and sodium bentonite, this can be explained by a competitiveness in the extraction between Na<sup>+</sup>/NH<sub>4</sub><sup>+</sup> and Nd(III).<sup>41</sup>

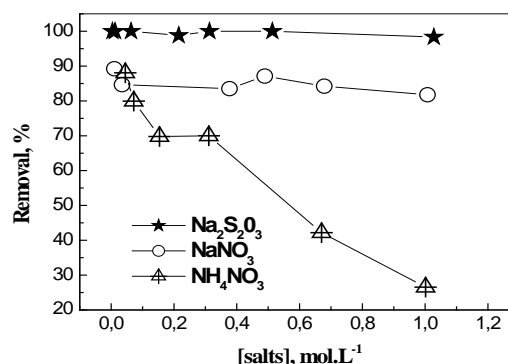


**Figure 13.** Removal of neodymium by magnetic activated carbon as a function of electrolytes under standard conditions.

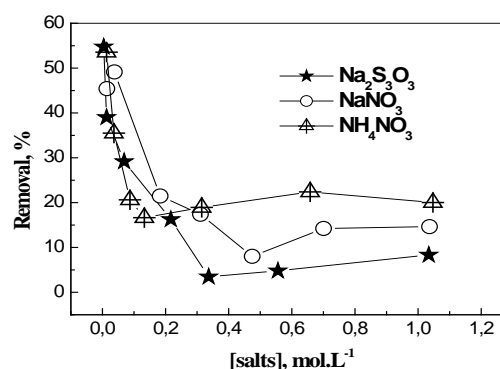


**Figure 14.** Removal of neodymium by magnetic activated carbon as a function of electrolytes under standard conditions.

## Desorption study

Desorption is a key process in sorption studies because it determines the economic value of the sorption process. To investigate the feasibility of regenerating used adsorbent, desorption experiments were performed using various eluting agents, namely HCl, HNO<sub>3</sub>, H<sub>2</sub>SO<sub>4</sub> and CH<sub>3</sub>COOH at a concentration of 0.5 mol L<sup>-1</sup> after Nd(III) adsorption. To a saturated sample the appropriate sorbent (0.01 g), 4 mL of the selected acid was added and kept for 3 h. The elution yield is calculated by Eqn. (3). Though hydrochloric acid, nitric acid and acetic acid have given significant elution yield for magnetic activated carbon (close to 100 % in a single step), sulfuric acid showed a less efficiency. The elution kinetics was made to optimize this study. Figure 16 show the kinetics of elution efficiency. This study shows that initially desorption of neodymium is rapid, it reaches a value of around 80 % after 10 min of agitation for the three acids. Between 10 and 100 min, the elution yield is stable then it reaches its maximum value after 150 min of agitation (around 100 %). The behaviour of the three acids for the desorption is similar.

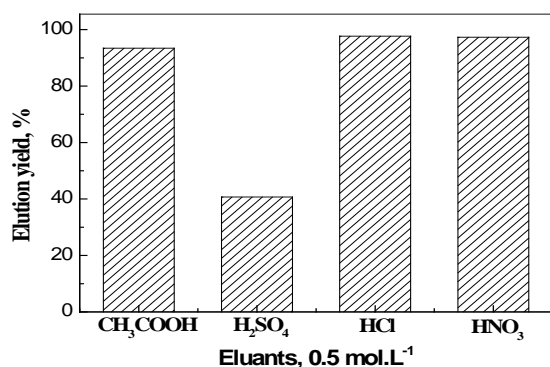


Figure 15. Optimum eluants for quantitative recovery of neodymium.

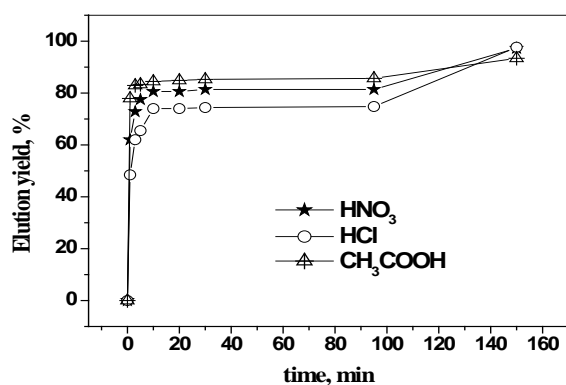


Figure 16. Effect of contact time on the desorption of Nd(III).

## CONCLUSION

The activated carbon magnetic and sodium bentonite were successfully applied for the removal of Nd(III) from seawater matrix. Equilibrium time, pH effect, kinetics, isotherms, ionic strength and effect of initial metal concentration were examined carefully. The characterization of magnetic activated carbon by BET, XDR and TEM indicate that the activated carbon was functionalized by iron oxide. The optimal adsorption efficiency could be observed

over 99.9 % at pH 9.2 for sodium bentonite and in a range between 3.1 and 9.2 for magnetic activated carbon. The pseudo-second order model accurately fits the Nd adsorption kinetics for both adsorbent and the data agrees well with Freundlich adsorption isotherm model. The experimental capacity obtained was 528 mg g<sup>-1</sup> for magnetic activated carbon and 508 mg g<sup>-1</sup> for sodium bentonite. The sorption of Nd(III) achieves equilibration at 100 and 60 min for magnetic activated carbon and sodium bentonite, respectively.

The synthesized magnetic activated carbon has the great potential for fast and effective neodymium recovery from seawater media. The magnetic activated carbon have superiority in separation, it can be quickly separated from a medium by a simple magnetic process and the results obtained in this comparative study make this magnetic particle as promising material for sorption, immobilization and pre-concentration of rare earth elements, radioactive metal and heavy metal ions from large volume of solutions.

## REFERENCES

- Yao-Jen, T., Sheng-Chung, L., Chen-Feng, Y., Selective and fast recovery of neodymium from seawater by magnetic iron oxide Fe<sub>3</sub>O<sub>4</sub>, *J. Chem. Eng.*, **2015**, 262, 966. <https://doi.org/10.1016/j.cej.2014.10.025>
- Wannachod, T., Phuphaibul, P., Mohdee, V., Pancharoen, U., Phatanasri, S., Optimization of synergistic extraction of neodymium ions from monazite leach solution treatment via HFSLM using response surface methodology, *Miner. Eng.*, **2015**, 77, 1. <https://doi.org/10.1016/j.mineng.2015.01.016>
- Anithaa, M., Ambarea, D. N., Singh, D. K., Singh, H., Mohapatra, P. K., Extraction of neodymium from nitric acid feed solutions using an emulsion liquid membrane containing TOPO and DNPPA as the carrier extractants, *J. Chem. Eng. Res. Des.*, **2015**, 98, 89. <https://doi.org/10.1016/j.chemd.2015.04.011>
- Panda, R., Jha, M. K., Hait, J., Kumar, G., Singh, R. J., Keun, Y., K., Extraction of lanthanum and neodymium from leach liquor containing rare earth metals (REMs), *Hydrometallurgy*, **2016**, 165, 106. <https://doi.org/10.1016/j.hydromet.2015.10.019>
- El-Hefny, N. E., Kinetics and mechanism of extraction and stripping of neodymium using a Lewis cell, *J. Chem. Eng. Process.*, **2007**, 46, 623. <https://doi.org/10.1016/j.ccep.2006.08.007>
- Gok, C., Neodymium and samarium recovery by magnetic nano-hydroxyapatite, *J. Radioanal. Nucl. Chem.*, **2014**, 301, 641. <https://doi.org/10.1007/s10967-014-3193-z>
- Aghayan, H., Mahjoub, A. R., Khanchi, A. R., Samarium and dysprosium removal using 11-molybdo-vanadophosphoric acid supported on Zr modified mesoporous silica SBA-15, *J. Chem. Eng.*, **2013**, 225, 509. <https://doi.org/10.1016/j.cej.2013.03.092>
- Onoda, H., Nakamura, R., Recovery of neodymium from an iron-neodymium solution using phosphoric acid, *J. Environ. Chem. Eng.*, **2014**, 2, 1186. <https://doi.org/10.1016/j.jece.2014.04.019>
- Wannachod, T., Leepipat Piboon, N., Pancharoen, U., Nootong, K., Synergistic effect of various neutral donors in D2EHPA for selective neodymium separation from lanthanide series via HFSLM, *J. Ind. Eng. Chem.*, **2014**, 20, 4152. <https://doi.org/10.1016/j.jiec.2014.01.014>
- Dedov, A. G., Loktev, A. S., Moiseev, I., Aboukais, A., Lamonier, J. F., Filimonov, A., Oxidative coupling of methane catalyzed by rare earth oxides: Unexpected

- synergistic effect of the oxide mixtures, *J. Appl. Catal.*, **2003**, *245*, 209. [https://doi.org/10.1016/S0926-860X\(02\)00641-5](https://doi.org/10.1016/S0926-860X(02)00641-5)
- <sup>11</sup>Ambare, D. N., Ansari, S. A., Anitha, M., Kandwal, P., Singh, D. K., Singh, H., Mohapatra, P. K., Non-dispersive solvent extraction of neodymium using a hollow fiber contactor: Mass transfer and modeling studies, *J. Membr. Sci.*, **2013**, *446*, 106. <https://doi.org/10.1016/j.memsci.2013.06.034>
- <sup>12</sup>Okabe, T. H., Takeda, O., Fukuda, K., Umetsu, Y., Direct Extraction and Recovery of Neodymium Metal from Magnet Scrap, *J. Mater. Trans.*, **2003**, *44*, 798. <https://doi.org/10.2320/matertrans.44.798>
- <sup>13</sup>Makhoukhi, B., Djab, M., Didi, M. A., Adsorption of Telen dyes onto bis-imidazolium modified bentonite in aqueous solutions, *J. Environ. Chem. Eng.*, **2015**, *3*, 1384. <https://doi.org/10.1016/j.jece.2014.12.012>
- <sup>14</sup>Bulut, Y., Akçay, G., Elma, D., Ersin Serhatli, I., Synthesis of clay-based superabsorbent composite and its sorption capability, *J. Hazard. Mater.*, **2009**, *171*, 717. <https://doi.org/10.1016/j.jhazmat.2009.06.067>
- <sup>15</sup>Wu, L., Ye, Y., Liu, F., Tan, C., Liu, H., Wang, S., Wang, J., Yi, W., Wu, W., Organo-bentonite-Fe<sub>3</sub>O<sub>4</sub> poly(sodium acrylate) magnetic superabsorbent nanocomposite: Synthesis, characterization, and Thorium(IV) adsorption, *J. Appl. Clay Sci.*, **2013**, *83-84*, 405. <https://doi.org/10.1016/j.clay.2013.07.012>
- <sup>16</sup>Makhoukhi, B., Didi, M. A., Moulessehoul, H., Azzouz, A., Villemin, D., Diphosphonium ion-exchanged montmorillonite for Telen dye removal from aqueous media, *J. Appl. Clay Sci.*, **2010**, *50*, 354. <https://doi.org/10.1016/j.clay.2010.08.026>
- <sup>17</sup>Ngomsik, A., Bee, A., Siaugue, J., Talbot, D., Cabuil, V., Cote, G., Co(II) removal by magnetic alginate beads containing Cyanex 272®, *J. Hazard. Mater.*, **2009**, *166*, 1043. <https://doi.org/10.1016/j.jhazmat.2008.11.109>
- <sup>18</sup>Miraoui, A., Didi, M. A., Extraction of thorium(IV) with sodium bentonite and maghemite containing magnetic nanocomposite bentonites, *Eur. Chem. Bull.*, **2015**, *4*, 512. <http://dx.doi.org/10.17628/ecb.2015.4.512-521>
- <sup>19</sup>Baghban, N., Shabani, M., Dadfarnia, S., Solid Phase Extraction of Trace Amounts of Cadmium with Cetyltrimethylammonium Bromide-Coated Magnetic Nanoparticles Prior to Its Determination by Flame Atomic Absorption Spectrometry, *J. Chin. Chem. Soc.*, **2012**, *59*, 782. <https://doi.org/10.1002/jccs.201100561>
- <sup>20</sup>Oliveira, L. C. A., Rios, R. V. R. A., Fabris, J. D., Lago, R. M., Magnetic Particle Technology. A Simple Preparation of Magnetic Composites for the Adsorption of Water Contaminants, *J. Chem. Educ.*, **2004**, *81*, 248. <https://doi.org/10.1021/ed081p248>
- <sup>21</sup>Miraoui, A., Didi, M. A., Villemin, D., Neodymium(III) removal by functionalized magnetic nanoparticles, *J. Radioanal. Nucl. Chem.*, **2016**, *307*, 963. <https://doi.org/10.1007/s10967-015-4267-2>
- <sup>22</sup>Kaczmarek, G., Meinrath, S., Kufelnicki, L., The Interaction of Arsenazo III with Nd(III)—A Chemometric and Metrological Analysis, *J. Solut. Chem.*, **2008**, *37*, 933. <https://doi.org/10.1007/s10953-008-9287-x>
- <sup>23</sup>Abderrahim, O., Ferrah, N., Didi, M. A., Villemin, D., A new sorbent for europium nitrate extraction: phosphonic acid grafted on polystyrene resin, *J. Radioanal. Nucl. Chem.*, **2011**, *290*, 267. <https://doi.org/10.1007/s10967-011-1243-3>
- <sup>24</sup>Prakorn, R., Ura, P., Synergistic extraction and separation of mixture of lanthanum and neodymium by hollow fiber supported liquid membrane, *J. Chem. Eng.*, **2003**, *20*, 724. <https://doi.org/10.1007/BF02706915>
- <sup>25</sup>Abderrahim, O., Didi, M. A., Moreau, B., Villemin, D., A New Sorbent for Selective Separation of Metal: Polyethylenimine Methylene phosphonic Acid, *J. Solv. Extr. Ion Exch.*, **2006**, *24*, 943. <https://doi.org/10.1080/07366290600952519>
- <sup>26</sup>Abderrahim, O., Ferrah, N., Didi, M. A., Villemin, D., Removal of copper ions from aqueous solutions by a new sorbent: Polyethyleneiminemethylene phosphonic acid, *Desalination*, **2011**, *269*, 17. <https://doi.org/10.1016/j.desal.2010.11.035>
- <sup>27</sup>Ferrah, N., Abderrahim, O., Didi, M. A., Villemin, D., Sorption efficiency of a new sorbent towards uranyl: phosphonic acid grafted Merrifield resin, *J. Radioanal. Nucl. Chem.*, **2011**, *289*, 721. <https://doi.org/10.1007/s10967-011-1172-1>
- <sup>28</sup>Panda, N., Bala Devi, N. R., Mishra, S., Extraction of neodymium(III) using binary mixture of Cyanex 272 and Cyanex 921/Cyanex 923 in kerosene, *J. Radioanal. Nucl. Chem.*, **2013**, *296*, 1205. <https://doi.org/10.1007/s10967-013-2425-y>
- <sup>29</sup>Esma, B., Omar, A., Amine, D. M., Comparative study on lanthanum(III) sorption onto Lewatit TP 207 and Lewatit TP 260, *J. Radioanal. Nucl. Chem.*, **2014**, *299*, 439.
- <sup>30</sup>Boyd, G. E., Adamson, A. W., Myers Jr., L. S., The Exchange Adsorption of Ions from Aqueous Solutions by Organic Zeolites. II. Kinetics, *J. Am. Chem. Soc.*, **1947**, *69*, 2836-2848. <https://doi.org/10.1021/ja01203a066>
- <sup>31</sup>Haerifar, M., Azizian, S., Mixed Surface Reaction and Diffusion-Controlled Kinetic Model for Adsorption at the Solid/Solution Interface, *J. Phys. Chem. C.*, **2013**, *117*, 8310. <https://doi.org/10.1021/jp401571m>
- <sup>32</sup>Barkakati, P., Begum, A., Das, M. L., Adsorptive separation of Ginsenoside from aqueous solution by polymeric resins: Equilibrium, kinetic and thermodynamic studies, *Chem. Eng. J.*, **2010**, *161*, 34. <https://doi.org/10.1016/j.cej.2010.04.018>
- <sup>33</sup>Rout, A., Kotlarska, J., Dehaen, W., Binnemans, K., Liquid-liquid extraction of neodymium(iii) by dialkylphosphate ionic liquids from acidic medium: the importance of the ionic liquid cation, *J. Phys. Chem.*, **2013**, *15*, 16533. <https://doi.org/10.1039/c3cp52218k>
- <sup>34</sup>Nayak, D., Lahiri, S., Das, N. R., Synergistic extraction of neodymium and carrier-free promethium by the mixture of HDEHP and PC88A, *J. Radioanal. Nucl. Chem.*, **1999**, *240*, 555. <https://doi.org/10.1007/BF02349413>
- <sup>35</sup>Sanchez, J. M., Hidalgo, M., Salvado, V., Valiente, M., Extraction of neodymium(III) at trace level with di(2-ethylhexyl)phosphoric acid in hexane, *J. Solv. Extr. Ion Exch.*, **1999**, *17*, 455. <https://doi.org/10.1080/07366299908934623>
- <sup>36</sup>El-Kot, A. M., Solvent extraction of neodymium, europium and thulium by di-(2-ethylhexyl)phosphoric acid, *J. Radioanal. Nucl. Chem.*, **1993**, *170*, 207. <https://doi.org/10.1007/BF02134592>
- <sup>37</sup>Kao, H., Yen, P., Juang, R., Solvent extraction of La(III) and Nd(III) from nitrate solutions with 2-ethylhexylphosphonic acid mono-2-ethylhexyl ester, *J. Chem. Eng.*, **2006**, *119*, 167. <https://doi.org/10.1016/j.cej.2006.03.024>
- <sup>38</sup>Kul, A. R., Koyuncu, H., Adsorption of Pb(II) ions from aqueous solution by native and activated bentonite: Kinetic, equilibrium and thermodynamic study, *J. Hazard. Mater.*, **2010**, *179*, 332. <https://doi.org/10.1016/j.jhazmat.2010.03.009>
- <sup>39</sup>Abderrahim, O., Didi, M. A., Villemin, D., A new sorbent for uranium extraction: Polyethyleniminephenylphosphonamidic acid, *J. Radioanal. Nucl. Chem.*, **2009**, *279*, 237. <https://doi.org/10.1007/s10967-007-7270-z>

<sup>40</sup>Vilar, V. J. P., Botelho, C. M. S., Boaventura, R. A. R., Influence of pH, ionic strength and temperature on lead biosorption by *Gelidium* and agar extraction algal waste, *J. Process. Biochem.*, **2005**, *40*, 3267.  
<https://doi.org/10.1016/j.procbio.2005.03.023>

<sup>41</sup>Didi, M. A., Villemin, D., Abderrahim, O., Azzouz, A., Liquid-liquid extraction of thorium(IV) by fatty acids: a comparative study, *J. Radioanal. Nucl. Chem.*, **2014**, *299*, 1191.  
<https://doi.org/10.1007/s10967-013-2855-6>

Received: 31.03.2020.

Accepted: 25.04.2020.



# ADVANCED NANOCATALYSTS FOR BIODIESEL PRODUCTION

Linus N. Okoro<sup>[a]\*</sup> and Gubihama Joel<sup>[a]</sup>

**Keywords:** : Nanocatalyst, transesterification, biodiesel, catalyst characterization, homogenous catalysts.

Global energy consumption is on the rise due to increasing industrial capacity of nations. This has made humans to be over reliant on fossil fuel for energy production. Diminishing fossil fuel reserve and long-term increase in average climate temperature has given rise to energy shortage and environmental degradation. Renewable energy is an alternative that will offer clean, sustainable and efficient energy. Solar, wind and hydro have all been explored in this regard. Biodiesel is another promising resource with great potential. It is diesel produced from organic sources containing free fatty acids through the transesterification reaction process that utilizes alcohols and catalysts. Research has been undertaken over the years to improve the efficiency of biodiesel production aimed at reducing complexities and cost. The type of catalysts used influences reaction conditions and biodiesel yield. Heterogeneous nanocatalyst has shown great potential in eradicating complexities and reducing cost. This review will focus on most recent research works that have used nanocatalyst to produce biodiesel. Possible areas of research can be explored for advancement in biodiesel production using nanotechnology.

\* Corresponding Authors

E-Mail: linus.okoro@aun.edu.ng

[a] Department of Petroleum Chemistry/Engineering  
School of Arts and Sciences, American University of Nigeria,  
Wuro Hausa 640101, Yola, Nigeria

## INTRODUCTION

Fossil fuel is an integral part of our day to day lives. It is the major source of energy to mankind. Due to high energy content associated with carbon fossil fuels, a large amount deposited in earth reserves have already been explored. This has resulted in energy shortage as fossil fuel reserves continue to diminish. Even with the advent of renewable energy resource, fossil fuel consumption rate continues to rise. At the present rate of consumption, experts predict complete run out of fossil fuels by the year 2050.<sup>1</sup>

Fossil fuels also emit greenhouse gases which depletes the ozone layer thereby increasing global temperature levels. One effective way of controlling global warming is through reduction on the use of fossil fuels. This can be achieved by using renewable energy from wind, solar and hydrothermal sources. Various technologies have emanated from these sources and are already in use in many countries. Experts have projected an estimated 70 % drop in greenhouse gas emissions by 2040 due to increase in the demand and use of renewable energy.<sup>2</sup>

Biodiesel is another type of renewable energy resource gotten from animals and plants. It is biodegradable and nontoxic due to its zero greenhouse gas emissions. One major advantage of biodiesel is the ability to exhibit excellent cold flow properties similar to diesel from fossil fuels. Because the majority of biodiesel source emanates from edible sources, it has become a major concern as large scale production will result in competition with food supply. Therefore, a lot of research has been dedicated to the use of nonedible sources for biodiesel production.<sup>3</sup>

Biodiesel also known as Fatty Acid Methyl Esters (FAME) is obtained from reaction between Free Fatty Acids

(FFA) or tricylglycerols (TAGs) and a short chain alcohol either ethanol or methanol using catalyzed or non-catalyzed thermal reactions. In order to increase the efficiency of biodiesel production, a catalyst is used. Catalyzed reactions involve the use of homogeneous or heterogeneous substances. Heterogeneous catalysts are suitable for biodiesel fabrication as a result of non-corrosiveness and re-usability without the need for regeneration. However, the use of heterogeneous catalyst on large scale plants comes with some handling complexities. In most cases, biodiesel is used as blends with fossil fuel diesel so as to avoid engine modifications. Biodiesel improves the purity of diesel thereby making it cleaner and environmentally friendly. Nevertheless, they are used 100 % but only in rare cases.<sup>4</sup>

The cost of producing biodiesel is cheaper compared to conventional fossil fuel diesel. This is attributed to the cheap raw materials (used and waste oil, and fats from food industry, household and restaurant) that are used. Using nano-catalyst for biodiesel production is expected to further reduce the general cost of biodiesel production. Their very small particle size in the range of 1 to 100 nm increases their specific surface area thereby making them highly active and favorable in the heterogeneously-catalyzed biodiesel production.<sup>5</sup>

Over the last decade, scientists have employed carbon nanotubes, nanoclays and nanofibers to develop advanced and functional nanomaterials with geometrical sizes below 100 nm for different applications. Synthesis of nano particles, either through physical or chemical means, is energy dependent. The formation of nuclei following clustering and complexation gives rise to nanoparticles whose size and structure can be controlled using technology. It is evident from the environmental, technological and social point of view that nano particles are important due to their selectivity, durability and recoverability. The ability to control the size, shape, spatial distribution, electronic structure and surface composition makes nano-catalysts highly selective (100 %), active with long lifespan. Application of nanocatalysts in chemical industries has improved energy efficiency, optimized feedstock utilization and has reduced global warming. These favorable

characteristics have made nanocatalysts ideal for production of environmentally friendly fuels like biodiesel. However, nanomaterials are yet to be utilized on an industrial scale due some problems associated with their usage. These problems include difficulty in separation, high pressure drop, and formation of pulvurent materials.

After nanocatalysts are synthesized, it is important to investigate their chemical composition and crystal structure. The primary aim of characterizing nanocatalysts is to study their physical and chemical properties. Secondary objectives include degree of aggregation, size distribution, surface area and surface size. This is because the presence of organic ligands on surface catalyst or their sized distribution may influence their properties and possible applications. Credible characterization methods which allow compliance with regulations for large scale industrial application have been developed. Challenges associated with nanomaterial analytics is the lack of appropriate reference materials for tool calibration, complexities in sample preparation and data interpretation.<sup>6</sup> Difficulty in measurement of concentration especially in large scale production and waste/effluent monitoring are great barriers in the analysis of nanoparticles. Therefore, upscale production requires various methods of characterizations to be employed in other to obtain maximum information on the properties of the synthesized nanoparticles. In characterization process, the nanoparticles surface, that carries the ligands that influence the physical properties, are analyzed. Some of the characterization techniques that will be discussed in this review include Fourier Transform Infrared Spectroscopy (FTIR), Transmission Electron Microscopy (TEM), X-Ray Photoelectron Spectroscopy (XPS), Thermo Gravimetric Analysis (TGA), X-ray Diffraction spectroscopy (XRD), Scanning Electron Microscope (SEM), NMR, Carbon Hydrogen Nitrogen Sulfur test (CHNS), Energy Dispersive X-Ray Spectroscopy (EDX), Brunauer Emmett Teller (BET), Value Stream Mapping (VSM), N<sub>2</sub> adsorption-desorption (NAD) and UV-Vis diffuse reflectance (UDR).

## METHODOLOGY

For the purpose of this review, only research works published in reputable journals from 2017 to 2019 were used. This is to limit the scope of the study and to focus on more recent advancement on the topic. Google Scholar search engine was used to search for the journals. Open source journals that provided full article were utilized for the review. A comprehensive analysis dissecting key findings and subtopics was undertaken on each paper under review.

## LITERATURE REVIEW

In most cases, scientist prefer to systematicaly synthesize nanocatalyst in the laboratory using methodologies from existing literature. However shorter route have been utilized to save time by some researchers. For instance, Keihani et al. purchased calcium oxide nano-catalyst from a Malaysian vendor for the transesterification of chicken fat. The nanocatalyst was characterized to determine its physical properties. SEM showed 99 % purity and 50 nm particle size. 1 wt. % of the catalyst produced biodiesel of 94.4 % yield

with oil to methanol ratio of 9:1 used. The reaction reached completion in 5 hours at 65 °C. Keihani et al. used the synthesized biodiesel to make various biodiesel blends (B25, B50 and B75) with petroleum diesel in order to test improvement in fuel properties. They found B75 and B100 blends to be the best blend due to its favourable density and viscosity range when compared with international standards.<sup>7</sup>

### Thermal decomposition

When catalysts are subjected to pre-treatment under high temperature, the amount of active sites on the catalysts surface increase. This activity is referred to as thermal decomposition. Thermal decomposition increases the efficiency of the catalysts by eliminating substances that are absorbed on the surface of the catalyst when exposed to the atmosphere. For instance, CaO exposed to air absorbs water and carbon dioxide on the basic sites thus reducing the amount of basic sites on it. Thermal decomposition sometimes determines the shape and basicity of the obtained catalysts as increase in temperature desorbs molecule that obstruct the active sites.

Thermal decomposition technique was explored by Mazaheri et al. to produce heterogenous CaO nanocatalyst by calcinating, hydrating and dehydrating shells of *Chicoreus brunneus* (*Adusta murex*). Commercial CaO was also calcined at high temperature (900 °C) to eliminate contaminants. Both nanocatalysts were stored in a desiccator so as to prevent decrease in catalytic activity. The derived nanocatalysts were characterized using analytical techniques such as FTIR, XRD, TEM and BET. Mazaheri et al. developed two models of transesterification processes known as artificial neural networking and ant colony that predicted an optimal biodiesel yield of 93.5 % with minimal kinematic viscosity of 4.42 mm<sup>2</sup>s<sup>-1</sup> using CaO nanocatalyst in 35:1 methanol to RBO at reaction temperature and time of 1100 °C and 1 h 12 min, respectively. The biodiesel produced was in conformity with EN 14214 and ASTM D6751 standards.<sup>8</sup>

Using a conical reactor and thermal decomposition process, 10 g per batch of the nanoferrites catalysts were synthesized and then characterized using XRD. Dantas et al. investigated how Cu<sup>2+</sup> ions will affect the morphology, magnetism and structure of nanoferrites catalyst Ni<sub>0.5</sub>Zn<sub>0.5</sub>Fe<sub>2</sub>O<sub>4</sub> and its consequential influence the activity of the catalyst in the transesterification of soybean oil to FAME. The catalyst's texture was analyzed by N<sub>2</sub> absorption, heat content analyzed by temperature-programmed desorption and the magnetism measured. The biodiesel produced was also analyzed by gas chromatography. Dantas et al. noticed that whenever the doping of Cu<sup>2+</sup> ions increased from 0.0 to 0.4, the saturation magnetization value and the surface area of the catalyst reduced by 36.4 and 37 percent respectively. However the catalyst still retained its ferromagnetic properties as demonstrated by its attraction to magnets. Their findings points to an increase in biodiesel yield within 5.5-85 % range facilitated by the presence of Cu<sup>2+</sup> ions which signifies the potential application of these nanoferrite Cu<sup>2+</sup> doped Ni<sub>0.5</sub>Zn<sub>0.5</sub>Fe<sub>2</sub>O<sub>4</sub> catalyst in the biodiesel industry.<sup>9</sup>

In another study conducted by Raghavendra et al. ZnO nanoparticles were synthesized by thermally decomposing/treating zinc nitrate with *Garcinia gummi-gutta* seed extracts. Fixed amount of  $\text{Zn}(\text{NO}_3)_2 \cdot 6\text{H}_2\text{O}$  was used as a source of zinc and dissolved in 10 ml each of *G. gummi-gutta* seed extracts (0.2, 0.3, 0.4 and 0.5 g). Each of the mixtures was subjected to high temperatures to form ZnO nanoparticles by first dehydrating then decomposing. Effects of the various plant extracts were determined in the transesterification process to produce FAMES. Initial characterization of the nanocatalysts was performed by various techniques such as FTIR, UV-visible, SEM and XRD. Figure 1 shows the spectrum of UV-Vis analysis which reveal a sharp peak at 372 nm wavelength. They further evaluated the nanoparticles for antioxidant and photoluminescence properties. 1.5 wt.% of the derived ZnO nanoparticles were used for the transesterification of the *G. gummi-gutta* oil by adding it to methanol at 9:1 methanol to oil ratio. The reaction lasted for 2 h at 64 °C. Biodiesel yield of 80.1 % was obtained and the cold flow properties studied conformed with ASTM standard.<sup>10</sup>

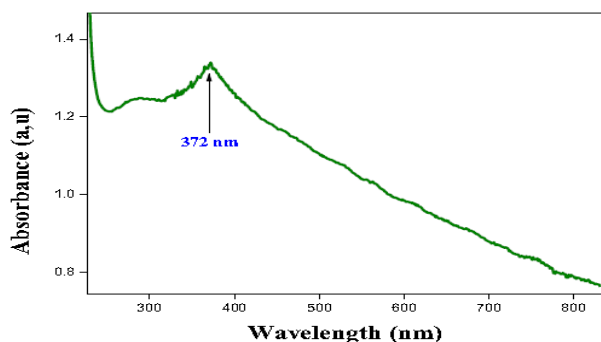


**Figure 1.** UV-Visible spectrum of ZnO nanoparticles.

Husin et al. used a slightly different approach by synthesizing solid nanocatalyst from fiber bunches of empty palm oil fruit for the transesterification of palm oil. Empty fruit bunch of palm oil was cleaned, dried and burnt to ashes. The  $\text{K}_2\text{O}$ -riched ash was further calcined at 600 °C temperature to produce nanoparticles with enhanced active sites. The nano particles were then characterized using XRD and SEM. XRD analysis showed that the catalyst had potassium oxide  $\text{K}_2\text{O}$  as the highest peak while the size of the particle fell in the 150-400 nm range as indicated by SEM analysis. 97 % of biodiesel yield was obtained when 1% of the catalyst at reaction time and temperature of 3 h and 600 °C, respectively. Their findings indicated that the nanocatalyst is cost effective and efficient.<sup>11</sup>

### Co-precipitation

Co-precipitation is used to produce highly acidic or basic catalysts by first preparing two component complex carrier. The carrier is then impregnated with a strong salt to get a mesoporous basic nanocatalyst or an organic ester to synthesize basic nanocatalyst. Nanocatalysts prepared using this process tend to easily separate from the final product.

Co-precipitation method was employed by Gardy et al. to synthesize a recyclable mesoporous and efficient solid acid nano-catalyst  $\text{TiO}_2/\text{PrSO}_3\text{H}$ . Initial pretreatment of titanium nanoparticles  $\text{TiO}_2$  NPs was conducted using ammonium hydroxide to produce a carrier with active receptive sites.

The carrier was then added to 1,3-propane sulfone in appropriate proportion to get the co-precipitate catalyst at 80 °C denoted as  $\text{TiO}_2/\text{PrSO}_3\text{H}$ . Gardy et al. went further to produce biodiesel from used cooking oil using the synthesized nanocatalyst. Various analytical methods including FTIR, XRD, TEM, XPS and TGA were used to characterize the synthetic nano-catalyst. Reaction for 9 h at 60 °C yielded 98 % of FAME when 4.5 wt.% loaded catalyst was used together with methanol at 1:15 oil to methanol molar ratio. The acid nanocatalyst was recycled five times without losing its efficiency. The biodiesel produced satisfied European Standard EN and American society testing and materials standards, ASTM.<sup>12</sup>

In another similar study, Vijayakumar et al. successfully prepared  $\text{KF-Al}_2\text{O}_3$  nanocatalyst by co-precipitation method for the transesterification of beef processing industrial sludge to biodiesel. The transesterification reaction was supported by ultrasonic irradiation. Characterization of the nanocatalyst was accomplished using XRD, SEM and FTIR. Yield of biodiesel was 97 % when 6 wt.% loaded catalyst was used in 1:15 oil to methanol molar ratio for a reaction time of 3 h. The nanocatalyst recycled seven times without diminishing in efficiency. The high efficiency was attributed to enhanced surface area of the nanocatalyst and the ultrasonic wave effect as well. Results from the quality test performed on the biodiesel showed that the biodiesel was within ASTM D6751 standards.<sup>5</sup>

Bayat et al. also used the co-precipitation method to prepare an efficient nanocatalyst  $\text{Fe}_3\text{O}_4@\text{Al}_2\text{O}_3$  which they used for the transesterification of waste cooking oil to FAME. The process involved the initial formation of magnetic suspension containing  $\text{Fe}_3\text{O}_4$  nanoparticles which is added to aluminium isopropoxide and sonicated for 2 h. The obtained nanoparticles were washed, dried and characterized using analytical methods. XRD analysis showed the standard cubic crystal pattern of  $\text{Fe}_3\text{O}_4$  nanocatalyst, while DLS characterization showed mean particle size of 193 nm. The VSM analysis confirmed high saturation magnetization of the catalyst. Analysis of variance ANOVA showed the temperature and time effect on the reaction exceeded that of methanol to oil ratio. In fact, temperature/time significance exceeded any other interaction. Results also showed that the rate constant was within 0.001 to 0.157  $\text{min}^{-1}$  and activation energy was 55.48  $\text{kJ mol}^{-1}$  for the transesterification reaction. The reaction was endergonic  $\Delta H = 54.08 \text{ kJ mol}^{-1}$  and nonspontaneous  $\Delta G = 93.80 \text{ kJ mol}^{-1}$ . They recovered the catalyst was heated at 400 °C and the catalyst was recycled four times without diminishing efficiency.<sup>1</sup>

For the purpose of biodiesel production, from waste cooking oil, Ashok et al. synthesized nanostructured magnesium oxide ( $\text{MgO}$ ) catalysts using the co-precipitation technique. A precipitate was formed by adding dropwise required amount of aqueous sodium hydroxide to an aqueous mixture containing equal amounts of magnesium nitrate hexahydrate and 0.1 M of sodium dodecyl sulphate. The formed precipitate was dried and heated at 100, 200, 300, 400 and 500 °C. Ashok et al. characterized the nanocatalysts using XRD, FTIR, UDR and EDX analysis. Reaction at 65 °C for 1 h with 2 wt. % amount of  $\text{MgO}$  nanocatalyst with oil to methanol molar ratio of 1:24, yielded 93.3 % of biodiesel. They further determined the fatty acid methyl ester content using GC-MS.<sup>13</sup>

A solid nanocatalyst CuO-Mg was prepared by Varghese et al. by co-precipitation of copper acetate (5 M) with aqueous NaOH doped with MgCl<sub>2</sub>. Furthermore, a novel transesterification model based on the assistance of ultrasonication was used to synthesize FAME using the CuO-Mg nanocatalyst. Transesterification at 60 °C for 30 min with 6:1 oil to methanol ratio yielded 71.78 % biodiesel although total FAME conversion could reach up to 82.83 %. Visual analysis of the synthesized biodiesel using gas GC-MS was also performed. Figure 2 shows the GC chromatogram of FAME and SFO biodiesel produced.<sup>14</sup>

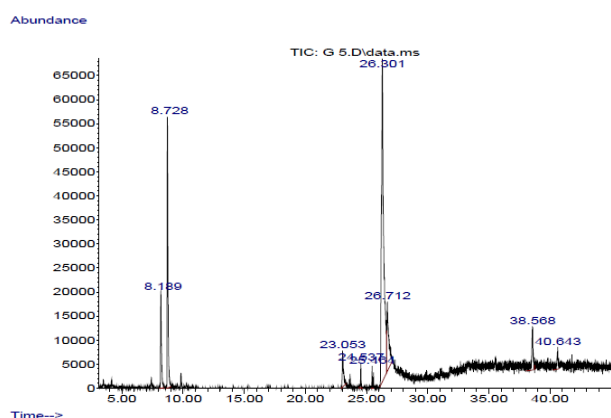


Figure 2. GC Chromatogram of FAMES of SFO biodiesel.

### Impregnation

Impregnation is used when preparing doped catalyst by amalgamating alkali metals with the parent catalyst under high temperature. For instance, the catalytic strength of CaO catalyst is enhanced by impregnating alkali metals ions onto nano CaO catalyst. The CaO solid carrier is first suspended in water before the precursor (aqueous) is added. Finally, the combined catalyst is subjected to high temperatures in order to transform the precursor to its active state. However, care must be taken not to overheat during calcination as doing so will result to surface sintering even though high temperatures favors the formation of crystals (combination of carrier and active component). The type of alkali ion used in impregnation determines activity of the doped catalyst. In most cases, the precursors used are ions of K<sup>+</sup>, Li<sup>+</sup> and Na<sup>+</sup>.

Using the impregnation method, Liu et al. prepared a solid base nano-magnetic catalyst, K/ZrO<sub>2</sub>/γ-Fe<sub>2</sub>O<sub>3</sub>, to synthesize biodiesel. ZrOCl<sub>2</sub>·8H<sub>2</sub>O was added to a mixture containing FeCl<sub>2</sub>·4H<sub>2</sub>O and FeCl<sub>3</sub>·6H<sub>2</sub>O (in 1:2 mole ratio) and subsequently, ammonia 25 wt.% was added to produce a gel-sol (Zr(OH)<sub>4</sub>-Fe(OH)<sub>3</sub>). The gel-sol was then impregnated with aqueous solution of KOH to obtain KOH/(Zr(OH)<sub>4</sub>-Fe(OH)<sub>3</sub>). Further calcination of the precursor was performed to produce K/ZrO<sub>2</sub>/γ-Fe<sub>2</sub>O<sub>3</sub> nanocatalyst viewed as nano-magnetic catalyst. Figure 3 shows the diagrammatic illustration of the nano-magnetic catalyst. XRD, BET, VSM, TEM, SEM and EDX analysis was used to characterize the catalyst. XRD revealed particle size within 15-25 nm range. Reaction conditions of 10:1 methanol molar ratio, 5 % catalyst and 65 °C for 3 h resulted in optimum biodiesel yield above 93.6 wt%. The catalyst was recycled six times without depreciating in strength.

The difficulty experienced in core shell production demonstrates great potential for use in green biodiesel production.<sup>15</sup>

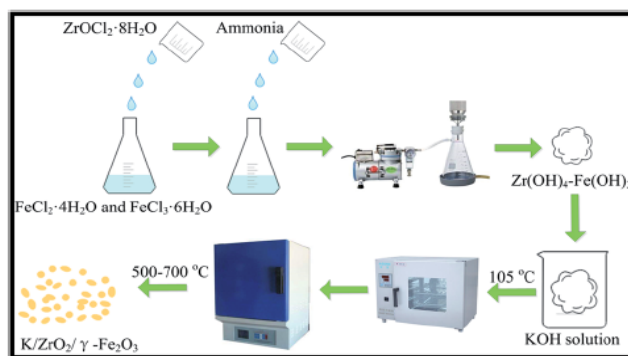


Figure 3. Synthesis of nano-magnetic catalyst K/ZrO<sub>2</sub>/γ-Fe<sub>2</sub>O<sub>3</sub>.

In another research conducted by Mostafa et al. , the wet impregnation method was used to prepare different K-La nanocatalysts supported on zeolite ZSM-5 and tested each to produce biodiesel from soybean oil. The optimal catalyst was found to be the one containing 7 wt.% of La loaded with 1 wt.% of K. when they used the catalyst with methanol to oil molar ratio of 12:1 at 60 °C, yield of FAME reached 90 % in 3h of reaction time. High catalytic activity of K-La/ZSM nanocatalyst was attributed to high number of basic sites. The nanocatalyst was characterized using various analytical methods which include SEM, XRD, TEM, FTIR and N<sub>2</sub> adsorption in order to determine its physical and chemical properties.<sup>3</sup>

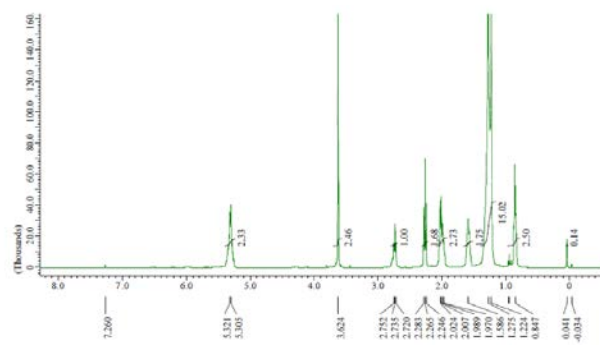


Figure 4. <sup>1</sup>H-NMR spectra of transesterified soybean oil.

Rafati et al. prepared several type of nanocatalysts (MgO-NaOH, CaO-NaOH, CaO-KOH, MgO-KOH) by impregnating or loading different strong bases on Ca(NO<sub>3</sub>)<sub>2</sub>·4H<sub>2</sub>O. It involved the addition of a strong base to Ca(NO<sub>3</sub>)<sub>2</sub>·4H<sub>2</sub>O dissolved in ammonia solution to form precipitates that are further dried at 120 °C and calcined at 400 °C. Rafati et al. tested each nanocatalyst to determine their level of effectiveness in biodiesel production. Electrolysis based transesterification was used to produce biodiesel using waste cooking oil. Their findings suggests high performance of MgO-NaOH nanocatalyst as demonstrated by biodiesel yield of 94-98 % when oil to methal ratio of 3:5 was used. The quality of the biodiesel was within ASTM and EN standard. The nanocatalysts were characterized and the XRD, results revealed average mean crystal size of 66.77 nm.<sup>4</sup>

## Mixing

Mixing is the method used to produce catalysts of metal oxide mixtures. Significant amount of the active component (metals) are mixed with oxides. This produces a favorable catalyst with smaller area and concentration of basic active sites. Often times, impregnation method is ensured to form higher active catalysts. For instance, CaO/NiO mixed oxide was first prepared as a carrier before impregnating it with KF to form an enhanced CaO-KF/NiO-KF nanocatalyst.

The mixing method was employed by Hassan et al. . Sol-gel samples of CaO-X nanocatalysts were prepared and used for the transesterification of palm oil. The Pechini procedure, whereby dissolved  $\text{Ca}(\text{NO}_3)_2 \cdot 4\text{H}_2\text{O}$  (1.0, 1.5, 2.0 mol) was slowly added to citric acid/deionized water to form a visous gel, was employed. The gel was further dried and calcined at 850 °C to produce CaO-X nanocatalyst. The prepared nanocatalysts were characterized for crystallinity and morphology using NAD analysis and XRD. Using all the catalysts for the the transesterification process, they synthesized biodiesel. According to their results, the incomplete reaction during synthesis of CaO-1.0 formed water on the catalyst surface which lowered its basic strenght thereby lowering the catalytic activity of the catalyst. CaO-2.0 was found to be mesoporous with high catalytic activity. This was demonstrated by formation 81 % FAME within 3 h reaction time.<sup>16</sup>

Bharti et al. used sol-gel mixing method to prepare calcium oxide nano catalysts. They used H-NMR, SEM, TEM, XRD, FTIR and BET to characterize the nanocatalyst. Figure 4 shows H-NMR transesterified soybean oil. XRD results showed the particulate size of the catalyst with range upto 8 nm, surface area about 67.781 m<sup>2</sup> g<sup>-1</sup> and pore diameter was 3.302 nm. They used 3.675 wt.% of the nanocatalyst in methanol to oil ratio of 11:1 to synthesize FAME in 97.61% yield from soybean oil at 60 °C for 2 h reaction time.<sup>17</sup>

The sol-gel mixing and impregnation methods were used separately to prepare KF/ $\gamma$ -Al<sub>2</sub>O<sub>3</sub> nanaocatalysts by two procedures. First, by adding a certain amount of KF-2H<sub>2</sub>O and  $\gamma$ -Al<sub>2</sub>O<sub>3</sub> in ethanol to form a clear white gel which was vaporized, dried, milled and calcined at high temperature to form KF/ $\gamma$ -Al<sub>2</sub>O<sub>3</sub>-OP nanocatalyst and secondly by directly impregnating KF over commercial  $\gamma$ -Al<sub>2</sub>O<sub>3</sub> under equivalent conditions devoid of ethanol. The synthesized nanocatalyst was used for the tri-component coupling transesterification of dimethyl carbonate, canola oil and methol. 10.0 wt.% KF was loaded and calcinated at 400 °C for the formation of nano catalyst. They applied 5.0 wt.% of the catalyst to methanol which was further added to the oil at molar ratio of dimethyl carbonate (DMC)/oil/methanol of 1:1:8. A reaction time of 2 h at 65 °C yielded 98.8 % biodiesel. High conversion rate of biodiesel has been attributed to the surface to volume ratio and high basicity of the catalyst.<sup>18</sup>

Aradhya and Math synthesized strontium oxide (SRO) nanocatalyst by mixing urea and strontium oxide to form an initial homogeneous solution which is further heated up to 900 °C. A solid nanocatalyst was formed and used used to produce biodiesel from boiled vegetable oil. They further undertook an investigative study on The performance characteristics of biodiesel blends formed by mixing with

diesel was compared with conventional diesel oil when fueled in compression ignition (CI) diesel. Their results showed close similarity between properties of conventional diesel and that of B20 biodiesel.<sup>19</sup>

Ali et al. <sup>20</sup> prepared a nano magnetic CaO/Fe<sub>3</sub>O<sub>4</sub> catalyst by chemically mixing 0.003M of calcium nitrate solution with 3.5g of Fe<sub>3</sub>O<sub>4</sub>. A precipitate was formed by adding 2 M of sodium hydroxide to the mixture and dried at 80 °C. Finally CaO/Fe<sub>3</sub>O<sub>4</sub> loaded nanocatalyst was formed by calcination of the dried precipitate at 550 °C for 1 h. The nanocatalyst was further characterized using FTIR, SEM, XRD and EDX analytical methods. The synthesized catalyst which was complemented by CaFe<sub>2</sub>O<sub>4</sub> was used in the producing biodiesel. Biodiesel with 69.7% yield was synthesized after 300 min of transesterification reaction at 65 °C using 10 wt.% of CaO/Fe<sub>3</sub>O<sub>4</sub> nanocatalyst loaded on methanol in 20:1 methanol/oil molar ratio. The quality of biodiesel produced was within EN and ASTM standard.<sup>20</sup>

## CONCLUSION AND RECOMMENDATION

Protecting our ecosystem from harmful greenhouse gases is essential hence there is a need to explore advanced methods for producing renewable alternatives. A lot of progress has been achieved over the years in the use of nanocatalyst for biodiesel synthesis. This review has covered methodologies used with the goal of improving the efficiency of transesterification reactions.

Characteristics such as high basicity, regeneration and reusability in addition to proper preparation and environmental safety make nanocatalysts suitable for biodiesel production. Various investigations covered in this review lead to the conclusion that nanocatalyst for biofuel production can enhance biodiesel production by far greater percentage compared to homogeneous catalyst. The various types of nanocatalysts used in recent times are metal oxides (CuO), metal oxide supported by metal oxide (KF-ZnO-Fe<sub>3</sub>O<sub>4</sub>) and metal supported on metal oxides (Au-ZnO).

It is recommended for future researchers to put greater emphasis on testing possibility and efficiency of nanocatalyst from biomass source. Experiments using inorganic (metal oxides) and organic (biomass) nanocatalysts can be undertaken concurrently to examine differences or changes in reaction conditions and biodiesel yield. We hope that this review will guide future researchers interested in nanocatalyst for biodiesel synthesis.

## REFERENCES

- Bayat, A., Baghdadi, M., Bidhendi, G. N., Tailored magnetic nano-alumina as an efficient catalyst for transesterification of wastecooking oil: Optimization of biodiesel production using response surface methodology, *Energ. Convers. Manag.*, **2018**, 157, 395-405.  
<https://doi.org/10.1016/j.enconman.2018.09.086>
- Hu, S., Guan, Y., Wang, Y., Han, H., Nano-magnetic catalyst KF/CaO-Fe<sub>3</sub>O<sub>4</sub> for biodiesel production, *Appl. Energ.*, **2011**, 88, 2685-2690.  
<https://doi.org/10.1016/j.apenergy.2011.02.012>

- <sup>3</sup>Mostafa, F., Zinatizadeh, L., Akbar, A., Parasto, N., Fataneh, J., Catalytic Performance and Characterization of Promoted K-La/ZSM-5 Nanocatalyst for Biodiesel Production, *Iran J. Chem. Eng.*, **2018**, 37(2), 33-44.
- <sup>4</sup>Rafati, A., Kambiz, T., Maryam, N., Production of Biodiesel by Electrolysis Method from Waste Cooking Oil Using Heterogeneous MgO-NaOH Nano Catalyst, *Energ. Sources, Part A*, **2018**, 41(9), 1062-1074. <https://doi.org/10.1080/15567036.2018.1539139>
- <sup>5</sup>Vijayakumar, B., Sivakumar, P., Ramesh, K., Choksi, H., Sircar, A., Sono-Chemical Biodiesel Production from Beef Processing Industrial Sludge in the Presence of nano-KF-Al<sub>2</sub>O<sub>3</sub>, *Int. Conf. Thermal. Eng., Gandhinagar*, 2019. <https://journals.library.ryerson.ca/index.php/ictca/article/view/1150>
- <sup>6</sup>Mourdikoudis, S., Pallares, R. M., Thanh, N. T., Characterization Techniques for Nanoparticles: Comparison and Complementarity Upon Studying Nanoparticles Properties, *Nanoscale*, **2018**, 10, 12871-12934. <https://doi.org/10.1039/C8NR02278J>
- <sup>7</sup>Keihani, M., Esmaeili, H., Rouhi, P., Biodiesel Production from Chicken Fat Using Nano-calcium Oxide Catalyst and Improving the Fuel Properties via Blending with Diesel, *Phys. Chem. Res.*, **2018**, 6(3), 521-529.
- <sup>8</sup>Mazaheri, H., Ong, H. C., Masjuki, H. H., Amini, Z., Harrison, M. D., Wang, C.-T., Kusumo, F., Alwi, A., Rice bran oil based biodiesel production using calcium oxide catalyst derived from *Chicoreus brunneus* shell, *Energy*, **2017**, 144, 10-19. <https://doi.org/10.1016/j.energy.2017.11.073>
- <sup>9</sup>Dantas, J., Leal, E., Mapossa, A. B., Cornejo, D. R., Costa, A. F., Magnetic nanocatalysts of Ni<sub>0.5</sub>Zn<sub>0.5</sub>Fe<sub>2</sub>O<sub>4</sub> doped with Cu and performance evaluation in transesterification reaction for biodiesel, *Fuel*, **2017**, 191, 463-471. <https://doi.org/10.1016/j.fuel.2016.11.107>
- <sup>10</sup>Raghavendra, M., Yatish, K. V., Lalithamba, H. S., Plant-mediated green synthesis of ZnO nanoparticles using *Garcinia gummi-gutta* seed extract: Photoluminescence, screening of their catalytic activity in antioxidant, formylation and biodiesel production, *Eur. Phys. J.*, **2017**, 132(358), 358, 1-11. <https://doi.org/10.1140/epjp/i2017-11627-1>
- <sup>11</sup>Husin, H., Asnawi, T. M., Firdausi, A., Husaini, H., Ibrahim, I., Hasfita, F., Solid Catalyst Nanoparticles derived from Oil-Palm Empty Fruit Bunches (OP-EFB) as a Renewable Catalyst for Biodiesel Production, *IOP Conf. Ser: Mater. Sci. Eng.*, **2018**, 358(3<sup>rd</sup>), Int. Conf. Global Sustain. Chem: Eng. (ICGSCE-2017, 15-16 February, Purajaya, Malaysia) <https://doi.org/10.1088/1757-899X/358/1/012008>
- <sup>12</sup>Gardy, J., Hassanpour, A., Lai, X., Ahmed, M. H., Rehan, M., Biodiesel Production from Used Cooking Oil Using a Novel Surface Functionalised TiO<sub>2</sub> Nano-catalyst, *Appl. Catal. B*, **2017**, 207, 297-310. <https://doi.org/10.1016/j.apcatb.2017.01.080>
- <sup>13</sup>Ashok, A., Kennedy, L. J., Vijaya, J. J., Aruldoss, U., Optimization of biodiesel production from waste cooking oil by magnesium oxide nanocatalyst synthesized using coprecipitation method, *Clean Technol. Environ. Policy*, **2018**, 20(6), 1219-1231, DOI: [10.1007/s10098-018-1547-x](https://doi.org/10.1007/s10098-018-1547-x)
- <sup>14</sup>Varghese, R., Jose, S., Joyprabu, H. and Johnson, I., "Ultrasonication Assisted Production of Biodiesel from Sunflower Oil by Using CuO: Mg Heterogeneous Nanocatalyst," *IOP Conf. Ser.: Mater. Sci. Eng.*, **2017**, 225(Int. Conf. Mater. Alloys, Exp. Mech. (ICMAEM, 3-4 July 2017, Narsimhy Reddy Eng. College, Tamilnadu, India, 2017. <https://doi.org/10.1088/1757-899X/225/1/012213>
- <sup>15</sup>Liu, K., Wang, R., Yu, M., Biodiesel production from soybean oils by a novel nano-magnetic solid base catalyst (K/ZrO<sub>2</sub>/γ-Fe<sub>2</sub>O<sub>3</sub>), *RSC Adv.*, **2017**, 7, 51814-51821. <https://doi.org/10.1039/C7RA10067A>
- <sup>16</sup>Hassan, N., Ismail, K. N., Hamid K. H. K., Hadi, A., CaO Nanocatalyst for Transesterification Reaction of Palm Oil to Biodiesel: Effect of Precursor's Concentration on the Catalyst Behavior," *IOP Conf. Ser: Mater. Sci. Eng.*, **2018**, 358(3<sup>rd</sup>), Int. Conf. Global Sustain. Chem: Eng. (ICGSCE-2017, 15-16 February, Purajaya, Malaysia), <https://doi.org/10.1088/1757-899X/358/1/012059>
- <sup>17</sup>Bharti, P., Singh, B., Dey, R. K., Process Optimization of Biodiesel Production catalyzed by CaO nanocatalyst Using Response Surface Methodology, *J. Nanostructure Chem.*, **2019**, 9, 269-280. <https://doi.org/10.1007/s40097-019-00317-w>
- <sup>18</sup>Tang, Y., Ren, H., Feiqin, C., Xuefan, G., Zhang, J., Nano KF/Al<sub>2</sub>O<sub>3</sub> particles as an efficient catalyst for no-glycerol biodiesel production by coupling transesterification, *RSC Adv.*, **2017**, 7, 5694-5700. <https://doi.org/10.1039/C6RA25782H>
- <sup>19</sup>Aradhya, P. J., Math, M. C., Biodiesel Production From Boiled vegetable oil Using Self Synthesized Strontium Oxide Nano Catalysts, *Int. J. Innov. Res. Adv. Eng.*, **2019**, 6(6), 36-42.
- <sup>20</sup>Ali, M. A., Al-Hydary, A. I., Al-Hattab, A. T., Nano-Magnetic Catalyst CaO-Fe<sub>3</sub>O<sub>4</sub> for Biodiesel Production from Date Palm Seed Oil," *Chem. React. Eng. Catal.*, **2017**, 12(3), 460-468. <https://doi.org/10.9767/bcrec.12.3.923.460-468>
- <sup>21</sup>Bankovic-Ilic, I. B., Miladinovic, R. M., Stamenkovic, O. S., Veljkovic, V. B., Application of Nano CaO-based catalysts in Biodiesel Synthesis, *Renew. Sust. Energ. Rev.*, **2017**, 72, 746-760. <https://doi.org/10.1016/j.rser.2017.01.076>
- <sup>22</sup>Kumar, D., Ali, A., Nanocrystalline Lithium Ion Impregnated Calcium Oxide As Heterogeneous Catalyst, *Energ. Fuels*, **2010**, 24, 2091-2097. <https://doi.org/10.1021/ef901318s>
- <sup>23</sup>Jadhav, S. D., Tandale, M. S., Optimization of transesterification process using homogeneous and nano-heterogeneous catalysts for biodiesel production from *Mangifera indica* oil, *Sust. Energ.*, **2017**, 37(1), 533-545. <https://doi.org/10.1002/ep.12690>

Received: 28.02.2020.

Accepted: 26.04.2020.